Aerosol remote sensing from ground–based polarized sky–radiance under cloudy conditions

Hans Christian Grob

München 2019

Aerosol remote sensing from ground–based polarized sky–radiance under cloudy conditions

Hans Christian Grob

Dissertation
an der Fakultät der Physik
der Ludwig–Maximilians–Universität
München

vorgelegt von
Hans Christian Grob
geboren in Ebersberg/Obb.

München, den 4.7.2019

Contents

Zusammenfassung

Für ein besseres Verständnis der Wechselwirkungsprozesse zwischen Aerosolen und Wolken ist es nötig diese in der Umgebung von Wolken zu untersuchen. Polarisationsaufgelöste Messungen haben sich als adäquate Erweiterung klassischer, multispektraler Photometrie bewährt, da sie zusätzliche Information über die Teilen enthalten. In dieser Arbeit wurde ein neuer Algorithmus entwickelt, um mikrophysikalische und optische Aerosoleigenschaften aus bodengebundenen, polarisations- und wellenlängenaufgelösten Messungen der Himmelshelligkeit abzuleiten. Dieser beinhaltet eine Technik zum detektieren und entfernen bewölkter Messpunkte, wodurch die Methode bei teilweiser Bewölkung anwendbar ist.

Es wurden numerische Studien mit synthetischen Beobachtungen durchgeführt, die mit 3D Monte–Carlo Strahlungstransportrechnungen erzeugt wurden und unterschiedliche Wolkensituation enthalten, wie Straßen aus Quaderwolken oder realistischere Wolkenfelder aus Large–Eddy–Simulationen (LES). Diese werden zunächst verwendet, um Veränderungen der gemessenen polarisationsaufgelösten Strahldichte zu bestimmen, die durch von Wolken induzierte 3D–Stahlungseffekte entstehen. Die unpolarisierte Strahldichte wird in unmittelbarer Nähe zu Wolken bei $550\,$nm um bis zu $55\,\%$ erhöht. In der selben Situation wird die polarisierte Strahldichte verringert, jedoch nur um ungefähr $25\,\%$. Als nächstes wurde der Einfluss dieser veränderten Messungen auf die aus ihnen abgeleiteten Aerosoleigenschaften untersucht. In den meisten Fällen konnten Effektivradius und optische Dicke zuverlässig bestimmt werden, sogar wenn ein großer Teil (bis zu $70\,\%$) des Himmels mit Wolken bedeckt war. Die optische Dicke des Aerosol wird in der Regel leicht überschätzt, jedoch um nicht mehr als 0.03 oder $10\,\%$. Der abgeleitete Effektivradius der Feinpartikel stimmt auf $0.04\,\mu$m genau, unabhängig vom Grad der Bewölkung. Für den Effektivradius der Grobpartikel wird der Fehler hin zu größeren Teilchen höher. Der Realteil des Brechungsindex wird in den meisten Fällen überschätzt.

Im zweiten Teil wurde der Algorithmus auf Messungen des multispektralen Sonnenphotometers SSARA angewendet. Dieses wurde bereits mit Polarisationsfiltern ausgestattet, um bei $501.5\,$nm die polarisierte Strahldichte messen zu können. Während der A-LIFE Messkampagne, die im April 2017 in Zypern stattfand, sammelte SSARA an 22 Tagen Messdaten. Hier werden drei Fallstudien gezeigt: Die erste veranschaulicht das Verhalten des Algorithmus bei teilweiser Bewölkung. Im zweiten Fall herrschte aufgrund einer Saharastaubschicht eine hohe Aerosolbelas-

tung bei ansonsten klarem Himmel. Der dritte Fall beschreibt das Aufziehen von Feinpartikel–Aerosolen aus Waldbrandgebieten.

Während der Vorbereitung des Instruments wurde zudem eine neuartige radiometrische und polarimetrische Kalibriermethode entwickelt, die es erlaubt gleichzeitig die Güte und die Winkel der Polarisationsfilter mit hoher Genauigkeit zu bestimmen (entsprechend auf 0.002 und unter 0.1°). Des weiteren wurde eine neue Methode für die Kalibrierung unserer altazimuthalen Montierung verwendet, die eine Korrektur der Positionierung des Messkopfs auf unter 32 arcmin ermöglicht. Dies ist momentan durch die Genauigkeit des verwendeten Sonnensuchers beschränkt. Diese beiden Kalibriermethoden sind auch auf andere Sonnenphotometer anwendbar, wie zum Beispiel die Cimel CE318-DP Instrumente, die in AERONET verwendet werden.

Abstract

To study aerosol–cloud interactions, observations in the vicinity of clouds are necessary. Polarimetry has proven to be a useful enhancement to classical multispectral photometry to infer aerosol optical properties, as polarized radiation contains additional information about the particles. In this thesis, a new retrieval algorithm for the retrieval of microphysical and optical aerosol properties from ground–based polarized and multispectral sky radiance measurements was developed. It includes a cloud screening mechanism that makes the method applicable to partly cloudy situations.

Numerical studies have been conduced with synthetic observations generated using 3D Monte–Carlo radiative transfer simulations of different cloud situations, including cuboid cloud streets and more realistic Large–Eddy simulation (LES) generated cloud fields. These are used to first determine the 3D radiative cloud effects observable in the measured polarized radiances as a function of cloud distance. Total radiance is increased by up to $55\,\%$ on average close to clouds at $550\,\mathrm{nm}$, while linear polarized radiance is reduced, but only by about $25\,\%$ in the same case. The influence of these altered measurements on the aerosol properties retrieved from them was investigated next. For most cases, effective radius and optical depth of the aerosol can be retrieved well, even if a significant portion (up to $70\,\%$) of the sky is covered by clouds. The aerosol optical depth is typically slightly overestimated (not more than 0.03 or $10\,\%$). The retrieval of fine mode particle effective radius is accurate to within $0.04\,\mu\mathrm{m}$ regardless of the cloud contamination. For the retrieved coarse mode effective radius the error becomes larger towards bigger particles. A positive bias in the retrieved index of refraction has been observed in most cases.

In a second step, the retrieval was applied to measurements made with the SSARA multispectral sun and sky photometer, which has previously been equipped with polarizer filters to measure polarized radiance at $501.5\,\mathrm{nm}$. During the A-LIFE field campaign in Cyprus in April 2017, SSARA collected 22 days of data. Here, three case studies are presented: The first demonstrates the performance of the retrieval under partially cloudy conditions. In the second case, a high aerosol load due to a Saharan dust layer was present during otherwise perfect clear sky conditions. Fine mode dominated Biomass burning aerosol was observed in the third case.

During the preparation of the instrument, a novel radiometric and polarimetric calibration method has been developed, which simultaneously determines the

linear polarizers' diattenuation and relative orientation with high accuracy (0.002 and below 0.1°, respectively). Furthermore, a new calibration method for the alt–azimuthal mount capable of correcting the instrument's pointing to within 32 arcmin was implemented. So far, this is limited by the accuracy of the sun-tracker. Both these methods are applicable to other sun and sky radiometers, such as Cimel CE318-DP instruments used in AERONET.

1. Introduction

The influence of aerosols on the earth's radiation budget is still not understood
well enough and introduces high uncertainties in the prediction of the climate
(IPCC, 2013). Several interaction processes are differentiated. First, the *direct
aerosol effect* describes the change of reflected solar radiation by the atmosphere
due to absorption and scattering by aerosols. On the other hand, aerosols can
act as cloud condensation nuclei (CCN) and therefore influence the formation
of clouds. Distributing the available moisture over more particles reduces their
size and therefore increases the cloud albedo (Twomey, 1977). Also, it has been
argued that the cloud droplet growth cycle is offset and hence the lifetime of the
cloud prolonged (Albrecht, 1989). These are known as *indirect aerosol effects.*
Additionally, effects precipitation are of course not only of interest on a climate,
but also on shorter time scales.

To advance our understanding of these aerosol–cloud interactions, the so-called
"twilight" or cloud transition zone surrounding clouds has to be studied. Koren
et al. (2007) suggests this region reaches several ("tens of") kilometers from the
cloud and is characterized by a higher humidity, hydrated aerosols and sub-visible
clouds. Calbó et al. (2017) makes the case that aerosols and clouds are both just
a suspension of particles and the distinction is difficult and rather arbitrary. To
gain insight into microphysical processes in the twilight zone not only the total
aerosol load (measured as aerosol optical depth, AOD) is of interest. Also, the
aerosol size distribution and its optical properties, such as the refractive index are
important. They can be used to discriminate between different types of aerosol,
by source region or chemical composition. These, in turn are indications for the
particles hygroscopicity, and therefore its influence on the cloud development.

There are several studies that investigate aerosol–cloud interactions from satellite
and ground–based measurements. While the former has the advantage of global
coverage, its spatial resolution is still not good enough to properly resolve smaller
clouds and the aerosol in between them. Várnai and Marshak (2012) describes
problems of near–cloud aerosol observations and how complementing measurements
from the CALIOP lidar and multispectral observations from the MODIS imager
can be used to study the twilight zone. Marshak et al. (2008) describes the 3D
radiative effects of clouds from MODIS observations. They find a stronger increase
of total radiance in shorter wavelengths due to the presence of nearby clouds.

With the AErosol RObotic NETwork (AERONET), a global network of sunpho-

tometers for sun and sky radiance measurements was established to provide aerosol measurements that may be used for validating satellite observations (Giles et al., 2019; Holben et al., 1998). The direct sun irradiance measurements can be directly used to derive the total and – in cloud-free situations – aerosol optical depth. While giving accurate information about the optical depth, these measurements contain no information about the scattering phase function, thus limiting the possibility to derive further information about the aerosol microphysics and optical properties. The Ångström exponent and its spectral curvature can be used to gain information about the aerosol size distribution and origin (Eck et al., 1999; Gobbi et al., 2007). The Spectral Deconvolution Algorithm (SDA) described in O'Neill et al. (2003) uses multispectral optical depth measurements for discriminating a fine and a coarse aerosol mode based on their size. AERONET measurements are routinely used as input for this method. Gasteiger et al. (2011) employ a combination of AERONET and ground–based lidar measurements to retrieve microphysical and optical properties of volcanic ash aerosols. They find that sun photometer measurements of the solar aureole provide additional information on the size of large particles that the lidar is insensitive to. Arola et al. (2017) have shown that the strictness of cloud screening methods applied to different levels of AERONET data has an influence on the retrieved fine-mode aerosol optical depth from the SDA. The effect of stratiform cirrus clouds on the retrieval of the same parameter was investigated in Smirnov et al. (2018).

In addition to direct sun observations, the sky radiance is measured in different scans. The multi–spectral radiance observed in these more complex geometries can be used to gain further insight into the scattering behaviour of the aerosol. Dubovik and King (2000) describe a retrieval using AERONET sun and sky radiance observations to derive aerosol optical properties. These are cloud-screened by imposing an upper limit on the variance of the measurements left and right of the sun (Holben et al., 2006). This limits the aerosol information in the vicinity of clouds.

Classically, this information is retrieved from multispectral measurements. Recently, polarimetric measurements started to be included as well. For satellites, this was done with the series of POLDER instruments (Deschamps et al., 1994). Several approaches for retrieving aerosol properties from its measurements have been developed (Dubovik et al., 2011; Hasekamp and Landgraf, 2007; Hasekamp et al., 2011). In POLDER measurements, the polarized scattering phase function of water produces distinct features in the polarized radiance allowing for cloud detection (Stap et al., 2015). The SPEX instrument proposed by van Harten et al. (2011) is a pointing multi–angle polarized hyperspectral radiometer. Originally designed as a satellite instrument (van Amerongen et al., 2017), a ground based version has been built (van Harten et al., 2014). Di Noia et al. (2015) demonstrates the use of

its data for retrieving aerosol properties. Similar use cases have been demonstrated for the Research Scanning Polarimeter (RSP, Chowdhary et al. (2001)), and the Airborne Multiangle Spectro-Polarimetric Imager (AirMSPI, Diner et al. (2013)).

Newer models of the sun and sky photometers used for AERONET are capable of polarized measurements that can be used to reduce the error in retrieved aerosol properties (Li et al., 2009). Dubovik et al. (2006) suggest that polarimetric measurements can be used to gain more insight into the aerosol particle shape. This was further examined by Fedarenka et al. (2016) using an updated AERONET inversion. They find an improvement in retrieval stability for fine mode dominated aerosols, and a high sensitivity to particle shape and real part of the refractive index due to the use of polarimetry. The sensitivity of polarimetric measuremednts to the non-sphericity of particle is also shown in Dubovik et al. (2002). Xu and Wang (2015) investigate the information content gained by including polartimetric measurements in almucantar and principal plane scans. Their research retrieval algorithm was applied to real world AERONET measurements in Xu et al. (2015), and showed an improvement over a pure radiance-based retrieval. The retrieval error was significantly reduced for size distribution parameters (50 %), refractive index (10 % to 30 %) and single scattering albedo (10 % to 40 %).

Várnai et al. (2017) did a statistical analysis of averaged MODIS satellite and MERRA-2 reanalysis data and found a positive correlation between cloud fraction and AOD over most of the globe. AOD was increased 30 % to 50 % on cloudier than average days. Also a modification of particle size in the vicinity of clouds was observable, although not consistent over all regions. These effects are attributed to several factors, including microphysical and 3D radiative processes. Yang et al. (2014) observed an enhancement in CALIPSO lidar backscatter signal at up to 5 km from clouds. Similarly, in a multi-instrument field experiment Eck et al. (2014) found enhancements of the AOD due to cumulus cloud development. This effect ranged up to 2.5 km from the cloud edge. Koren et al. (2009) performed microphysical simulations to determine the distribution of water in cumulus cloud fields and its dependency on aerosol.

Also, there have been studies regarding the influence of 1D or scalar approximations of the radiative transfer calculations. Detailed studies of 3D radiative effects on observations from MODIS and ASTER have been performed by Wen et al. (2007). They discovered errors between 50 % to 140 % in retrieved AOD when the 1D approximation is used for the radiative transfer. Concerning polarization, Mishchenko et al. (1994) and Emde and Mayer (2018) have shown that the scalar approximation of the vector radiative transfer equation induces errors in the total radiance of satellite observations.

Polarimetric instruments require an additional calibration. Prior work on this has been done for polarized CIMEL CE318-DP sun photometers by Li et al. (2014, 2010,

2018). In this work, an alternative approach overcoming some of their limitations and reducing the number of required steps by simultaneously determining the polarizers' efficiencies and angles is presented.

Additionally, an aerosol retrieval has been developed. It uses multi-spectral, multi-angle, polarized sky radiance measurements to retrieve optical depth, effective radius and refractive index of the aerosols in two size distribution modes. To be applicable to partly cloudy situations, it is extended by a method for removing measurements from cloud-contaminated sky regions. The impact of nearby clouds on the retrieval results are studied. Furthermore, the influence of clouds on radiance and polarization in their vicinity by 3D radiative effects is investigated. Understanding the implications of 3D radiative transfer is necessary to later discriminate them from cloud-induced modifications in the microphysics.

Our new methodology was applied to polarized radiance measurements from the SSARA polarized scanning sun and sky radiometer, taken during the A-LIFE (Absorbing aerosol layers in a changing climate: aging, LIFEtime and dynamics) field campaign. It took place in Cyprus during April 2017 and included ground-based components, such as lidar and radar systems, radiometers, and in situ samplers at Paphos and Limassol. Additionally, a research aircraft with in situ instrumentation was operated from Paphos airport. The goal of the A-LIFE project is to investigate the effects of aerosol on the earth's radiation budget, cloud development and atmospheric dynamics, with a focus on desert dust and absorbing aerosols, such as black carbon from biomass burning. SSARA has previously been employed in the SAMUM-1 and 2, and the SALTRACE field campaigns that had similar goals (Toledano et al., 2009, 2011).

This work is structured as follows: In Chapter 2 the theoretical concepts needed are introduced. These include the radiometric quantities used, the basics of vector radiative transfer and aerosol physics. The forward models used for the numerical studies and the inversion are presented in Chapter 3, together with the retrieval. Furthermore, the SSARA sun photometer is described, together with the necessary calibration methods. This includes the novel polarimetric calibration and mount correction methods. Chapter 4 contains two parts. In Section 4.1, the findings from the numerical studies with synthetic clouds are presented. The retrieval results for SSARA measurements taken during the A-LIFE field campaign are shown in Section 4.2. Here, three days are studied in more detail. Chapter 5 summarizes the findings summarizes the findings and gives an outlook to further studies. The appendix consists of a short primer for quaternion algebra necessary for the mount calibration in Appendix A, and the retrieval results for all days not discussed in the case studies before in Appendix B.

2. Theoretical background

2.1. Vector radiative transfer

2.1.1. Radiometry

In the following, the basic radiometric quantities used in this work will be presented. The description closely follows that found in Wallace and Hobbs (2006).

The basic measure for radiation used here is *spectral radiance I_λ*, also referred to as *spectral intensity.* It describes the amount of energy Q passing through surface area A oriented normal to the direction of the radiation in a solid angle interval $\mathrm{d}\Omega$ around a given direction over a time t by electromagnetic radiation of wavelength λ. In infinitessimal form, the definition of the spectral intensity is

$$I_\lambda = \frac{\mathrm{d}^4 Q}{\mathrm{d}A \ \mathrm{d}\Omega \ \mathrm{d}\lambda \ \mathrm{d}t} \ . \tag{2.1}$$

Its unit is therefore $\mathrm{W\,m^{-2}\,sr^{-1}\,nm^{-1}}$. Integrating I_λ over the solid angle of the entire hemisphere above the surface A, yields the *spectral irradiance F_λ*. It is a measure of the energy passing through the oriented surface per unit time. Here, the geometric "spreading" of the surface under slanted observation has to be considered, adding the cosine of the zenith angle ϑ,

$$F_\lambda = \int_{2\pi} \cos\vartheta \ I_\lambda \ \mathrm{d}\Omega \tag{2.2}$$

The unit of the spectral irradiance is $\mathrm{W\,m^{-2}\,nm^{-1}}$. For the spectral radiance and irradiance the wavelength–dependence can be integrated over a specific wavelength range. The resulting quantities are plainly named *radiance I* and *irradiance F*. In later chapters, spectral measurements are descibed in units of radiance. In these cases, the integral always has to be performed over the spectral filter transmission function $T(\lambda)$. For monochromatic simulations, this is a delta–function, but for real measurements, it is more complex.

$$I = \int_0^\infty T(\lambda) I_\lambda \ \mathrm{d}\lambda \tag{2.3}$$

The main source of visible radiation in atmospheric radiative transfer is the central star of the planetary system under consideration, here the sun. It can be

described as a *blackbody* with a surface temperature of about $5770\,\mathrm{K}$. The spectral radiance of a blackbody I_λ^{BB} is given by *Planck's law*,

$$I_\lambda^{\mathrm{BB}}(T) = \frac{2hc^2}{\lambda^5}\left[\exp\left(\frac{hc}{\lambda k_{\mathrm{B}} T}\right) - 1\right]^{-1},\tag{2.4}$$

with *Planck's constant h*, the vacuum speed of light *c*, and *Boltzmann constant* k_{B}. T is the effective surface temperature of the body. The sun is a so–called *isotropic emitter*, meaning that its radiation is emitted equally in all directions. By performing the appropriate integration of Eq. (2.2), it can be shown that for isotropic emitters $F_\lambda = \pi I_\lambda$. Using this identity and integrating Eq. (2.4) over the entire wavelength range yields the *Stefan–Boltzmann* law, describing a blackbody's emission,

$$\frac{\Phi(T)}{A} = \sigma_{\mathrm{SB}} T^4 = \frac{2\pi^5 k_{\mathrm{B}}^4}{15 h^3 c^2} T^4.\tag{2.5}$$

where σ_{SB} is known as the *Stefan–Boltzmann* constant and Φ the total radiant power emitted by the blackbody in W through its surface A. The *solar constant* is defined as the irradiance of the solar radiation passing a sphere with the mean orbital radius of the planet. For the earth, its current values is about $1368\,\mathrm{W\,m^{-2}}$.

2.1.2. Stokes–Müller formalism
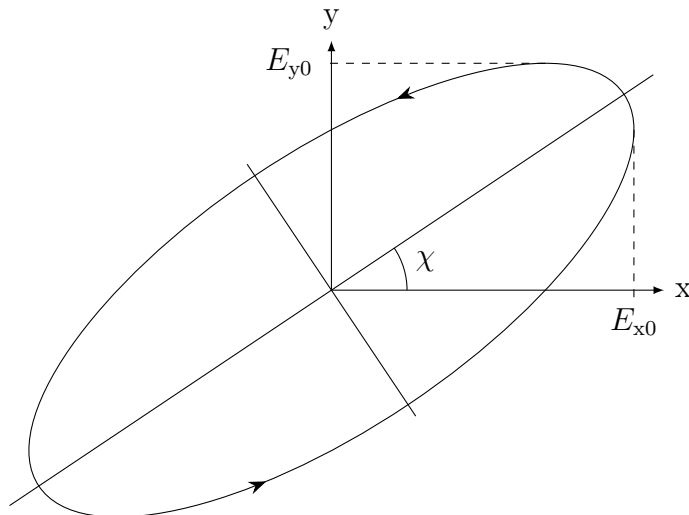
Definition of Stokes vector

Figure 2.1.: Polarization ellipse

Polarized radiance is described by the so-called *Stokes vector*. Its derivation can be found – for example – in Chandrasekhar (1950) and Collett (1968). To this end, the radiation is defined as two perpendicular electromagnetic waves with the same frequency propagating in the positive z direction. The electric field oscillates in x and y direction.

$$E_{\text{x}}(t) = E_{\text{x0}} \cos(\omega t + \delta_{\text{x}}) \tag{2.6}$$

$$E_{\text{y}}(t) = E_{\text{y0}} \cos(\omega t + \delta_{\text{y}}) \tag{2.7}$$

E_{x0} and E_{y0} are the amplitudes of the electric field in x and y direction, respectively. ω is the circular frequency of the wave, with $\omega = 2\pi f$. δ_{x} and δ_{y} are phase factors for the respective components. From this, the polarization ellipse (shown in Fig. 2.1) can be derived:

$$\left(\frac{E_{\text{x}}(t)}{E_{\text{x0}}}\right)^2 + \left(\frac{E_{\text{y}}(t)}{E_{\text{y0}}}\right)^2 - \frac{2E_{\text{x}}(t)\,E_{\text{y}}(t)\cos\delta}{E_{\text{x0}}E_{\text{y0}}} = \sin^2\delta \tag{2.8}$$

with the relative phase difference $\delta = \delta_{\text{y}} - \delta_{\text{x}}$. The components can now be averaged over time. This yields the definition for the components S_{i} of the Stokes vector $\mathbf{S}$

$$(E_{\text{x0}} + E_{\text{y0}})^2 = (E_{\text{x0}} - E_{\text{y0}})^2 + (2E_{\text{x0}}E_{\text{y0}}\cos\delta)^2 + (2E_{\text{x0}}E_{\text{y0}}\sin\delta)^2 \tag{2.9}$$

$$S_0^2 = S_1^2 + S_2^2 + S_3^2 \tag{2.10}$$

$$\mathbf{S} := \begin{pmatrix} S_0 \\ S_1 \\ S_2 \\ S_3 \end{pmatrix} = \begin{pmatrix} I \\ Q \\ U \\ V \end{pmatrix} = \begin{pmatrix} E_{\text{x0}}^2 + E_{\text{y0}}^2 \\ E_{\text{x0}}^2 - E_{\text{y0}}^2 \\ 2E_{\text{x0}}E_{\text{y0}}\cos\delta \\ 2E_{\text{x0}}E_{\text{y0}}\sin\delta \end{pmatrix} \tag{2.11}$$

I describes the intensity or radiance of the radiation. The components Q and U give the intensity of linear polarized light in two planes rotated by 45°. V corresponds to circular polarized radiation. The polarized radiances given in this thesis are normalized to the extraterrestrial solar flux and thus unitless.

For only partially polarized light, Eq. (2.10) becomes an inequality relation

$$S_0^2 \geq S_1^2 + S_2^2 + S_3^2\,. \tag{2.12}$$

Due to its low abundance in atmospheric radiation (de Haan et al., 1987; Emde et al., 2010), circular polarization will be neglected here. In the context of linear polarized radiation, two definitions will be used. The linear polarized intensity (Eq. (2.13)) and the degree of linear polarization (DoLP, Eq. (2.14)).

$$I_{\text{LP}} = \sqrt{Q^2 + U^2} \leq I \tag{2.13}$$

$$\eta = \frac{\sqrt{Q^2 + U^2}}{I} = \frac{I_{\text{LP}}}{I} \tag{2.14}$$

Müller matrices

In the *Stokes–Müller* formalism, interactions with optical components or the atmosphere are described by left multiplication of the Stokes vector of the incoming radiation $\mathbf{S}_{\text{in}}$ with the appropriate real 4×4 Müller matrices $\widehat{\mathbf{M}}_1$ to $\widehat{\mathbf{M}}_{\text{n}}$,

$$\mathbf{S}_{\text{out}} = \widehat{\mathbf{M}}_{\text{n}} \cdots \widehat{\mathbf{M}}_1 \cdot \mathbf{S}_{\text{in}} \,. \tag{2.15}$$

A selection of these matrices for different optical components can be found in Bass et al. (2010, Chap. 22). A linear polarizer, for instance, can be described as a linear diattenuator, meaning its attenuation differs for light polarized parallel and perpendicular to its orientation. The corresponding Müller matrix is

$$\widehat{\mathbf{LD}}_{\updownarrow} = \frac{1}{2} \begin{pmatrix} (k_0 + k_1) & (k_1 - k_0) & 0 & 0 \\ (k_1 - k_0) & (k_0 + k_1) & 0 & 0 \\ 0 & 0 & 2\sqrt{k_0 k_1} & 0 \\ 0 & 0 & 0 & 2\sqrt{k_0 k_1} \end{pmatrix} \,. \tag{2.16}$$

k_0 and k_1 are the transmission values for the filter in the direction parallel and perpendicular to its orientation, respectively. Additionally, the component might be rotated around the direction of light propagation by the angle ϑ. This is described by a real 4×4 rotation matrix $\widehat{\mathbf{R}}$.

$$\widehat{\mathbf{M}}_{\vartheta} = \widehat{\mathbf{R}}\,(\vartheta)^{\text{T}}\,\widehat{\mathbf{M}}\widehat{\mathbf{R}}\,(\vartheta) \tag{2.17}$$

$$\text{with} \qquad \widehat{\mathbf{R}}\,(\vartheta) = \begin{pmatrix} 1 & 0 & 0 & 0 \\ 0 & \cos(2\vartheta) & -\sin(2\vartheta) & 0 \\ 0 & \sin(2\vartheta) & \cos(2\vartheta) & 0 \\ 0 & 0 & 0 & 1 \end{pmatrix}, \tag{2.18}$$

$$\text{and} \qquad \widehat{\mathbf{R}}\,(\vartheta)^{-1} = \widehat{\mathbf{R}}\,(-\vartheta) = \widehat{\mathbf{R}}\,(\vartheta)^{\text{T}} \tag{2.19}$$

The resulting Müller matrix $\widehat{\mathbf{LD}}$ for a linear diattenuator rotated by an arbitrary angle ϑ is

$$\widehat{\mathbf{LD}}\,(\vartheta) =$$
$$\frac{1}{2} \begin{pmatrix} a & b\cos(2\vartheta) & b\sin(2\vartheta) & 0 \\ b\cos(2\vartheta) & a\cos^2(2\vartheta) + c\sin^2(2\vartheta) & (a-c)\cos(2\vartheta)\sin(2\vartheta) & 0 \\ b\sin(2\vartheta) & (a-c)\cos(2\vartheta)\sin(2\vartheta) & a\sin^2(2\vartheta) + c\cos^2(2\vartheta) & 0 \\ 0 & 0 & 0 & c \end{pmatrix}, \tag{2.20}$$

with $a = k_0 + k_1$, $b = k_0 - k_1$, and $c = 2\sqrt{k_0 k_1}$.

2.1.3. Radiative transfer equation

The *vector radiative transfer equation* (VRTE) is an integro–differential equation, describing the transport of polarized monochromatic radiation in the atmosphere. In the most general case of three dimensional polarized radiative transfer, it is defined as follows (see Emde and Mayer, 2018):

$$(\mathbf{n} \cdot \nabla) \mathbf{I}_\lambda (\mathbf{x}, \mathbf{n}) = -\widehat{\beta}_{\text{ext}} (\mathbf{x}) \mathbf{I}_\lambda (\mathbf{x}, \mathbf{n}) + \frac{\beta_{\text{scat}}}{4\pi} \int_{4\pi} \widehat{\mathbf{Z}} (\mathbf{n}', \mathbf{n}) \mathbf{I}_\lambda (\mathbf{x}, \mathbf{n}') \, \mathrm{d}\mathbf{n}' \qquad (2.21)$$

The equation describes the change of the specral radiance given by the Stokes vector $\mathbf{I}_\lambda$ at location $\mathbf{x}$ in direction of $\mathbf{n}$ along an the infinitesimal path length. $\mathbf{n}$ and $\mathbf{n}$' are normalized. Contributions to this are the scattering or absorption out of the light path (also referred to as extinction), and the scattering of light into the direction along the light path. The contribution from blackbody radiation is neglected here, as it is only relevant in the infrared regime for the earth's atmosphere, due to its low temperature. β_{abs} and β_{scat} are the absorption and scattering coeffincients, respectively. The extinction coefficient $\beta_{\text{ext}} = \beta_{\text{abs}} + \beta_{\text{scat}}$ is used to shorten the first term. As the absorption coefficient can depend on the polarization state, $\widehat{\beta}_{\text{ext}}$ is described as a matrix. The for polarization–independent absorption, it becomes a scalar $\beta_{\text{ext}} = \widehat{\beta}_{\text{ext},11}$ These coefficients can be calculated from the respective cross-sections σ_{scat} and σ_{abs}, and the particle's volume number density $n_{\text{V}} = \mathrm{d}N/\mathrm{d}V$. Alternatively, the geometric or areal cross-section of the particles σ_{g} can be used, together with a absorption or scattering efficiency Q_{abs} or Q_{scat} (Hansen and Travis, 1974). Another useful quantity is the *single scattering albedo* ω_0, defined by Eq. (2.24).

$$\beta_{\text{abs/scat}} = \sigma_{\text{abs/scat}} \cdot n_{\text{v}} = Q_{\text{abs/scat}} \cdot \sigma_{\text{g}} \cdot n_{\text{v}} \qquad (2.22)$$

$$\beta_{\text{ext}} = \beta_{\text{scat}} + \beta_{\text{abs}} \qquad (2.23)$$

$$\Rightarrow \quad \omega_0 = \frac{\beta_{\text{scat}}}{\beta_{\text{ext}}} = \frac{\beta_{\text{scat}}}{\beta_{\text{scat}} + \beta_{\text{abs}}} \qquad (2.24)$$

The extinction component in Eq. (2.21) has a negative sign, signifying that radiation is "removed" by scattering out of the light path or absorption.

The second term in Eq. (2.21) describes light scattered into the light path, contributing positively to the differential radiance. It mainly consists of an integral over the radiances coming from every direction, weighted by the matrix $\widehat{\mathbf{Z}} (\mathbf{n}', \mathbf{n})$, giving the probability of scattering radiation coming from direction $\mathbf{n}'$ to $\mathbf{n}$. This direction is given by an zenith angle ϑ and an azimuth φ. The matrix $\widehat{\mathbf{Z}}$ is a transformed version of the scattering phase matrix $\widehat{\mathbf{P}}$:

$$\widehat{\mathbf{Z}} (\Omega', \Omega) = \widehat{\mathbf{R}} (i_2) \widehat{\mathbf{P}} (\theta) \widehat{\mathbf{R}} (i_1) \qquad (2.25)$$

$\widehat{\mathbf{R}}$ is a rotation matrix – as defined in Eq. (2.18) – transforming the scattering process to the scattering frame of reference. For spherical and randomly oriented particles, this reduces the directional dependence to only the scattering angle θ. This frame of reference is defined be the scattering plane including the incoming and the outgoing direction of the radiation, and a vector perpendicular to it. The rotation angles i_1 and i_2 are defined in Emde et al. (2010) as

$$\cos(\theta) = \mathbf{n}' \cdot \mathbf{n} \tag{2.26}$$

$$\cos(i_1) = (\mathbf{n}' \times \mathbf{e}_z) \cdot (\mathbf{n}' \times \mathbf{n}) \tag{2.27}$$

$$\cos(i_2) = (\mathbf{n} \times \mathbf{e}_z) \cdot (\mathbf{n} \times \mathbf{n}') \tag{2.28}$$

with the normalized vector in z direction $\mathbf{e}_z = (0, 0, 1)^T$

The VRTE can be simplified to the scalar RTE by just considering the first component of the Stokes vector. The scattering matrix consequently also reduces to a scaler function, which is the P_{11}–element of $\widehat{\mathbf{P}}$. However, this approximation induces errors in the radiative transfer (see Emde and Mayer, 2018; Mishchenko et al., 1994).

Limiting the problem to homogeneous, plane–parallel atmopsheres, a simplified version of Eq. (2.21) can be used (see Mishchenko et al., 1994):

$$\frac{d\mathbf{I}_\lambda(\mathbf{n})}{ds} = -\beta_{\text{ext}}\mathbf{I}_\lambda(\Omega) + \frac{\beta_{\text{scat}}}{4\pi}\int_{4\pi}\widehat{\mathbf{Z}}(\mathbf{n}', \mathbf{n})\,\mathbf{I}_\lambda(\mathbf{n}')\,d\mathbf{n}' \tag{2.29}$$

now with ds describing the infinitesimal path length along which the Stokes vector in direction $\mathbf{n}$ changes. The direction $\mathbf{n}$ is described by the zenith angle ϑ and the azimuth angle φ. In the atmosphere, the optical properties mainly vary along the z direction, so a coordinate transformation from ds to dz can be performed, using the zenith angle of the incoming radiation ϑ_0. Incorporating the optical depth $\tau = \beta_{\text{ext}}s$, we end up in the τ coordinate system. For ground–based observations we choose τ_0 to be at the top of the atmosphere and increasing downwards (see Fig. 2.2).

Introducing the optical depth $d\tau = \beta_{\text{ext}}ds$ and $\mu_0 = \cos\vartheta_0 = \frac{dz}{ds}$ Eq. (2.29) can be transformed into the following:

$$\mathbf{I}_\lambda(\tau, \mathbf{n}_v) = \mathbf{I}_\lambda^{\text{dir}}(\tau, \mathbf{n}_v) + \mathbf{I}_\lambda^{\text{scat}}(\tau, \mathbf{n}_v) \tag{2.30}$$

$$= \mathbf{I}_\lambda^0 \exp\left(-\frac{\tau}{\mu_0}\right)\delta(\mathbf{n}_v, \mathbf{n}_0)$$

$$+ \frac{1}{\mu_v}\int_0^\tau \frac{\omega_0}{4\pi}\int_{4\pi}\widehat{\mathbf{P}}(\mathbf{n}', \mathbf{n}_v)\,\mathbf{I}_\lambda(\tau', \mathbf{n}')\,d\mathbf{n}'\exp\left(-\frac{\tau - \tau'}{\mu_v}\right)d\tau' \tag{2.31}$$

$\mathbf{n}_0$ and $\mathbf{n}_v$ are the sun and viewing directions, respectively. μ_0 and μ_v are the cosines of the corresponding solar and viewing zenith angles ϑ_0 and ϑ_v. The radiance

at the optical depth τ is now the sum of the direct ($\mathbf{I}_\lambda^{\mathrm{dir}}$) and the scattered radiation ($\mathbf{I}_\lambda^{\mathrm{scat}}$). This definition of the direct radiation is called the *Bouguer–Lambert–Beer* law:

$$\mathbf{I}_\lambda\left(\tau\right) = \mathbf{I}_\lambda^0 \exp\left(-m\tau\right) \tag{2.32}$$

with the *airmass factor* m, which here is $1/\mu_0$. $\mathbf{I}_\lambda^0$ is the spectral intensity of the radiation entering the medium. In atmospheric radiative transfer, this is given by the solar constant. The scattering contribution can further be devided into single and multiple scattering components, $\mathbf{I}_\lambda^{\mathrm{scat}} = \mathbf{I}_\lambda^{\mathrm{ss}} + \mathbf{I}_\lambda^{\mathrm{ms}}$. Solving Eq. (2.31) is analytically impossible, as the sought $\mathbf{I}_\lambda$ also appears on the right hand side inside the τ–integal.

Single scattering
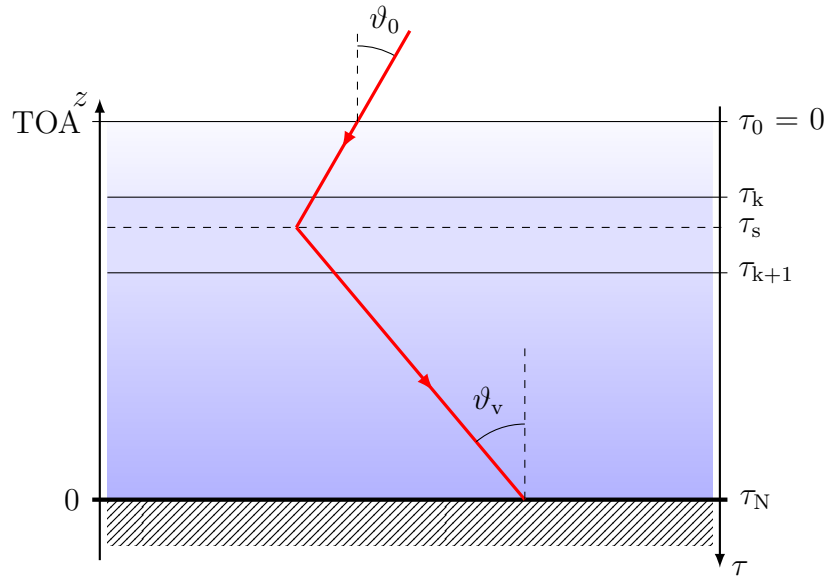
Figure 2.2.: Single scattering geometry. Radiation entering the atmosphere under the solar zenith angle ϑ_0 is scattered at an optical depth τ_{s} into the direction of the viewing zenith angle ϑ_{v}. The optical properties are discretized in layers in z direction.

The geometry for single scattering is shown in Fig. 2.2. For its contribution $\mathbf{I}_\lambda^{\mathrm{ss}}$ an analytic solution exists, as the source radiance in the τ–integral on the right

hand side is replaced by the direct radiation $\mathbf{I}_\lambda^{\text{dir}}$:

$$\mathbf{I}_\lambda^{\text{ss}}(\tau, \mathbf{n}_\text{v}) = \frac{1}{4\pi\mu_\text{v}} \int_0^\tau \omega_0 \int_{4\pi} \widehat{\mathbf{Z}}(\mathbf{n}', \mathbf{n}_\text{v}) \mathbf{I}_\lambda^{\text{dir}}(\tau_\text{s}, \mathbf{n}') \, \text{d}\mathbf{n}' \, \exp\left(-\frac{\tau - \tau_\text{s}}{\mu_\text{v}}\right) \text{d}\tau_\text{s} \qquad (2.33)$$

$$= \frac{\mathbf{I}_\lambda^0}{4\pi\mu_\text{v}} \int_0^\tau \omega_0 \widehat{\mathbf{Z}}(\mathbf{n}_0, \mathbf{n}_\text{v}) \exp\left(-\frac{\tau_\text{s}}{\mu_0} - \frac{\tau - \tau_\text{s}}{\mu_\text{v}}\right) \text{d}\tau_\text{s} \qquad (2.34)$$

Note that Fig. 2.2 only depicts scattering at a single optical depth τ_s. However in Eq. (2.34), it has be integrated over to account for scattering taking place throughout the depth of the atmosphere.

Computationally, the atmosphere is represented by discrete plane–parallel layers with optical parameters $\widehat{\mathbf{P}}_\text{k}$, $\Delta\tau_\text{k}$ and ω_k. With this, the integral in Eq. (2.34) can be replaced by a sum over all N layers and an integral within the layer k.

$$\mathbf{I}_\lambda^{\text{ss}}(\tau, \mathbf{n}_\text{v}) = \frac{\mathbf{I}_\lambda^0}{4\pi\mu_\text{v}} \sum_{k=0}^{N-1} \omega_{0,\text{k}} \widehat{\mathbf{Z}}_\text{k}(\mathbf{n}_0, \mathbf{n}_\text{v}) \int_0^{\Delta\tau_\text{k}} \exp\left(-\frac{\tau_\text{k} + \tau'}{\mu_0} - \frac{\tau - \tau_\text{k} - \tau'}{\mu_\text{v}}\right) \text{d}\tau'$$

$$(2.35)$$

$$= \frac{\mathbf{I}_\lambda^0}{4\pi} \frac{\mu_0}{\mu_0 - \mu_\text{v}} \sum_{k=0}^{N-1} \omega_{0,\text{k}} \widehat{\mathbf{Z}}_\text{k}(\mathbf{n}_0, \mathbf{n}_\text{v})$$

$$\cdot \exp\left(-\frac{\tau_\text{k}}{\mu_0} - \frac{\tau - \tau_{\text{k}+1}}{\mu_\text{v}}\right) \left[\exp\left(-\frac{\Delta\tau_\text{k}}{\mu_0}\right) - \exp\left(-\frac{\Delta\tau_\text{k}}{\mu_\text{v}}\right)\right] \qquad (2.36)$$

Multiple scattering

For solving the multiple–scattering contribution, no analytic solution exists. However, there are some numerical solutions. In this work, two approaches are used.

The first one is Monte–Carlo sampling, where a lightpath (often called *photon*) is simulated. The scattering phase functions and Bouguer–Lambert–Beer law are interpreted as probability functions. The integral over these is done by statistically sampling the corresponding probability density functions. By taking a multitude of light paths, we get an approximate solution of the integral. The inherent noise in this method can be reduced by using more lightpaths or a variety of variance reduction methods. This process is computationally rather expensive and therefore not fast enough for use in a inverse methods. However – given sufficient computing power – it is the most accurate method, as it is relatively easy to realistically model physical processes, such as polarization dependence of optical processes. It can be used for 3D radiative transfer with horizontally and vertically inhomogeneous optical properties including clouds, and also spherical coordinate systems. Therefore it can be used to simulate reference measurements for numerical studies.

The other method used here is the so–called *doubling–adding* method originally proposed by (van de Hulst, 1981). Here, the idea is to split a layer k into many

sublayers with identical optical properties. These sublayers are supposed to be so thin, that multiple scattering within them is not relevant. Therefore, their transmission and reflection coefficients of a homogeneous layer can be calculated using only single scattering (Hansen, 1969; Hovenier, 1969). These solutions can then be used to determine the coefficients for a combined layer (Hansen, 1971; Hovenier, 1971). This process is repeated until all layers of the atmosphere are used. The method solves the polarized radiative transfer equation. Additionally, the $d\Omega$ integral in Eq. (2.31) has to be discretized into sums. For this, the φ-dependence is expanded in terms of Fourier modes. For the ϑ-dependence, Gaussian quadrature is used for $\mu = \cos(\vartheta)$. All this results in a system of linear equations that can be solved using standard methods (Howell and Jacobowitz, 1970; Twomey et al., 1966). Even though this method is comparatively fast – making it suitable for inversion schemes – no extension to 3D exists so far and only plane–parallel atmospheres are supported. Also, small errors arise the single scattering assumption within the sublayers.

2.2. Atmospheric scattering processes

2.2.1. Rayleigh scattering

Solar radiation reaching the top of the earths atmosphere is unpolarized. However, scattering processes in the atmosphere can create polarized light. One such process is *Rayleigh scattering* caused by the scattering on the bound electrons of gas molecules and atoms. The cross-section for Rayleigh scattering in the atmosphere is investigated by many papers (e. g. Bodhaine et al., 1999; Fröhlich and Shaw, 1980; Nicolet, 1984). The most recent, Bodhaine et al. (1999), gives an overview and recommends the following formula with the characteristic λ^{-4}–dependence:

$$\sigma_{\text{scat}} = \frac{24\pi^3}{\lambda^4 N_{\text{s}}^2} \left(\frac{n^2 - 1}{n^2 + 2} \right)^2 \frac{6 + 3\delta}{6 - 7\delta} \tag{2.37}$$

with the depolarization factor δ, the refractive index n and the molecular density of air N_{s}. δ depends on the so–called *King factor* of air F_{air}. The exact calculation of F_{air}, N_{s} and n are described in the aforementioned paper. However, it also gives an approximate function for dry air with a CO_2 concentration of 360 ppm:

$$\sigma_{\text{scat}} = \frac{1.045\,599\,6 - 341.290\,61\,\mu\text{m}^2\,\lambda^{-2} - 0.902\,308\,50\,\mu\text{m}^{-2}\,\lambda^2}{1 - 0.002\,705\,988\,9\,\mu\text{m}^2\,\lambda^{-2} - 85.968\,563\,\mu\text{m}^{-2}\,\lambda^2} \cdot 10^{-28}\,\text{cm}^2$$
$$\tag{2.38}$$

The phase matrix for Rayleigh scattering in the atmosphere can be found in

Hansen and Travis (1974) and is given by

$$
\widehat{\mathbf{P}}\left(\theta\right) = \Delta
\begin{pmatrix}
\frac{3}{4}\left(1+\cos^2\theta\right) & -\frac{3}{4}\sin^2\theta & 0 & 0 \\
-\frac{3}{4}\sin^2\theta & \frac{3}{4}\left(1+\cos^2\theta\right) & 0 & 0 \\
0 & 0 & \frac{3}{2}\cos\theta & 0 \\
0 & 0 & 0 & \Delta'\frac{3}{2}\cos\theta
\end{pmatrix}
$$
$$
+ \left(1-\Delta\right)
\begin{pmatrix}
1 & 0 & 0 & 0 \\
0 & 0 & 0 & 0 \\
0 & 0 & 0 & 0 \\
0 & 0 & 0 & 1
\end{pmatrix} ,
\tag{2.39}
$$

with the scattering angle θ and

$$
\Delta = \frac{1-\delta}{1+\delta/2} , \qquad \Delta' = \frac{1-2\delta}{1-\delta} .
\tag{2.40}
$$

2.2.2. Aerosol scattering

The remote sensing of aerosols is based on their scattering and absorption properties. For randomly oriented aerosol particles, the scattering matrix can be described by six functions (van de Hulst, 1981). It is given by

$$
\widehat{\mathbf{P}}\left(\theta\right) =
\begin{pmatrix}
P_{11}\left(\theta\right) & P_{12}\left(\theta\right) & 0 & 0 \\
P_{12}\left(\theta\right) & P_{22}\left(\theta\right) & 0 & 0 \\
0 & 0 & P_{33}\left(\theta\right) & P_{34}\left(\theta\right) \\
0 & 0 & -P_{34}\left(\theta\right) & P_{44}\left(\theta\right)
\end{pmatrix} .
\tag{2.41}
$$

If the particles are also spherical, this number reduces to four, as then $P_{11} = P_{22}$ and $P_{33} = P_{44}$. Scattering by water droplets can polarize radiation in much the same way as aerosols.

Depending on the *size parameter* $x = 2\pi r/\lambda$ describing the ratio between particle radius r and wavelength λ, the scattering matrix and cross-section can either be determined either by Mie ($x \approx 1$) or geometric optics calculations ($x \gg 1$).

2.3. Aerosol properties

To describe the number of aerosol particles in a given size range $\mathrm{d}r$, a *number density distribution* $n\left(r\right)$ for the aerosol particles is required. It is normalized to the total particle count N.

$$
\int_0^\infty n\left(r\right)\,\mathrm{d}r = N \iff \frac{\mathrm{d}N\left(r\right)}{\mathrm{d}r} = n\left(r\right)
\tag{2.42}
$$

Common choices for the number density function are gamma, normal, and lognormal distributions. In this work, aerosols are assumed to have a *lognormal* number size distribution. According to the *OPAC* library (Hess et al., 1998), it is defined as

$$n\left(r\right) = \frac{N}{\sqrt{2\pi}\, r\, \ln\left(\sigma_{\mathrm{n}}\right)} \exp\left[-\frac{1}{2}\left(\frac{\ln\left(r\right) - \ln\left(r_{\mathrm{n}}\right)}{\ln\left(\sigma_{\mathrm{n}}\right)}\right)^2\right], \qquad (2.43)$$

where r_{n} is the lognormal mode radius and σ_{n} its standard deviation, which is related to the width of the distribution. N is the total number of particles. As described in Hansen and Travis (1974), particle interaction with radiation can be more aptly described by the *effective radius r_{eff}*. It can be derived from the *mean radius $\bar{r}$* by weighting it with the *scattering cross-section σ_{scat}* of the scatterer in question. The resulting *mean radius for scattering r_{scat}* is the most meaningfull for describing scattering processes, but it involves the highly specific *scattering efficiency Q_{scat}*. Neglecting this quantity by setting it to 1 yields the effective radius.

$$\bar{r} = \frac{\int_0^\infty r \cdot n\left(r\right)\mathrm{d}r}{\int_0^\infty n\left(r\right)\mathrm{d}r} = \frac{1}{N}\int_0^\infty r \cdot n\left(r\right)\mathrm{d}r \qquad (2.44)$$

$$r_{\mathrm{scat}} = \frac{\int_0^\infty r \cdot \pi r^2 Q_{\mathrm{scat}} \cdot n\left(r\right)\mathrm{d}r}{\int_0^\infty \pi r^2 Q_{\mathrm{scat}} \cdot n\left(r\right)\mathrm{d}r} = \frac{1}{G}\int_0^\infty r \cdot \pi r^2 Q_{\mathrm{scat}} \cdot n\left(r\right)\mathrm{d}r \qquad (2.45)$$

$$r_{\mathrm{eff}} = \frac{\int_0^\infty r \cdot \pi r^2 \cdot n\left(r\right)\mathrm{d}r}{\int_0^\infty \pi r^2 \cdot n\left(r\right)\mathrm{d}r} = \frac{\mathcal{M}_3}{\mathcal{M}_2} = \frac{1}{G}\int_0^\infty r \cdot \pi r^2 \cdot n\left(r\right)\mathrm{d}r \qquad (2.46)$$

Here, $\mathcal{M}n$ describes the nth moment of the number density distribution. Along the same lines, a measure for the width of the size distribution can be found by calculating the second central moment of the number density distribution. This leads to the definition of the *effective variance v_{eff}*.

$$v_{\mathrm{eff}} = \frac{1}{r_{\mathrm{eff}}^2}\frac{\int_0^\infty \left(r - r_{\mathrm{eff}}\right)^2 \cdot n\left(r\right)\mathrm{d}r}{\int_0^\infty n\left(r\right)\mathrm{d}r} = \frac{1}{G \cdot r_{\mathrm{eff}}^2}\int_0^\infty \left(r - r_{\mathrm{eff}}\right)^2 \cdot n\left(r\right)\mathrm{d}r \qquad (2.47)$$

Both, effective radius and variance, can be calculated for the lognormal distribution as follows,

$$r_{\mathrm{eff}} = r_{\mathrm{n}} \cdot \left(1 + v_{\mathrm{eff}}\right)^{5/2} \iff r_{\mathrm{n}} = \frac{r_{\mathrm{eff}}}{\left(1 + v_{\mathrm{eff}}\right)^{5/2}}, \qquad (2.48)$$

$$v_{\mathrm{eff}} = \exp\left[\ln^2\left(\sigma_{\mathrm{n}}\right)\right] - 1 \iff \sigma_{\mathrm{n}} = \exp\left[\sqrt{\ln\left(1 + v_{\mathrm{eff}}\right)}\right]. \qquad (2.49)$$

AERONET products contain information about aerosol size distribution parameters. Instead of the number size distribution $n(r)$, the volume size distribution $v(r) = \frac{\mathrm{d}V}{\mathrm{d}r}$ is taken to have a lognormal distribution (Dubovik et al., 2006). This gives the *volume mode radius* r_v and the corresponding standard deviation σ_v. The volume mode radius can be converted to number mode radius and effective radius by

$$r_\mathrm{n} = r_\mathrm{v} \cdot \exp\left(-3 \ln^2(\sigma_\mathrm{v})\right) , \tag{2.50}$$

$$r_\mathrm{eff} = r_\mathrm{v} \cdot \exp\left(-\frac{1}{2} \ln^2(\sigma_\mathrm{v})\right) . \tag{2.51}$$

The standard deviations of both distributions are equal ($\sigma_\mathrm{n} = \sigma_\mathrm{v}$). These conversion relations of different parametrizations of the size distribution can, for instance, be found in Chýlek et al. (1992) and Li et al. (2015).

The complex refractive index $m = m_\mathrm{r} + i\, m_\mathrm{i}$ of aerosols varies by chemical composition and even their source region (Dubovik et al., 2002). The imaginary part m_i is directly related to the absorption cross-section and therefore also the single scattering albedo ω_0. It can therefore be used to identify absorbing aerosols, such as black carbon.

The aerosol optical properties from Dubovik et al. (2006) are used in the forward model of the retrieval. It contains the six scattering matrix component functions described in Section 2.2.2 for scattering angles from 0° to 180° with a resolution of 1°. Furthermore, it contains the scattering (σ_sca) and extinction cross sections (σ_ext). These monodisperse optical properties have been determined by combining Mie calculations with geometric optics for larger particles. They are tabulated for a number of input parameters. These are the size parameter $x = 2\pi r/\lambda$, the real and imaginary part of the refractive index $m = m_\mathrm{r} + i\, m_\mathrm{i}$. An additional parameter for the asphericity of the particles is not used here, since we are only considering spherical particles.

In the models used for this work two aerosol modes are assumed. This is similar to AERONET spectral deconvolution algorithm (SDA, O'Neill et al. (2003)) and inversion products (Dubovik and King, 2000). The modes are named *fine* and *coarse* mode with respect to their effective radius. A lognormal particle size distribution (PSD) is used for each mode. The optical depth τ_{550} refers to a wavelength of 550 nm. To create the distributions from the monodisperse parametrization, they are integrated over the particle size distribution.

3. Methods and Instrument characterization

3.1. Radiative transfer models

3.1.1. LIRA-V

The iterative nature of the retrieval requires a fast forward model. Here, a modified version of the *LIRA-V* model is used, which was developed at SRON for trace gas retrievals (Landgraf et al., 2001). Originally a scalar radiative transfer solver, it was later expanded to include polarization (Hasekamp and Landgraf, 2002). *LIRA-V* solves the single scattering part of the radiance analytically. The multiple-scattering contribution is calculated with a doubling-adding approach (de Haan et al., 1987), using the Gauß-Seidel iteration scheme for solving the coupling between layers. It utilizes the aerosol optical properties from the dataset described in Dubovik et al. (2006).

3.1.2. MYSTIC

The synthetic observations for this study have been generated with the *Monte Carlo code for the physically correct tracing of photons in cloudy atmospheres (MYSTIC)* (Mayer, 2009), which is part of the *libRadtran* radiative transfer software package (Emde et al., 2016; Mayer and Kylling, 2005). *MYSTIC* is capable of calculating fully polarized radiances for three dimensional aerosol and cloud scenes using the Monte-Carlo method to solve the radiative transfer equation (Buras and Mayer, 2011; Emde et al., 2010). It has been validated in the IPRT intercomparison project (Emde et al., 2015, 2018). *libRadtran* also provides tools for creating aerosol and cloud optical properties using Mie theory (Mie, 1908; Wiscombe, 1980).

3.2. Aerosol retrieval

3.2.1. Retrieval method

The forward models described in the previous section solve the vector radiative transfer equation for a given atmospheric state $\mathbf{x}$, as expressed in Eq. (3.1). The resulting measurement vector $\mathbf{y}_{\mathrm{mod}}$ contains the Stokes vectors at the different viewing directions. A retrieval tries to solve the inverse problem of determining the atmospheric state associated with a given measurement vector. In general, this is analytically not possible and ill-posed, meaning the result might be ambiguous. Therefore minimization techniques have to be used, as shown in Eq. (3.2). This implies finding the solution state vector $\mathbf{x}^\star$ minimizing the loss function $S\left(\mathbf{r}\right)$ for the residual $\mathbf{r} = \mathbf{y} - F\left(\mathbf{x}\right)$.

$$\mathbf{y}_{\mathrm{mod}} = F\left(\mathbf{x}\right) \tag{3.1}$$
$$\mathbf{x}^\star = \arg\min_{\mathbf{x}}\left[S\left(\mathbf{r}\right)\right] = \arg\min_{\mathbf{x}}\left[S\left(\mathbf{y}_{\mathrm{meas}} - F\left(\mathbf{x}\right)\right)\right] \tag{3.2}$$

$\arg\min_{a}\left[G\left(a\right)\right]$ is a function describing the parameter a that minimizes the value of $G\left(x\right)$.

These types of minimizations are usually performed by iterative methods, such as Newton Conjugate-Gradient (CG) solvers. For this work, a truncated Newton CG algorithm described in (Nash, 1984) has been used, which has the ability to specify bounds for the components of the solution state. This is advantageous as it allows us to restrict for example the aerosol parameters to the tabulated values or a subrange thereof. As all CG methods, it requires the Jacobian of the forward model. Furthermore, for iterative solvers an initial guess for the state vector is needed.

The Stokes vector is calculated for several sun and viewing angles, and wavelengths. The measurement vector can then be defined in a variety of ways. My retrieval can use the total radiance, the linear polarized radiance and the degree of linear polarization for each wavelength and viewing angle in the measurement vector. Also, a combination is possible.

However, the magnitude of these types of measurements might differ by a large factor. For example, the total radiance, on average, is a factor of 10 to 150 larger than the linear polarized radiance (compare Fig. 4.2 and Fig. 4.4). This has to be taken into account for calculating the loss function in Eq. (3.2). Therefore, we use a weighted 2-norm:

$$S\left(\mathbf{r}\right) = \sqrt{\mathbf{r}^{\mathrm{T}}\widehat{\mathbf{M}}\mathbf{r}}$$

$$= \sqrt{\left(\begin{array}{c}\Delta\mathbf{I}\\\Delta\mathbf{I}_{\mathrm{LP}}\end{array}\right)^{T}\widehat{\mathbf{M}}\left(\begin{array}{c}\Delta\mathbf{I}\\\Delta\mathbf{I}_{\mathrm{LP}}\end{array}\right)}$$

$$= \sqrt{\left(\begin{array}{c}\Delta\mathbf{I}\\\Delta\mathbf{I}_{\mathrm{LP}}\end{array}\right)^{T}\left(\begin{array}{cc}\mathbb{1} & 0\\0 & \widehat{\mathbf{Q}}\end{array}\right)\left(\begin{array}{c}\Delta\mathbf{I}\\\Delta\mathbf{I}_{\mathrm{LP}}\end{array}\right)},$$

$$\text{with} \qquad \widehat{\mathbf{Q}} = \mathrm{diag}\left(q\right), q = \frac{\overline{I}}{\overline{I_{\mathrm{LP}}}}.$$

ΔI and ΔI_{LP} are the residuals for the total and linear polarized intensity, respectively. The quotient q gives the polarized intensity measurements a higher weight. It is proportional to the ratio of the means of the total intensity $(\overline{I})$ and the linear polarized intensity $(\overline{I_{\mathrm{LP}}})$.

My retrieval is designed in such a way that arbitrary scan patterns for any sun position can be used, as well as multispectral measurements. The *scipy* Python library includes the aforementioned truncated Newton CG solver under the name *TNC*. Also, it has facilities to numerically calculate the necessary Jacobian using two–point finite difference estimation. The LIRA-V forward model also has the possibility to calculate the Jacobian using finite differences. However, this this was left to the minimizer as it can be more "clever about it" and does not always need calculate the full Jacobian, providing a speedup. For the initial guess and the parameter bounds, the values in Table 3.1 have been used. For a detailed explanation of the parameters, see Section 2.3. They represent realistic values in the parameter bounds. These cover the range of realistic values for all aerosol parameters.

In this study, the measurement vector $\mathbf{y}$ is comprised of the total and the polarized radiance for each wavelength and viewing angle.

3.2.2. Cloud screening

The cloud screening is based on a density based outlier detection algorithm called *Local Outlier Factor* (LOF) (Breunig et al., 2000). It is implemented as part of the *scikit-learn* Python library. This algorithm is trained with simulated measurements generated with a forward model. Each measurement can have features in several dimensions. In the resulting metric space, the distance between the datapoints can be calculated. Then the distance is calculated for the real world measurements that are to be evaluated. If it exceeds the average distance of its k nearest neighbours by a certain threshold, it is considered to be an outlier.

Table 3.1.: Boundaries and initial values for the aerosol parameters used for the retrieval in the synthetic studies. For effective variance (v_{eff}), imaginary part of the refractive index (m_{i}), and fraction of spherical particles (f_{sph}) no bouds are given, as these quantities are fixed.

parameter	fine mode			coarse mode		
	min	max	init	min	max	init
r_{eff} [µm]	0.01	0.5	0.1	0.5	3.0	1.0
v_{eff} [-]	–	–	0.62	–	–	0.62
m_{r} [-]	1.3	1.7	1.5	1.3	1.7	1.5
m_{i} [-]	–	–	0.01	–	–	0.01
τ_{550} [-]	0.01	1.0	0.2	0.01	1.0	0.05
f_{sph} [-]	–	–	1.0	–	–	0.1

The features selected for the cloud screening are the total and polarized radiance at all wavelengths and viewing angles, as well as the derivatives with respect to the viewing angle. Using only the derivatives makes the method susceptible to noisy data, leading to a too strict screening. The absolute values however only pick up extreme outliers, missing clouds with small modifications in the radiance field. A combination of the two yields more sensible and stable results.

To generate the training data for the algorithm, a set of 200 simulations are run for random states in the acceptance region of the retrieval (see Table 3.1). This is done using the *LIRA-V* forward model. Since the algorithm is based on a random process the results can vary slightly from run to run. To get correct retrieval results the cloud screening should rather remove too many measurements than too few. Worst case, the retrieval will converge slowly or not at all, but not towards wrong values.

3.2.3. Modified aerosol retrieval algorithm

To better adapt the retrieval algorithm to real measurements, several changes have been made. These modifications are employed for all results shown in Section 4.2. Those in Section 4.1 use the method outlined above.

Firstly, the cloud-screening has been be revised. Due to the higher level of noise in the measurements, the original method classified too many measurements as cloudy. Furthermore, SSARA also provides unpolarized radiance measurements at 440 nm and 780 nm usable for cloud detection. In the new version, a set of 500 simulations of the given scan geometry is performed with aerosol parameters randomly sampled from the ranges given in Table 4.1. For simplicity and computational speed, only

a single aerosol mode is used in these forward simulations. For every wavelength, the measured total radiance and its derivative with respect to the scattering angle are compared to these simulations. If the measured quantities are not within the 95th percentile of the simulated values, the measurement at this angle is flagged as cloudy. The same is done for the DoLP at 500 nm. This gives four separate cloud masks, three from unpolarized radiances at 440 nm, 500 nm and 780 nm, and one from the DoLP at 500 nm. If more than two of them indicate a cloud at a certain scan angle, this datapoint is removed from the scan for the subsequent retrieval. This multi-stage approach makes the method robust against noise, but still strict enough to reliably remove observations of clouds.

Additionally, the measurement scans performed with SSARA during the A-LIFE campaign are not taken at equidistant scattering angles, as was done in the synthetic studies Similar to scans performed by instrument in the AERONET framework, the measurements are denser around the sun. This results in this area being overrepresented and therefore overweighted in the minimization procedure. However, much of the additional information provided by polarization is contained in measurements at larger scattering angles. To account for this, all measurements are weighted by the inverse of their angular density

$$w_\mathrm{i} = \frac{1}{2} \left(\vartheta_\mathrm{i+1} - \vartheta_\mathrm{i-1} \right) , \tag{3.3}$$

where w_i is the weight of the ith measurement point, and ϑ_i the corresponding scattering angle.

Lastly, a mixture of spherical and non-spherical particles is assumed for the coarse mode. This is more realistic for many aerosols (e. g. Dubovik et al., 2006, and references therein). The optical properties of this mixture is calculated by linear mixing of the tabulated optical properties for spheres and spheroids from Dubovik et al. (2006). They describe spheroids as a mixture of particles with aspect ratios ranging from 0.3 (elongated) to 3.0 (flattened). The fine mode is still assumed to contain only spherical particles. Table 4.1 shows the changed initial values and retrieval limits for all aerosol parameters for the retrieval of the SSARA measurements. A ground albedo of 0.15 has been estimated from MODIS observations and is used for all wavelengths.

3.3. The polarized sun and sky radiometer SSARA

3.3.1. Design overview

SSARA is a polarized multispectral sun photometer that has been designed and built at the Meteorological Institute Munich. The instrument consists of three main

Table 3.2.: Boundaries and initial values for the aerosol parameters used for the retrieval in the A-LIFE data. For effective variance (v_{eff}), imaginary part of the refractive index (m_{i}), and fraction of spherical particles (f_{sph}) no bouds are given, as these quantities are fixed.

parameter	fine mode			coarse mode		
	min	max	init	min	max	init
r_{eff} [µm]	0.05	0.50	0.10	0.50	3.00	1.00
v_{eff} [-]	–	–	0.62	–	–	0.62
m_{r} [-]	1.35	1.65	1.50	1.35	1.65	1.50
m_{i} [-]	–	–	0.01	–	–	0.01
τ_{550} [-]	0.01	1.00	0.10	0.01	1.00	0.05
f_{sph} [-]	–	–	1.00	–	–	0.10

components. These are the sensorhead, an alt–azimuthal mount, and a controller box containing a Programmable Logic Controller (PLC). The latter is responsible for actuating the mount, operating the sensorhead with all its life support, and digitizing the sensorhead's signals. It is connected to and controlled by a computer via a serial connection.

The radiometer's sensorhead (Fig. 3.1) houses baffles for 15 optical channels with a nominal field of view (FOV) of 1.2°. All these channels can measure simultaneously. The selection of wavelengths for the channels is done by bandpass interference filters in front of the baffles. Their characteristics are given in Table 3.3. All channels are installed parallel to each other and are installed inside a watertight casing with with a quartz glass window in front. The pointing of the channels is parallel to within 20 arcmin.

For channels 1–12, measurements of the direct sun radiance are possible. Their filters are chosen to have similar characteristics to those used in AERONET instruments. In addition to the bandpass interference filters, channels 13–15 are equipped with linear polarizers. These are oriented at roughly 0°, −45° and 90° relative to the sensorhead's horizontal axis. Channels 3, 7, and 11, as well as the polarized channels, have a second amplifier stage installed. This allows for measurements of the sky radiance, which is several orders of magnitude smaller than the direct sun radiances. These measurements are performed in the solar principal and the almucantar plane. Another difference between the channels is their optics. While channels 1–12 use a simple pinhole design, the latter use plano–convex lenses. This was done to increase the sensitivity of the instrument, as the radiance of a larger area is concentrated on the detector, requiring smaller amplification. Furthermore, the sensorhead includes a four-quadrant sensor for

Figure 3.1.: SSARA sensorhead with 12 direct channels (smaller diameter tubes), and 3 polarized channels (larger diameter at the top, left and right). The quadrant sun-tracker is in the center, below it is a finder for manual sun tracking.

tracking the sun.

In order to apply proper corrections to the Rayleigh scattering background, the air pressure is measured by a *Young 61204V* barometric pressure sensor and also inputs a voltage signal. The sensorhead is continuously heated to 40 °C to minimize drifts in detector and filter characteristics. A rain sensor is used to bow the sensorhead during precipitation to avoid staining of the front window. A electronically controlled shutter can be used to shade all detectors from incoming radiation. This feature was included to perform dark-current measurements.

The instrument can perform measurements at a maximum time resolution of about 1.6 s, which is used for the direct measurements. Due to the design of the electronics, the amplifiers of the polarized channels have a higher time constant of 1 s (compared to 0.25 s in the direct channels). This was done intentionally to have an analog filter for smoothing the signal. For scans, we therefore wait 6 s to allow for the detector signal to settle, preventing the measurements at different scanning angles from "blurring" into one another.

The scan patterns and wavelengths of SSARA are similar to those of the Cimel instruments used in AERONET, allowing for comparison. However, in contrast to Cimel, it is able to measure all its channels simultaneously, because it does not use a filter wheel. Also, since it is not part of an operational network, it can be operated in any mode deemed appropriate. For instance, sky radiance scans can

Table 3.3.: SSARA channel configuration from 23 January 2017 onward. λ_{ctr} is the central wavelength of the filter, $\Delta\lambda$ is its full-width at half maximum. *gain* gives the amplification of the second amplifier stage, if installed for the corresponding channel.

Nr.	λ_{ctr}[nm]	$\Delta\lambda$[nm]	gain	remarks
1	340.2	1.9		
2	378.7	1.9		
3	440.2	10.1	210.97	
4	499.8	9.8		
5	614.8	3.6		
6	675.7	9.8		
7	780.8	5.8	210.49	
8	869.6	9.7		
9	909.7	9.8		for water vapor absorption
10	936.6	9.7		for water vapor absorption
11	1020.4	9.7	1004.80	defective
12	1639.7	25.3		InGaAs detector
13	501.5	7.9	2.00	polarized, 0°
14	501.5	7.9	2.01	polarized, −45°
15	501.5	7.9	2.00	polarized, 90°

be performed at a higher rate, or even using new patterns for testing.

3.3.2. Readout electronics

Every channel has its own detector with readout electronics. With the exception of channel 12, silicon PIN-photodiodes (*Judson UV-040BQ*) are used as detectors. These are however only usable up to ∼1100 nm, so for the infrared channel 12 an InGaAs photodiode (*Hamamutsu G5832-01*) is used. The first stage of the readout circuitry is outlined in Fig. 3.2. It consists of a transimpedance amplifier converting the photo-electric current of the photodiode to a voltage signal. The photodiode is installed in photo–conductive mode, giving it linear response to incoming radiation. For a given incoming spectral radiance I_λ^{in}, the voltage signal $U_{\text{S1,k}}$ of channel k can be calculated by

$$U_{\text{S1,k}}(\lambda) = G_{\text{k}} \cdot R_{\text{k}}(\lambda) \cdot T_{\text{k}}(\lambda) \cdot I_\lambda^{\text{in}}. \tag{3.4}$$

The channels filters transmissivity T_{k} and the responsivity of the photodiode R_{k} can be found in their respective datasheets. Obviously the filter transmittance, but also the sensors reponsivity have a strong wavelength dependence. However, if the filters characteristic is narrow enough, the equation can be treated as monochromatic. Their value is different for every channel k. So is the transimpedance G_{k} of the amplifier, which is set by the resistors R_1, R_2, and R_3 as

$$G = \frac{U_{\text{S1}}}{I_{\text{photo}}} = R_1 \cdot \left(1 + \frac{R_2}{R_3}\right). \tag{3.5}$$

The values for these components are chosen so that the maximum expected values of solar radiance does not saturate the amplifier and analog–digital converter (ADC) in the PLC. The time constant mentioned above is mainly influenced by the capacitance C_1.

Some channels have an additional second amplifier stage (Fig. 3.3) to allow for the measurement of diffuse sky radiance. The second stage uses the operational amplifier in non–inverting amplifier configuration. Here, the gain G_2 is defined by the resistors R_4 and R_5.

$$U_{\text{S2}} = G_2 \cdot U_{\text{S1}} = \left(1 + \frac{R_4}{R_5}\right) \cdot U_{\text{S1}} \tag{3.6}$$

The amplifier used in both stages is a *Linear Technology LT1057* dual JFET input operational amplifier. An offset voltage of ≈200 mV is added to all signals by an instrument amplifier inside the sensorhead. This is done to avoid operating the ADC near 0 V and account for channels with negative signal voltages discussed later. The signals of the detectors are then multiplexed on a single wire, leading from the
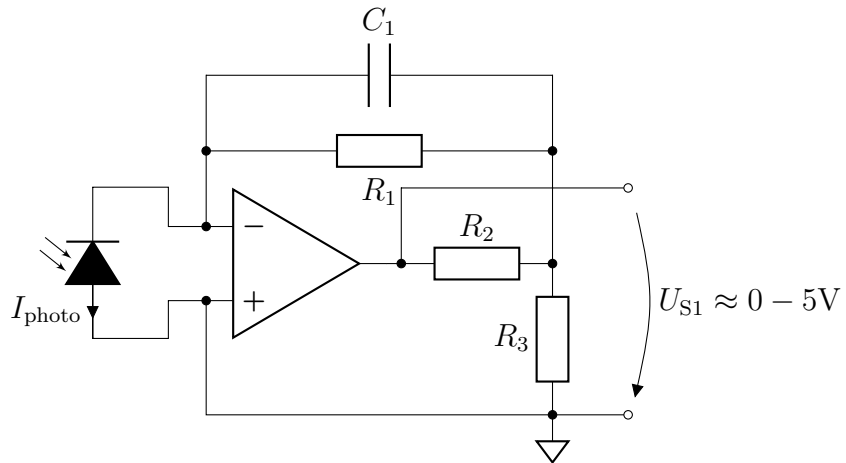
Figure 3.2.: SSARA sensorhead detector and readout electronics with first amplifier stage.
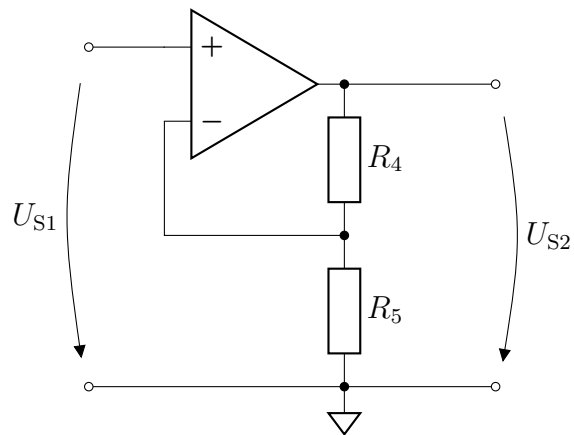
Figure 3.3.: SSARA sensorhead second stage amplifier

sensorhead to the PLC. The analog voltage signal U_S is digitalized in the *Jetter JX2-IA4* analog-to-digital converter (ADC) unit extending the *Jetter NANO-B* PLC. It mainly contains a *Analog Devices MAX197* ADC with a resolution of 12 bit. The voltage is digitized in a single ended configuration from 0 V to 10 V. In addition to the detector signals, 5 V produced by a *Analog Devices REF02* reference voltage source and the signal ground are passed to the ADC. This allows for the correction of common-mode interference and detection of higher frequency noise on the data line. In total 35 signal voltages are measured at a time, distributed over several multiplexers and ADC channels. Table 3.4 gives an overview over all these signals. Apart from the detector signals including the quadrant sun tracker (4Q), the reference voltages and the pressure sensor signal, the voltage at several thermistors is measured. With this, the temperature near the photodetectors, filters, elevation motor, and power supply can be determined.

We use the ADC readout for the 5 V ($S_{5\,V}$) and signal ground ($S_{0\,V}$) and the dark signal (S_{dark}) to reconstruct the signal voltage U_S from its ADC readout S,

$$U_S = \frac{S_{5\,V} - S_{0\,V}}{5\,V} \cdot (S - S_{dark}) \,. \tag{3.7}$$

Here, S_{dark} is the signal measured with no radiation reaching the sensor. This measurement is done by either covering the sensorhead window or closing SSARA's internal shutter. For most channels (all but those including a second amplifier stage), the dark current and the ground signal are equal to within the resolution of the ADC ($S_{dark} \simeq S_{0\,V}$). The others (channels 3, 7, 11 and 13 through 15) might have signal voltages below signal ground ($S_{dark} < S_{0\,V}$). This subtraction removes the offset voltage added earlier. For compatibility with older software expecting ADC counts instead of voltages, this signal voltage U_S can be converted to a virtual ADC readout $S^\star$ by

$$S^\star = \frac{2^{12}}{10\,V} \cdot U_S \,. \tag{3.8}$$

Reconstructing the measured air pressure from the recorded voltage U_S is simpler. According to the datasheet, the air pressure range of 660 hPa to 1100 hPa is linearly mapped to 0 V to 5 V, so

$$p = \frac{500\,hPa}{5\,V} U_S + 600\,hPa \tag{3.9}$$

3.3.3. Alt–azimuthal Mount

The sensorhead is mounted on a two-axis alt–azimuthal mount (Seefeldner et al., 2004). Its stepper motors are operated by two *JX2-SM1D* motor drivers, also

Chan. no.	SSARA channel	ADC channel	Mux no.	Mux channel	description
0	1	0	0	0	340 nm direct
1	2	0	0	1	380 nm direct
2	3	0	0	2	440 nm direct
3	4	0	0	3	500 nm direct
4	5	0	0	4	615 nm direct
5	6	0	0	5	675 nm direct
6	7	0	0	6	780 nm direct
7	8	0	0	7	870 nm direct
8	9	0	0	8	910 nm direct
9	10	0	0	9	950 nm direct
10	11	0	0	10	1030 nm direct
11	12	0	0	11	1550 nm direct
12	–	0	0	12	5 V reference Mux 0
13	–	0	0	13	thermistor U_0
14	–	0	0	14	thermistor detector
15	–	0	0	15	0 V reference Mux 0
16	13	0	1	0	500 nm 0° pol
17	14	0	1	1	500 nm 45° pol
18	15	0	1	2	500 nm 90° pol
19	3	0	1	3	440 nm sky x200
20	7	0	1	4	780 nm sky x200
21	11	0	1	5	1030 nm sky x1000
22	13	0	1	6	500 nm 0° pol x2
23	14	0	1	7	500 nm 45° pol x2
24	15	0	1	8	500 nm 90° pol x2
25	–	0	1	9	4Q right upper
26	–	0	1	10	4Q left upper
27	–	0	1	11	4Q right lower
28	–	0	1	12	5 V ref Mux 1
29	–	0	1	13	0 V ref Mux 1
30	–	0	1	14	4Q left lower
31	–	0	1	15	thermistor filter
32	–	1	–	–	thermistor power supply
33	–	2	–	–	pressure sensor
34	–	3	–	–	thermistor elevation motor

Table 3.4.: SSARA channel breakdown. The channels are selected by the ADC channel, and multiplexer (mux) number and channel. SSARA channel is the physical channel as described in Table 3.3.

controlled by the PLC. The *Phytron ZSS52.200.2,5* motors have a resolution of 200 steps per rotation (1.8° per step). They are extended by a *Harmonic Drive HD14* transmission with a reduction of 100:1. Since the motor drivers are able to operate the motors with half-steps, the resolution is again halved to a final value of 0.009° (32.4 arcsec).

3.3.4. Straylight baffle

Sunlight scattered from the glass window and possible dirt particles on it can create straylight, especially at larger scattering angles. To minimize this effect, a baffle has been designed and built in preparation of the A-LIFE campaign. It consists of a 24 cm long, black PVC cylinder with openings for the channels that is put in front of the glass window. The openings are chose to leave a 2 mm clearing to the FOV of their optical channel. This should inhibit direct sun light from hitting the front glass for scattering angles greater than 3.5°. The effect of the baffle can be seen in Fig. 3.4. It shows the difference of two consecutive principal plane scans with (orange) and without (blue) the baffle installed. For the radiance in the direct channels 3 ($I(440\,\mathrm{nm})$) and 7 ($I(780\,\mathrm{nm})$), the effect is hardly noticeable. Due to their internal construction, they already seem to be protected against stray light. The wider, polarized channels 13–15 however show deviations. The radiance without the baffle is higher across the entire scan, as would be expected from stray light. The reconstructed DoLP has a more complex behaviour. The stray light leads to an underestimation up to scattering angles of about 20°. For larger scattering angles, it is then underestimated. However, close to the sun, the DoLP should be zero, as direct radiation is almost completely unpolarized, so some errors seem to remain.

3.3.5. Software

For this work, the software for the SSARA instrument was completely redesigned in *Python*. It is designed to be network transparent, meaning that different components can run on different machines on the network. This is achieved using *pyro4* for using remote objects and *ZeroMQ* for transfer of data.

The lowest operates on the instrument itself. This serial communication itself is split into two sublayers. `JetterSerial` handles the low–level serial communication with the Jetter PLC over RS232. It includes character escaping and verifying transmission integrity using checksums. The connection has a rate of 9600 baud, with 8 bit per frame, stop bit and even parity (often abbreviated to 8E1). Building on top of that, `JetterControl` provides functionality for reading and writing the registers and flags, and starting and stopping the programs. The meaning and format of these registers, as well as the serial protocol, is described in its manual.
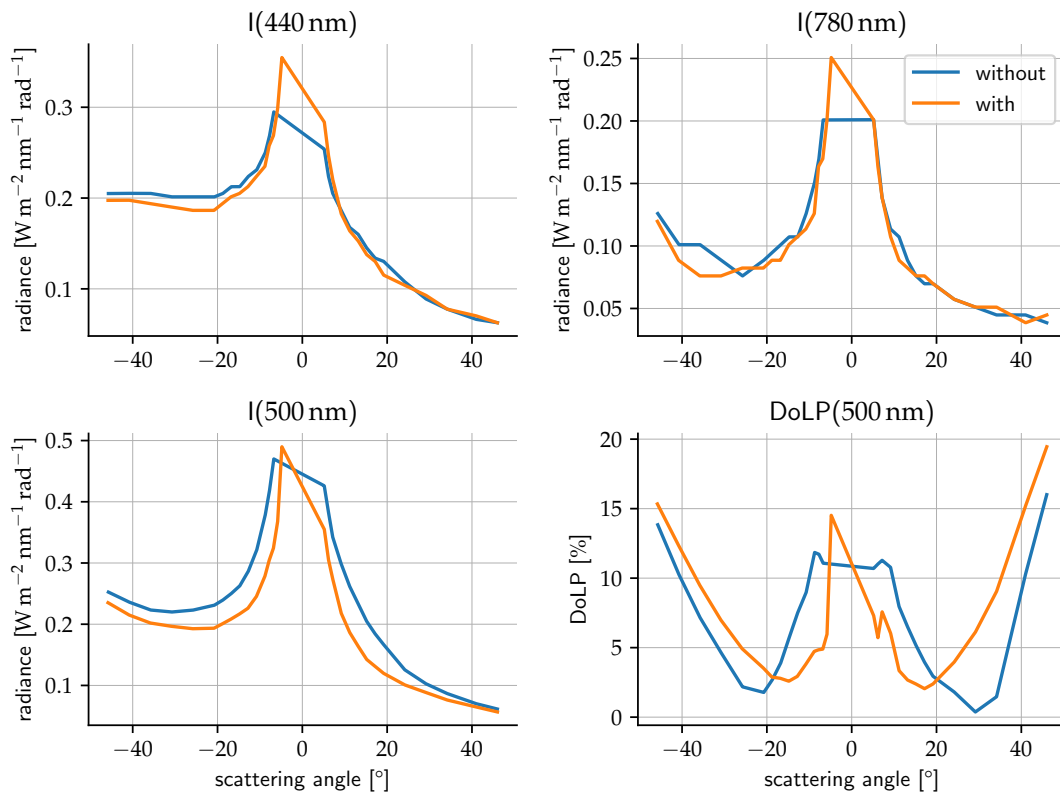
Figure 3.4.: Effect of straylight baffle on principal plane

The second layer consists of controllers for SSARA functionality, using the `JetterControl`. For instance `MotorController` has functions to read the motor current step position, and set a new target position. The `MountController` consists of two `MotorControllers` and contains information for the transformation of a viewing direction to motor step positions.

The `MeasurementController` continuously runs the readout program and sends the data over the network via *ZeroMQ*, together with timestamps for the start and end time of the acquisition. The PLC has a program stored that simplifies the process of selecting and digitizing all the signals shown in Table 3.4. This is triggered by setting flag 4. Once it is cleared again, the 35 measurement values can be read from registers 201–236. However, for this program to work, the motors have to be connected as well, which is an annoyance during laboratory calibration. To get around this, a `SensorheadController` was added to manually set and latch the address in the multiplexer via the PLC's digital outputs (lower 5 bit of register 2450). Due to the additional overhead required in the serial communication, the acquisition rate is lower, so this should not be used for normal operation.

The `TrackingController` plugs into the `MountController` and updates its position according to the tracking information from the quadrant sensor. Lastly, the `HeatingController` controls the instrument heating by receiving the thermistor measurements from the `MeasurementController` and updating the heating of the instrument using the PLC's digital to analog converter (DAC). This is implemented as a PID regulator finely tuned to quickly achieve a stable instrument temperature of $40\,°C$, without causing temperature spikes.

On the highest level, the controllers are used to create complex scanning routines. The software documentation contains an example for simple direct sun measurements under `servers/direct.py`. Additionally, the *CPM* scheduler was designed to routinely run different scans at certain times or sun zenith angles. Each task is assigned a priority with higher priority tasks preempting lower ranked ones. However, smaller numbers correspond to higher priority. A collection of programs can be found in `cpm/program`.

Also, a simple configuration framework was designed to simplify the tedious process of creating the controllers from hand. The SSARA software uses a single YAML configuration file in home directory under `.macs/ssara.yaml`. For instance, the `JetterController` can be configured to use a specific serial port:

```
jetter:
  pyro:
    name: 'ssara.jetter'    # object name for network transparancy
  port: '/dev/ttyUSB0'      # serial port to use
```

Furthermore, the location of the instrument can be set. For this, a set of known locations exist for roof of the institute (`MIM`) and the Schneefernerhaus on Mount

Zugspitze (`UFS`). Alternatively, the location can be set in decimal degrees longitude and latitude with north and east positive, and the elevation in metres. This setting is required for the calculation of the solar position.

```
location:
  # built-in locations: MIM, UFS
  # if name is set (lat, lon and lat) are ignored
  name: 'MIM'
  #lat: 34.67438
  #lon: 33.0404712
  #el: 15
```

Also the programs to be executed can be configured. Here, the instrument performs almucantar scans at certain SZAs given in `at_sza`, principal plane scans at the times listed in `at_time` and direct sun measurements for the remaining time.

```
programs:
  - name: "almuk"
    type: offset
    prio: 20
    az_offsets: [5, 10, 20, 30, 40, 50, 60, 80, 100, 120, 140, 180]
    symmetrical: az
    at_sza: [10, 15, 20, 25, 30, 35, 40, 45, 50, 60]
    trigger: angles
  - name: "pplane"
    type: offset
    prio: 25
    symmetrical: el
    el_offsets: [5, 10, 20, 30, 40, 50, 60, 80, 100, 120, 140, 180]
    at_time:
      - '09:00'
      - '10:00'
      - '11:00'
      - '12:00'
    trigger: times
  - name: "direct"
    type: direct
    target: sun
    prio: 50
```

For observing the instrument status, a simple web–GUI was implemented. It shows the status of the instrument, the readout of the sensors, the temperature,

and the mount position. Additionally, it provides the opportunity to update then configuration file.

3.4. Calibration

3.4.1. Polarimetric calibration

The polarimetric and radiometric calibration of the sky radiance channels has been performed at Laboratoire d'Optique Atmosphérique (LOA) in Lille, France. To produce linear polarized light a combination of an Ulbricht sphere and the so-called POLBOX was used (Balois, 1998). Figure 3.6 depicts the calibration setup. The POLBOX acts as a linear polarizer for the unpolarized light coming from the sphere. It consists of two glass plates that can be tilted up to 65° relative to the optical axis.
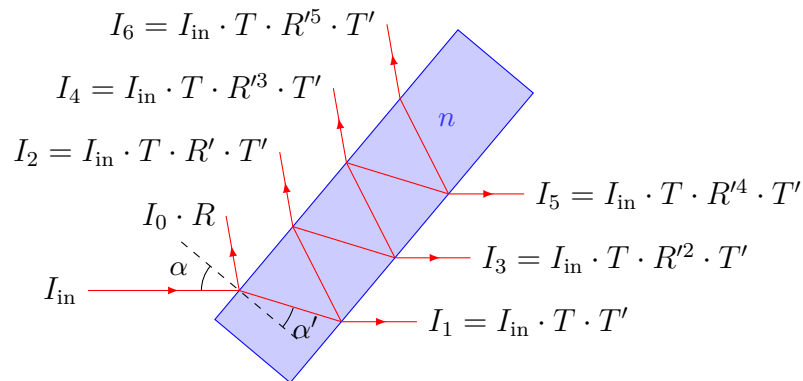
Figure 3.5.: Fresnel reflection on a single glass plate

The optical behaviour of a tilted glass plate is shown in Fig. 3.5. The incoming radiance I_in hitting the surface from the outside is either reflected (with coefficient R), or transmitted (with coefficient T). The same is true for the transmitted part hitting the inner surface, with the coefficients R' and T'. This leads to successive orders of scattering contributing to the total reflected (I_R) and transmitted intensity

(I_T). We are only interested in the latter:

$$I_\text{T} = I_1 + I_3 + I_5 + \cdots \tag{3.10}$$

$$= I_\text{in} \cdot TT' + I_\text{in} \cdot TR'^2 T' + I_\text{in} \cdot TR'^4 T' + \cdots \tag{3.11}$$

$$= I_\text{in} \cdot TT' \cdot \underbrace{\sum_{k=1}^{\infty} \left(R'^2 \right)^k}_{\text{geom. series}} \tag{3.12}$$

$$= I_\text{in} \cdot \frac{TT'}{1 - R'^2} \tag{3.13}$$

The Fresnel equations describe the coefficients for transmission and reflection on the interface of two media with refractive indices n_1 and n_2. These differ for radiation polarized in the incident plane ($I_\parallel$) and perpendicular to it ($I_\perp$)

$$R_\perp = \left(\frac{n_1 \cos\alpha - n_2 \cos\alpha'}{n_1 \cos\alpha - n_2 \cos\alpha'} \right)^2 , \quad T_\perp = \frac{n_2 \cos\alpha'}{n_1 \cos\alpha} \left(\frac{2n_1 \cos\alpha}{n_1 \cos\alpha - n_2 \cos\alpha'} \right)^2 \tag{3.14}$$

$$R_\parallel = \left(\frac{n_2 \cos\alpha - n_1 \cos\alpha'}{n_2 \cos\alpha - n_1 \cos\alpha'} \right)^2 , \quad T_\parallel = \frac{n_2 \cos\alpha'}{n_1 \cos\alpha} \left(\frac{2n_1 \cos\alpha}{n_2 \cos\alpha - n_1 \cos\alpha'} \right)^2 \tag{3.15}$$

$$R + T = R' + T' = 1 , \qquad R = -R' \quad \Rightarrow \quad TT' = (1 - R)^2 \tag{3.16}$$

Here, α is the angle between the incident light and the normal of the glass plate, α' that between the normal and the refracted light. Note that these are the equations for intensity, not electric fields. From these a series of properties (Eq. (3.16)) can be derived, which hold true regardless of the polarization state. Using those equalities, Eq. (3.13) can be further simplified:

$$I_\text{T} = I_\text{in} \cdot \frac{1 - R}{1 + R} \tag{3.17}$$

$$\Rightarrow \quad I_\perp = I_\text{in} \cdot \frac{1 - R_\perp}{1 + R_\perp} , \quad I_\parallel = I_\text{in} \cdot \frac{1 - R_\parallel}{1 + R_\parallel} \tag{3.18}$$

$$\tag{3.19}$$

$I_\perp$ and $I_\parallel$ are the intensities of the radiance transmitted through the glass plate in the respective polarization state. Therefore, the degree of linear polarization (DoLP) η of the transmitted light is dependent on to the tilting angle of the glass plate α.

$$\eta(\alpha, n) = \frac{I_\parallel - I_\perp}{I_\parallel + I_\perp} \tag{3.20}$$

$$= \frac{(1 - n^2) \left[\cos^2\alpha - \left(1 - \frac{1}{n^2} \sin^2\alpha \right) \right]}{(1 + n^2) \left[\cos^2\alpha + \left(1 - \frac{1}{n^2} \sin^2\alpha \right) \right]} \tag{3.21}$$

The refractive index of air is assumed to be 1, so the equation is only dependent on that of the glass material n. Since the angle of the plate can be determined with high accuracy, also the DoLP is known to a high precision. The entire assembly can be rotated around its optical axis, therefore changing the polarization plane of the transmitted light. When using two plates and tilting the second by the same angle α, but in the opposite direction, a divergent ray of light hitting the first plate at angle $\alpha + \delta\alpha$ will hit the second plate at an angle $\alpha - \delta\alpha$. This compensates for linear terms of error in the DoLP due to divergent light. It can be shown that the DoLP after the second plate η_{tot} is given by

$$\eta_{\text{tot}}(\alpha, n) = \frac{2\eta(\alpha)}{1 + \eta^2(\alpha)} + \mathcal{O}\left(\delta\alpha^2\right) \tag{3.22}$$

$$\approx \frac{\left(1 - n^4\right)\left(\cos^4 \alpha - \cos^4 \alpha'\right)}{\left(1 + n^4\right)\left(\cos^4 \alpha + \cos^4 \alpha'\right) + 4n^2 \cos^2 \alpha \cos^2 \alpha'} \tag{3.23}$$

α' can be calculated using Snellius law.

$$\sin \alpha = \sin \alpha' \cdot n \tag{3.24}$$

$$\Rightarrow \quad \cos \alpha' = \sqrt{1 - \frac{1}{n^2} \sin^2 \alpha} \tag{3.25}$$

The glass plates are fabricated from *Schott SF-11* type glass. Its datasheet provides coefficients for the Sellmeier equation (Eq. (3.26)), to calculate the refractive index n:

$$n(\lambda) = \sqrt{1 + \sum_i \frac{B_i \lambda^2}{\lambda^2 - C_i}}, \tag{3.26}$$

with

$B_1 = 1.73759695$, $C_1 = 0.013\,188\,707\,00\,\mu\text{m}^2$,
$B_2 = 0.313747346$, $C_2 = 0.062\,306\,814\,2\,\mu\text{m}^2$,
$B_3 = 1.898781010$, $C_3 = 155.236\,290\,0\,\mu\text{m}^2$.

The POLBOX handbook (Balois, 1998) further expands Eq. (3.23) in powers of the refractive index n, employing Snellius law to subsitute α'. This leads to the following solution for the total degree of polarization:

$$\eta_{\text{tot}}(\alpha, n) = \frac{A \cdot \cos^2(2\alpha) + B \cdot \cos(2\alpha) + C}{D \cdot \cos^2(2\alpha) + E \cdot \cos(2\alpha) + F}, \tag{3.27}$$
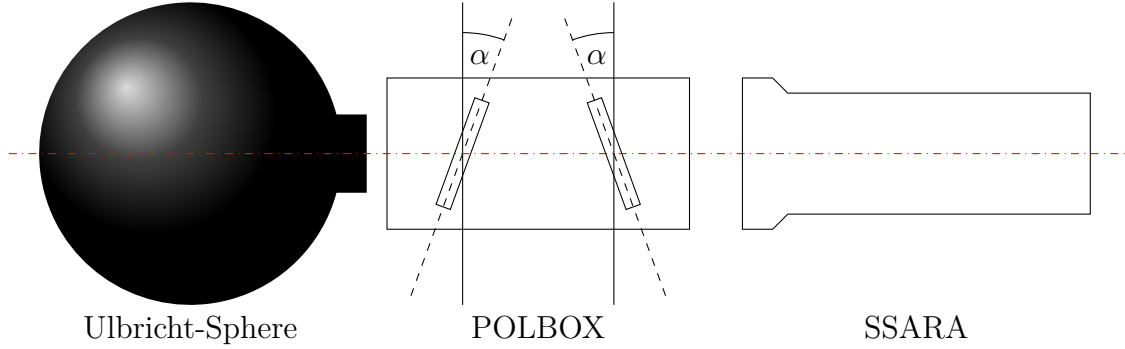
Figure 3.6.: POLBOX calibration setup

with

$$A = -n^8 + 2 \cdot n^4 - 1 \,,$$
$$B = -2 \cdot n^8 + 4 \cdot n^6 - 4 \cdot n^2 + 2 \,,$$
$$C = 3 \cdot n^8 - 4 \cdot n^6 - 2 \cdot n^4 - 4 \cdot n^2 - 1 \,,$$
$$D = -A + 8 \cdot n^4 \,,$$
$$E = -B + 16 \cdot n^6 \,,$$
$$F = -C + 8 \cdot n^8 \,.$$

The POLBOX has a maximum tilt angle of $\alpha = 65°$. The resulting DoLP is roughly $58\,\%$ at the SSARA polarized wavelength of $501.5\,\text{nm}$.

As discussed in Section 2.1.2, in the context of the *Stokes–Müller* formalism SSARA's polarization filters can be described by the Müller matrix $\widehat{\mathbf{LD}}$ of a linear diattenuator.

$$\widehat{\mathbf{LD}}\left(\vartheta\right) =$$

$$\frac{1}{2} \begin{pmatrix} a & b\cos\left(2\vartheta\right) & b\sin\left(2\vartheta\right) & 0 \\ b\cos\left(2\vartheta\right) & a\cos^2\left(2\vartheta\right) + c\sin^2\left(2\vartheta\right) & \left(a-c\right)\cos\left(2\vartheta\right)\sin\left(2\vartheta\right) & 0 \\ b\sin\left(2\vartheta\right) & \left(a-c\right)\cos\left(2\vartheta\right)\sin\left(2\vartheta\right) & a\sin^2\left(2\vartheta\right) + c\cos^2\left(2\vartheta\right) & 0 \\ 0 & 0 & 0 & c \end{pmatrix}, \tag{3.28}$$

with $a = k_0 + k_1$, $b = k_0 - k_1$, and $c = 2\sqrt{k_0 k_1}$. k_0 and k_1 are the transmission values for the filter in the direction parallel and perpendicular to its orientation, respectively. ϑ is the angle between the polarization direction of the incoming radiation and the filter. Since a photodiode can only measure the total intensity of the light (first component of Stokes vector), the measurement operator $\langle M|$ projects only the first row of the matrix. Mathematically, it can be described as a

transposed vector $(1, 0, 0, 0)$

$$I = \langle M | \widehat{\mathbf{LD}} | \mathbf{S} \rangle \tag{3.29}$$

$$= \frac{1}{2} \left[a \cdot I_0 + b \cdot \cos\left(2 \cdot \Delta\vartheta\right) \cdot Q_0 + b \cdot \sin\left(2 \cdot \Delta\vartheta\right) \cdot U_0 \right] \tag{3.30}$$

The light entering the instrument behind the POLBOX is taken to be polarized only in the positive Q direction. This means the Stokes vector is given by $(I_0, \eta_{\mathrm{tot}} I_0, 0, 0)^{\mathrm{T}}$, with η_{tot} again being the degree of linear polarization produced by the POLBOX. Also, the sensor has a certain radiometric response C, so the measurement vector becomes $\langle M | = (C, 0, 0, 0)$.

$$S\left(\vartheta\right) = \frac{C}{2} \left[a \cdot I_0 + b \cdot \cos\left(2\left(\vartheta - \vartheta_0\right)\right) \eta \cdot I_0 \right] \tag{3.31}$$

$$= \frac{1}{2} \left[a' \cdot I_0 + b' \cdot \cos\left(2\left(\vartheta - \vartheta_0\right)\right) \cdot \eta \cdot I_0 \right] \tag{3.32}$$

$$= \frac{1}{2} \left[A' + \eta \cdot B' \cdot \cos\left(2\left(\vartheta - \vartheta_0\right)\right) \right] \tag{3.33}$$

It can be seen that the polarimetric (described by a and b) and radiometric response (C) of the instrument/filter combination cannot be determined separately. Therefore, we introduce $a' = C \cdot a$ and $b' = C \cdot b$. Also, since the total intensity of the incoming light is unknown, so we define $A' = a' \cdot I_0$ and $B' = b' \cdot I_0$. Measuring the signal S at varying rotation angles ϑ of the POLBOX, the parameters A', B' and ϑ_0 can be obtained by performing a Levenberg–Marquardt (LM) fit using Eq. (3.33) as a model. k_0 and k_1 cannot be determined independently, but it is possible to derive the diattenuation D as

$$D = \frac{k_0 - k_1}{k_0 + k_1} = \frac{b}{a} = \frac{b'}{a'} = \frac{B'}{A'} \, . \tag{3.34}$$

It is independent of the intensity of the incoming radiation I_0. The LM-fit also gives estimations for the uncertainties in A', B', and ϑ_0. For determining the response a', we use LOA's *SphereX*, a radiometrically calibrated Ulbricht sphere. As it provides unpolarized light with known intensity, the measured signal is given by

$$S = \frac{C}{2} a \cdot I_0 = \frac{a'}{2} I_0 \tag{3.35}$$

$$\Rightarrow \quad a' = \frac{2 \cdot S}{I_0} \, . \tag{3.36}$$

For the SSARA calibration on 2 February 2017, the fit of Eq. (3.33) to the measurements can be seen in Fig. 3.7. The determined values and their uncertainties
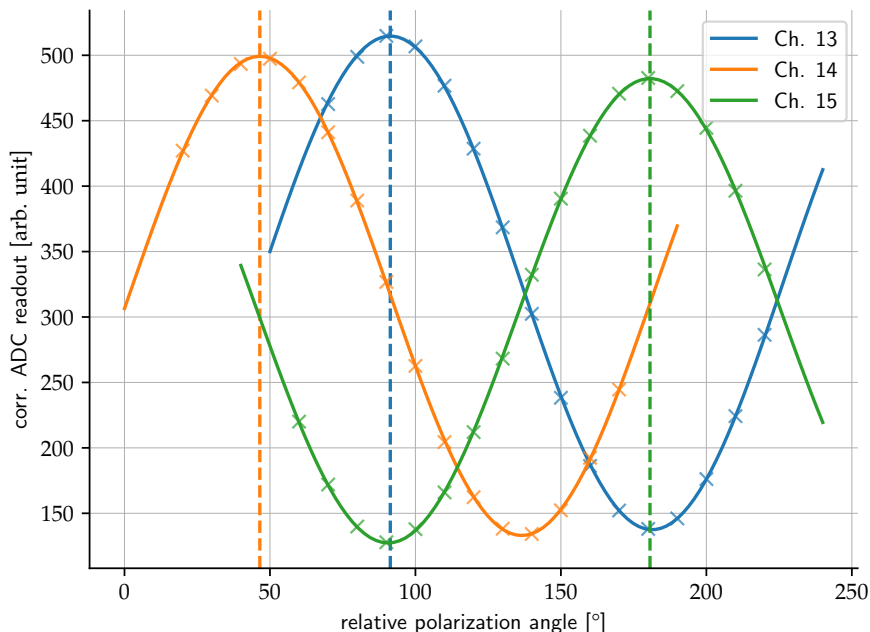
Figure 3.7.: Fit of Eq. (3.33) to intensity measurements of the three polarized SSARA channels at varying POLBOX orientations. The dashed horizontal lines correspond to the angles of maximum transmission ϑ_0. Amplitude and vertical offset are related to the radiometric and polarimetric response.

are shown in Table 3.5. It should be noted that the sensorhead was placed on its right side, therefore adding roughly 90° to the filter orientation.

What remains after this calibration is the collective rotation of all channels in the sensorhead, which also includes rotations stemming from the mount. When only the degree of linear polarization is of interest, this is not relevant. However, this global rotation has to be known to determine the polarization angle, which influences how the polarized radiation is devided between the Q and U component. As outlined in Li et al. (2014), this could be done by using known features of the Rayleigh background (e.g. $U = 0$ in principal plane).

To determine the potential error arising from neglecting the imperfections of the filters and their orientation, a polarized radiance all-sky panorama has been simulated for 500 nm using *MYSTIC* (see Section 3.1.2). To get the maximum error corresponding to the highest possible degree of linear polarization, a pure Rayleigh atmosphere was used as model input, without aerosol or clouds. Scattering processes by these would "destroy" polarization. The ground is non-reflective for the same reason and the sun at a zenith angle of 30°. The simulation is used to generate synthetic measurements in the three polarized SSARA channels, taking

Table 3.5.: Calibration results for measurements on 2 February 2017. The uncertainties are determined from the fit. Channels 3, 7, and 11, are unpolarized, so, per definition, $k_0 = k_1 = 1$, and therefore $D = 0$.

Channel	ϑ_0 [°]	D [-]	a' [1/mW m^{-2}]
3	-	0	412
7	-	0	331
11	-	0	362
13	91.36 ± 0.06	0.984 ± 0.002	8164
14	46.51 ± 0.05	0.985 ± 0.002	7979
15	180.62 ± 0.07	0.990 ± 0.002	7717

into account the filter characteristics from Table 3.5. From these, the Stokes vector is reconstructed, once assuming perfect polarizers ($D = 1$) at exact angles (90°, 45°, and 180°), and again with the actual filter characteristics in Table 3.5. Their relative difference in the total radiance and the degree of linear polarization is displayed in Figs. 3.8 and 3.9, respectively. The relative error in total radiance varies by between -1.1% and $+0.8\%$, the relative error in DoLP from -2.4% and $+1.5\%$ (relative, not in absolute value). Due to the relative rotation of the polarizers, the pattern is not symmetrical.

3.4.2. Mount calibration

SSARA should be set up perfectly perpendicular to the local tangential plane, facing exactly south. However, often this is possible only to within a few degrees. Also, SSARA is designed to be portable, so the setup procedure has to be performed regularly. Therefore, it is useful to be able to quickly install the instrument in roughly the right orientation and determine the exact alignment by correlating the positions of the mount motors with the known sun position for times with accurate sun tracking.

To determine the actual orientation of the mount from several known sun positions, we cannot directly fit the Euler angles using conventional real 3×3 rotation matrices, as this approach suffers from what is known as *gimbal lock*. This results from singularities in spherical coordinate systems, caused by directional "flips", for instance when crossing the zenith. Conventional minimization methods are not applicable in such highly non-linear cases. However, the fit can be performed using quaternions, as rotations here are always smooth and free of singularities. The mathematical fundamentals of quaternions are given in Appendix A. To perform the mount calibration, several coordinate systems are defined that can be transformed
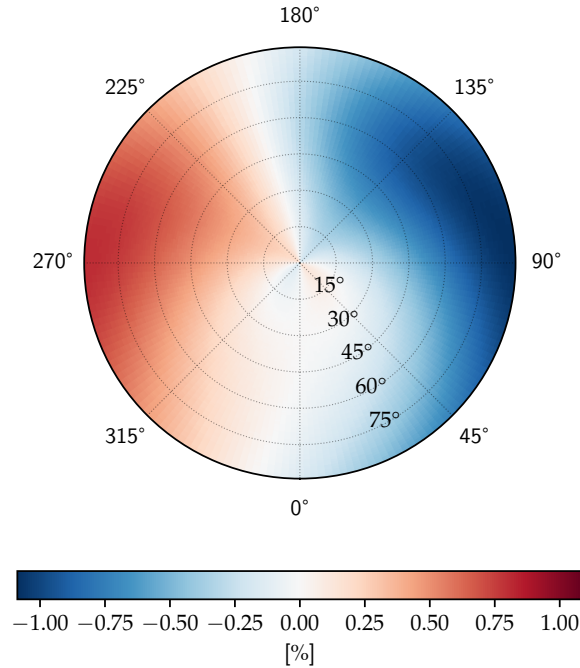
Figure 3.8.: Relative difference in measured total radiance at $500\,\mathrm{nm}$ due to incorrect rotation and imperfect polarizer for a synthetic scene. The sun is at a zenith angle of $30°$ and azimuth $0°$.

into one another by rotation. Translation is ignored, as the earth-sun-distance is much larger than the replacements in the instrument and mount. The coordinate systems used are similar to those defined in Riesing et al. (2018). Figure 3.10 sketches the coordinate systems used for SSARA:

- *East-North-Up (ENU)*: local horizon coordinate system on the tangential plane containing the observation position. Elevation and azimuth of the sun (ϑ_s, ϕ_s) can be calculated for this system. x-axis points towards east, y-axis towards north, and z-axis towards zenith.

- *Mount (MNT)*: y-axis along that of the elevation motor, x-axis is along the rotation axis of the azimuth motor, with the elevation motor centered ($\phi_0 = 0$). z-axis is the cross product of x and y-axis to form a right-handed system.

- *Gimbaled system (GMB)*: the mount system rotated around the motor axes by the elevation ϑ and azimuth ϕ. These angles consist of the zero-offset of the motor axes ($\vartheta_0\ and \phi_0$), and the rotation of the motors ($\Delta\vartheta$ and
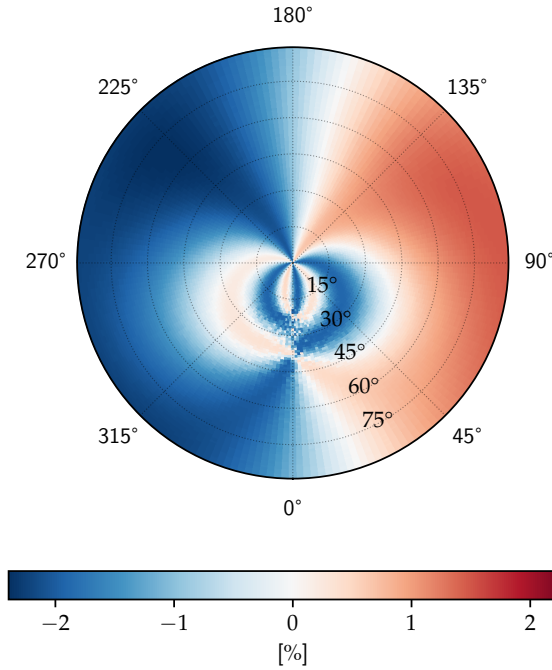
Figure 3.9.: Same as Fig. 3.8, but for the relative difference in the degree of linear polarization

$\Delta\phi$). By choice of the MNT system, ϕ_0 is defined as zero. Additionally, a non-perpendicularity between the motor axes δ is considered.

- *Sensorhead (SH)*: z-axis points along the optical axis of the sensorhead, x-axis points towards the top of the instrument, y-axis towards the right, forming a right-handed system.

In an ENU spherical coordinate system, the azimuth ϕ is zero in the north and increases towards the east, as one would expect. The polar angle is zero in the nadir and increases towards the zenith. Rotations between the coordinate systems are described by quaternions, where $^B\mathbf{q}_A$ is a quaternion rotating coordinate system A to B.

For direct measurements with the quadrant sensor uniformly lit, the sun and viewing vector in the ENU system are assumed to be equal (to within the accuracy of the suntracker). The sun position in the ENU system is determined with the *pyEphem* Python package. It can calculate planetary positions to a precision satisfactory for our purpose using the VSOP87 model (Bretagnon and Francou, 1988). To obtain the viewing vector $\mathbf{r}_v$ of the instrument, the unit vector in
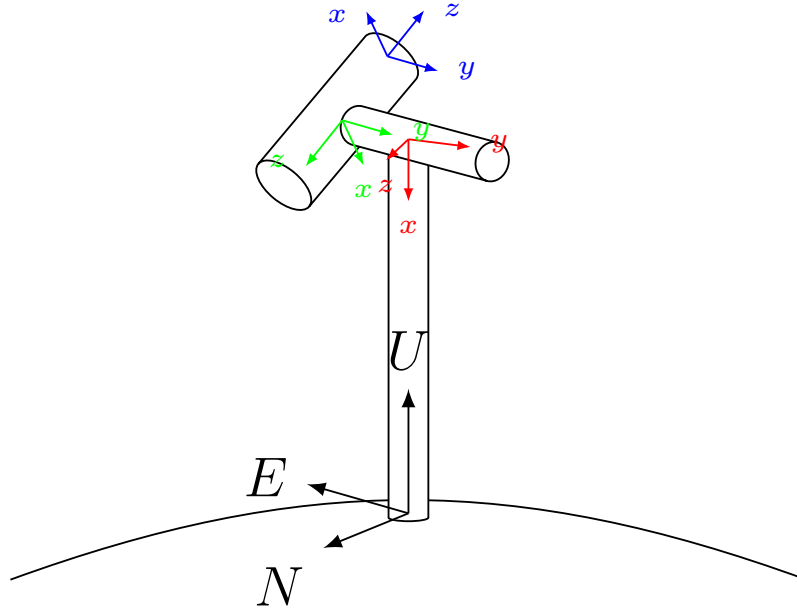
Figure 3.10.: Sketch of the SSARA instrument and the coordinate systems used for the mount calibration; ENU (black), unrotated mount system MNT (red), gimbaled mount system GMB (green), and sensorhead system SH (blue).

z-direction $\mathbf{e}_z$ in the *SH* system has to be transformed as follows

$$\mathbf{r}_v = {}^{ENU}\mathbf{q}_{SH}\mathbf{r}_{SH} = {}^{ENU}\mathbf{q}_{SH}\mathbf{e}_z \,. \tag{3.37}$$

The optimal rotation quaternion can be found by minimizing the distance between viewing vectors and sun vector $\mathbf{r}_v$,

$$S = \frac{1}{N}\sum_{i=0}^{N}\left\|\mathbf{r}_s - \mathbf{r}_v\right\| = \frac{1}{N}\sum_{i=0}^{N}\left\|\mathbf{r}_s - {}^{ENU}\mathbf{q}_{SH}\mathbf{e}_z\right\| \,. \tag{3.38}$$

However, ${}^{ENU}\mathbf{q}_{SH}$ is composed of several rotations:

$$^{ENU}\mathbf{q}_{SH} = {}^{ENU}\mathbf{q}_{MNT}{}^{MNT}\mathbf{q}_{GMB}{}^{GMB}\mathbf{q}_{SH} \tag{3.39}$$

${}^{GMB}\mathbf{q}_{SH}$ is defined as a 180° rotation around the local y-axis to obtain the sensorhead coordinate system. The active component of the mount acts on ${}^{MNT}\mathbf{q}_{GMB}$. It contains the rotation angles of the azimuth and elevation motors ($\Delta\phi$ and $\Delta\vartheta$), as well as the zero-point offset angles of the motors (ϑ_0 and ϕ_0). ϕ_0 is zero due to our definition of the MNT system (it is effectively absorbed into ${}^{ENU}\mathbf{q}_{MNT}$), but ϑ_0 has to be determined. Both offset angles are constant over time and do not change

for instrument realignment. Furthermore, the non-perpendicularity δ between the two motors is considered.

$$^{\mathrm{MNT}}\mathbf{q}_{\mathrm{GMB}} = \mathbf{q}\left(\phi, \mathbf{e}_{\mathrm{x}}\right)\left[\mathbf{q}\left(\delta, \mathbf{e}_{\mathrm{z}}\right)\mathbf{q}\left(\vartheta, \mathbf{e}_{\mathrm{y}}\right)\mathbf{q}\left(-\delta, \mathbf{e}_{\mathrm{z}}\right)\right] \tag{3.40}$$

$$= \mathbf{q}\left(\phi_0 + \Delta\phi, \mathbf{e}_{\mathrm{x}}\right)\left[\mathbf{q}\left(\delta, \mathbf{e}_{\mathrm{z}}\right)\mathbf{q}\left(\vartheta_0 + \Delta\vartheta, \mathbf{e}_{\mathrm{y}}\right)\mathbf{q}\left(-\delta, \mathbf{e}_{\mathrm{z}}\right)\right] \tag{3.41}$$

$$= \mathbf{q}\left(\Delta\phi, \mathbf{e}_{\mathrm{x}}\right)\left[\mathbf{q}\left(\delta, \mathbf{e}_{\mathrm{z}}\right)\mathbf{q}\left(\vartheta_0, \mathbf{e}_{\mathrm{y}}\right)\mathbf{q}\left(\Delta\vartheta, \mathbf{e}_{\mathrm{y}}\right)\mathbf{q}\left(-\delta, \mathbf{e}_{\mathrm{z}}\right)\right] \tag{3.42}$$

$^{\mathrm{ENU}}\mathbf{q}_{\mathrm{MNT}}$ is unknown and contains the tilt and rotation of the mount. It changes every time the instrument is moved, involving a new calibration. The minimization now has six variables (four components of $^{\mathrm{ENU}}\mathbf{q}_{\mathrm{MNT}}$, δ, and ϑ_0), and one constraint ($^{\mathrm{ENU}}\mathbf{q}_{\mathrm{MNT}}$ has to be normed). This can be achieved using the *Sequential Least SQares Programming* (SLSQP) algorithm (Kraft, 1988).

For the A-LIFE data, the fitting determines a non-perpendicularity of the motors δ of 0.95° and an elevation offset ϑ_0 of -6.46°. The rotation quaternion $^{\mathrm{ENU}}\mathbf{q}_{\mathrm{MNT}}$ is reconstructed to (0.704, -0.044, -0.707, 0.043). While the non-perpendicularity and the elevation offset are constant over time, the rotation quaternion will change every time the instrument is moved.

Figure 3.11 shows the remaining deviation between the fitted instrument pointing and the actual sun position for all measurements in the A-LIFE campaign. The calibration is accurate to within 32 arcmin, corresponding to the apparent solar radius. The remaining inaccuracies are most likely due to the limited precision of the quadrant-sensor and the way the instrument is tracking the sun. The sensor has to pick up on brightness-differences over the sun. Also, high aerosol loads, cirrus, or thin water clouds blur out the sun disc, resulting in an equally lit quadrant-sensor further away from the sun's center. If the clouds are "streaky", this effect can occur in a certain direction. To avoid oscillation of the sensorhead the correction of pointing is damped. As a result, the instrument will most likely point to the lower left of the sun disc in the morning, and the upper left in the evening. Other disruptions might occur by the instrument having to "search" the sun after every scan. In the future, this effect should be minimized by used online-fitting of the mount skewness. Furthermore, the change of the apparent solar position due to atmospheric refraction has been ignored.

3.4.3. Langley calibration

Langley extrapolation is a method to enable sun-photometers to retrieve the total optical depth of the atmosphere, without the need for a radiometric calibration of the instrument in a laboratory (Forgan, 1994). The basis for the extrapolation is the *Bouguer–Lambert–Beer* law and its logarithmic representation:

$$I = I_0 \cdot \exp\left(-m\tau\right) \tag{3.43}$$

$$\ln\left(I\right) = \ln\left(I_0\right) - m\tau \tag{3.44}$$
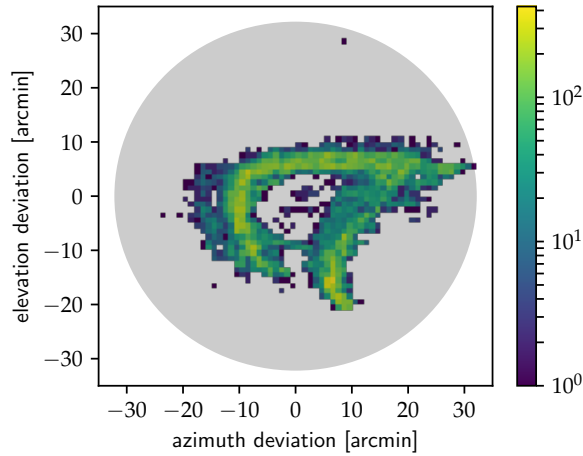
Figure 3.11.: Residual between calibrated and calculated sun position. Average apparent size of sun disk (32 arcmin) as reference (grey).

where I and I_0 are the measured and extraterrestrial irradiance, respectively. τ is the optical depth, and m the airmass factor. The latter describes the increase in the direct optical pathlength — and therefore the optical depth — from the sun to the detector. In the simplest geometric approach, $m = \cos^{-1}(\Theta)$, with the solar zenith angle Θ. A more elaborate airmass model taking into account atmospheric refraction and the curvature of the earth can be found in Kasten and Young (1989). Additionally, the extraterrestrial irrandiance I_0 has to be corrected for the seasonal variablity in sun-earth distance (Spencer, 1971).

Taking measurements at varying values of the airmass factor, and assuming the optical depth to be constant over time, the logarithm of the irradiance in Eq. (3.44) can be fitted as a linear function of m with slope τ. Extrapolating the linear fit to $m = 0$ yields $\ln(I_0)$. This value can then be used for reconstructing τ from measurements of I. Since only the ratio of the irradiances I and I_0 is used, they can be replaced by any detector signal S that is linear in I.

$$\tau = \frac{1}{m} \ln\left(\frac{I}{I_0}\right) = \frac{1}{m} \ln\left(\frac{S}{S_0}\right) , \qquad (3.45)$$

with $S = C \cdot I$ and $\tau = \tau_R + \tau_M + \tau_A$.

This τ is the combined value of Rayleigh (τ_R), trace gas (τ_M), aerosol (τ_A), and possibly cloud (τ_C) optical depths. The contribution from Rayleigh was determined according to Bodhaine et al. (1999), scaled with the measured air pressure. At around 500 nm, O_3 and NO_2 are the main contributors to the trace gas optical depth τ_M. Their profiles were taken from Anderson et al. (1986), and the corresponding absorption cross-sections from Bogumil et al. (2003). Assuming that no clouds are

present, subtracting these components from the total optical depth leaves only the contribution from aerosol.

According to Ångström (1929), the wavelength dependence of the aerosol optical depth can be described as

$$\tau_A(\lambda) = \beta\lambda^{-\alpha}, \tag{3.46}$$

with the Ångström turbidity coefficient β and the Ångström exponent α. The latter can be determined from our measurements using

$$\alpha(\lambda_1, \lambda_2) = -\frac{\ln\left(\frac{\tau_A(\lambda_2)}{\tau_A(\lambda_1)}\right)}{\ln\left(\frac{\lambda_2}{\lambda_1}\right)}. \tag{3.47}$$

for the reference wavelengths λ_1 and λ_2. This parameter of the wavelength dependence can be used to classify the aerosol type (Eck et al., 1999). In this work, 440 nm and 870 nm are used as reference wavelenths.

SSARA is usually calibrated once a year, either around March/April or around October/November at UFS Schneefernerhaus (2650 m) on Mount Zugspitze. Firstly, at that height, the contamination by boundary layer aerosols is minimal. Also, early/late in the year, convective processes over the measurement site are not prominent. Therefore, temporal homogenity of τ is found more frequently during that time. The calibration used for the data presented in this paper was done in November 2016.

4. Results

In this chapter, the retrieval described in Section 3.2 is tested. Section 4.1 shows the results of numerical studies using synthetic measurements simulated from cloud fields. These results have previously been published in Grob et al. (2019a). In a second step, the retrieval with the modification described in Section 3.2.3 is employed to SSARA measurements recorded during the A-LIFE field campaign. The two case studies shown there have been published in Grob et al. (2019b).

4.1. Numerical sensitivity studies studies

4.1.1. Synthetic cloud observations and atmospheric setup

To test the retrieval in cloudy conditions, synthetic cloud observations have been simulated with MYSTIC. Two types of cloud scenes are supplemented by simulated clear sky observations. The scenes only contain water clouds, ice clouds were not present. Their droplet size follow a gamma distribution:

$$n\left(r\right) = A \cdot r^{\alpha} \cdot \exp\left(-\beta r\right) \tag{4.1}$$

α and β are parameters of the size distribution, A the scaling factor. Same as for the aerosol, the cloud optical properties are determined using Mie calculations. The cloud fields are used with periodic boundary conditions, meaning they are infinitely replicated along the horizontal axes.

The US standard atmosphere is used (Anderson et al., 1986) for temperature, pressure and molecular scattering. Molecular absorption has been disabled. The ground surface is assumed to be fully absorbent. This was done to get the undisturbed signal of the clouds, uncontaminated by second-order effects generated by the ground or absorbing molecules. Effects of ground albedo on polarized sky radiance measurements from ground have been studied — for example — in Kreuter et al. (2010). The parameters for the two models chosen for the synthetic cloud observations are summarized in Table 4.1.

The synthetic "measurements" are taken in the so-called *principal plane*, spanned by the sensor, the zenith and the sun. Note, that the retrieval also accepts other scanning geometries. The viewing zenith angles are taken equidistant with 5°

Table 4.1.: Aerosol parameters used to generate synthetic cloud observations with MYSTIC; these settings have been combined with all cloud scenes.

parameter	fine mode	coarse mode
r_{eff} [µm]	0.05, 0.1, 0.25	1.0, 2.5
v_{eff} [-]	0.62	0.62
m_{r} [-]	1.4, 1.5, 1.6	1.4, 1.5, 1.6
m_{i} [-]	0.01	0.01
τ_{550} [-]	0.05, 0.1, 0.3, 0.5	0.05, 0.1, 0.3, 0.5

separation, centered around the sun at a zenith angle of 30°. This results in scattering angles between −55° (below the sun) and 115° (opposite the sun).

Cuboid clouds

The first set consists of cuboid clouds arranged for 25 % cloud cover. The size and pattern of the clouds was chosen to produce a clearing between them. This allows for principle plane scans to be performed in these cloud free "streets". Therefore, no cloud screening is necessary for these measurements.

Two cases have been selected. One with a cloud size and horizontal separation of 100 m, the other with 2 km. As an example, the liquid water path (LWP) pattern for the latter is shown in Fig. 4.1. The other case looks similar, but is scaled in the x-y-plane. The resulting distance of the scanning plane to the cloud is half the cloud size (e.g. 50 m and 1 km). Vertically, the clouds are located between 1 km to 1.5 km with a LWC of $0.5\,\text{g}\,\text{m}^{-3}$ and an effective radius of 5 µm. The effective variance v_{eff} for the gamma distribution of the droplet size is 0.1 (or $\alpha = 7$ in Eq. (4.1)). This results in an LWP of $250\,\text{g}\,\text{m}^{-2}$ and a cloud optical depth of roughly 75.

Figure 4.2 shows the all-sky total and polarized radiances, as well as the degree of linear polarization for the two cuboid cloud cases at a wavelength of 550 nm. The radiances are normalized to the extraterrestrial solar flux. For these simulations, the fine and coarse mode have an AOD of 0.1 or 0.05 and an effective radius of 0.1 µm or 1.0 µm, respectively. The effective variance is 0.62 and the refractive index 1.5 + 0.01i for both modes.

LES cloud fields

For testing the retrieval under more realistic conditions, clouds fields have been generated using UCLA-LES (Stevens et al., 2005). The domain has a horizontal extent of 6.4 km with a resolution of 25 m both, horizontally and vertically. It has a
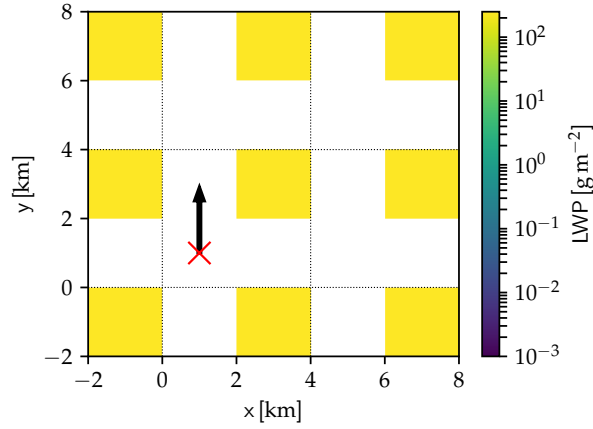
Figure 4.1.: Liquid water path pattern of 2 km cuboid clouds. The dashed black lines indicate the LES domain which is periodically repeated in x and y direction for the synthetic cloud observations. The red cross indicates the sensor position, the arrow points towards the sun. Scans are performed along the vertical. The sun is towards the top of the scene.

cloud coverage of roughly 29 %. The LWP for the domain is shown in Fig. 4.3. The red crosses indicate the sensor positions for generating the synthetic observations. The arrows points towards the sun in the respective case. These have been chosen to create four scenes with differing obstruction by clouds. The all-sky radiance and polarization distributions for these are shown in Fig. 4.4. For these, the aerosol situation is the same as in Fig. 4.2 (see Section 4.1.1).

For LES case 1, the sun is towards the left of the scene. Therefore, the principal plane is oriented also along the horizontal in Fig. 4.3. This produces a large cloud free portion in the scan. However, in the zenith there is a cloud close by. In all other cases, the sun is towards the top and the resulting principle plane oriented along the vertical in the LWP plot. Scenes 2–4 have increasing obstruction of the principal plane by clouds.

4.1.2. Retrieval results

In this section, the influence of clouds on the radiation field and retrieved aerosol properties is discussed. The detailed numeric retrieval results can be found in Tables 4.2 to 4.4.

The retrieval results are presented in the form of so-called *violin* plots. They are a visual representation of the density of the retrieved parameter for its corresponding true value. The horizontal marker depicts the median of this distribution. For reference, the 1:1 relation is shown as a dashed black line. The grey areas at the top
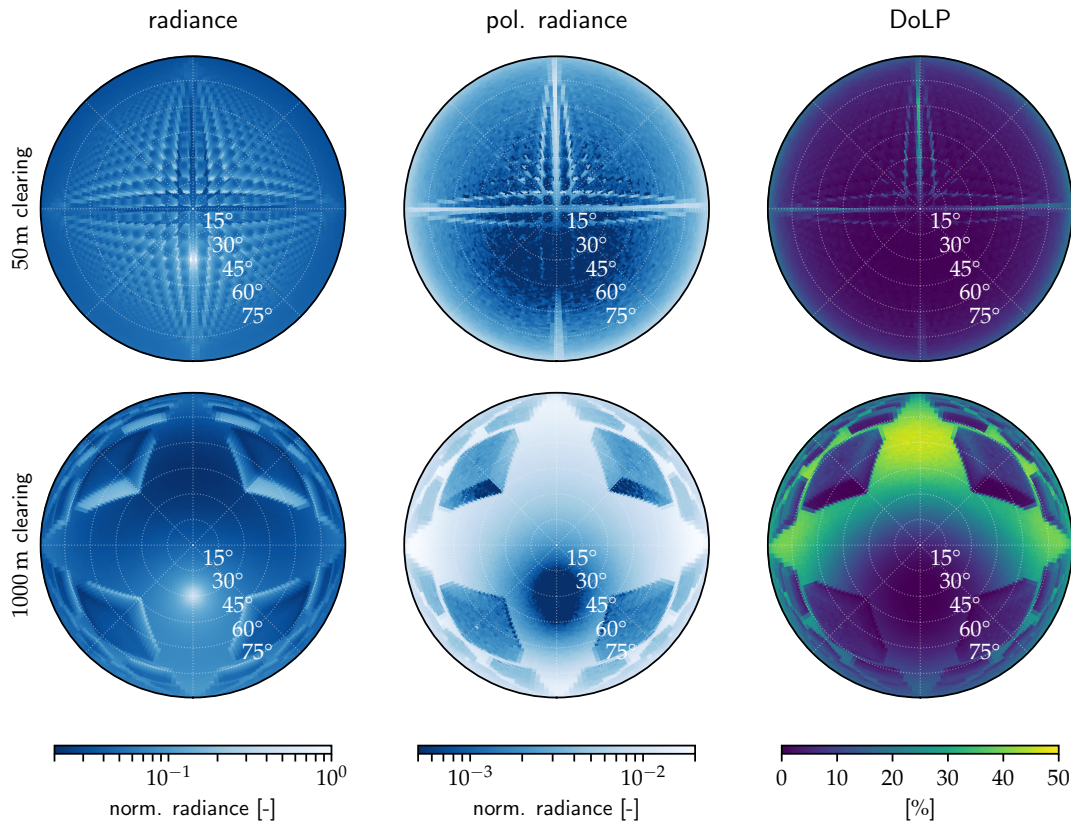
Figure 4.2.: All-sky distribution of total radiance (left column) and linear polarized radiance (middle column), and degree of linear polarization (right column) for the two cube cloud scenarios described in Section 4.1.1. The radiance is calculated at 550 nm and is normalized to the extraterrestrial solar flux. The degree of linear polarization is given in percent.
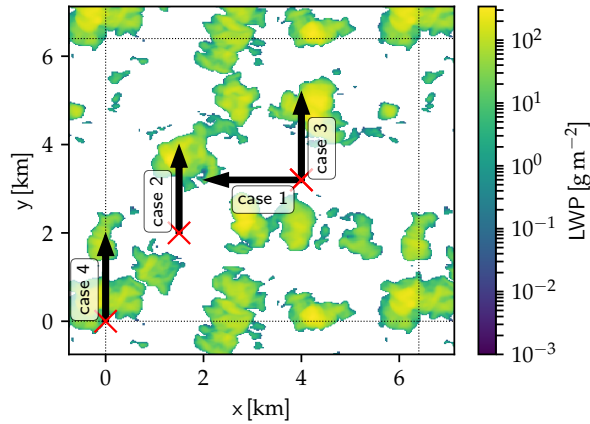
Figure 4.3.: Similar to Fig. 4.1, but for the LES cloud fields. Cases 1 and 3 have the same sensor position, but for case 1 the sun (and therefore scan direction) is to the left. For all the other cases, the sun direction is upward.

and bottom indicate the bounds imposed on the retrieval. The solid horizontal black line marks the prior for the parameter. Figures 4.5 and 4.12 show the combined AOD in both modes. Since this is not retrieved directly, there is no prior and the bounds are the sum of the bounds for the two modes.

To evaluate the retrieval results, some standard has to be established. Mishchenko et al. (2004) give measurement requirements on several aerosol properties for determining the forcing effect of aerosols on climate. The limit for total AOD is given as 0.04 or 10 %, whichever is larger. For this parameter, GCOS (2011) requires a similar accuracy (0.03 or 10 %). The effective radius should be retrieved to the greater of 0.1 μm or 10 %. The refractive index has to be known to 0.02 of its absolute value. However, to distinguish different source regions of - for instance - desert dust an accuracy of 0.01 or better might be required (Dubovik et al., 2002; Köpke et al., 1997).

Retrieval of aerosol properties under clear sky conditions

First, the performance of the retrieval has been tested under clear sky conditions. The results are shown in blue in Figs. 4.5 and 4.6. The retrieval is capable of reproducing the aerosol parameters to within 10 % of the original state in most cases, often much more accurate. The total AOD (Fig. 4.5) is slightly underestimated over the entire range, but with no more than 0.01 error for most values. Only high AOD loads have higher deviations (up to 6.2 % underestimation). The optical depth is retrieved equally well for fine and coarse mode aerosol, fulfilling the aforementioned GCOS requirements even for the individual modes. Fine mode effective radius can
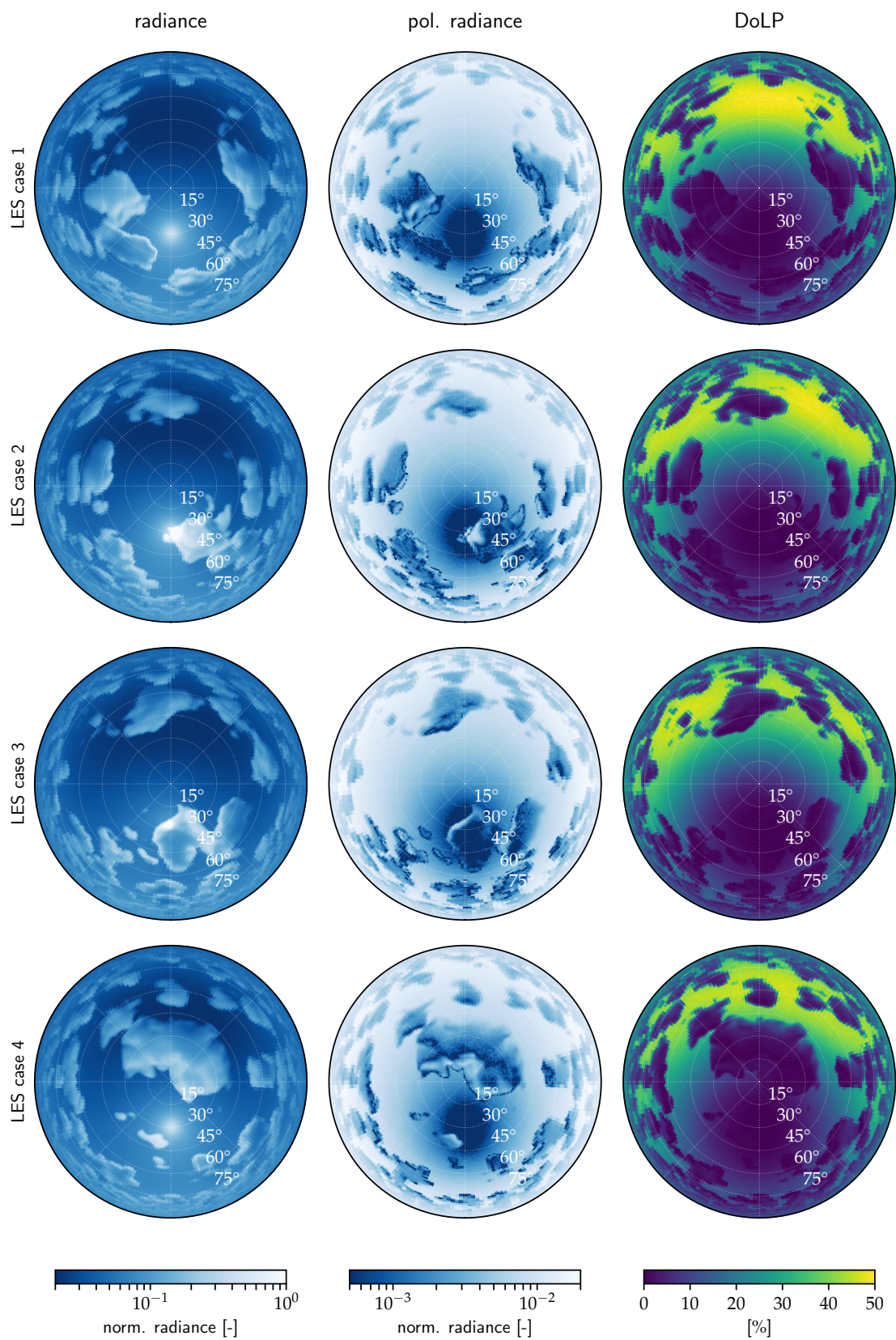
Figure 4.4.: Same as Fig. 4.2, but for the LES scenarios described in Section 4.1.1.

be reproduced to within 0.01 µm of the original value (subplot c). In the coarse mode, the error is larger, especially towards bigger particles (subplot d). The real part of the refractive index of the fine mode is well reconstructed with absolute deviations of less than 0.01 (subplot e). For the coarse mode, the discrepancies are - again - larger (subplot f). It appears that the retrieval does not deviate enough from the prior, which might be related to the inaccuracy in the effective radius for large particles.
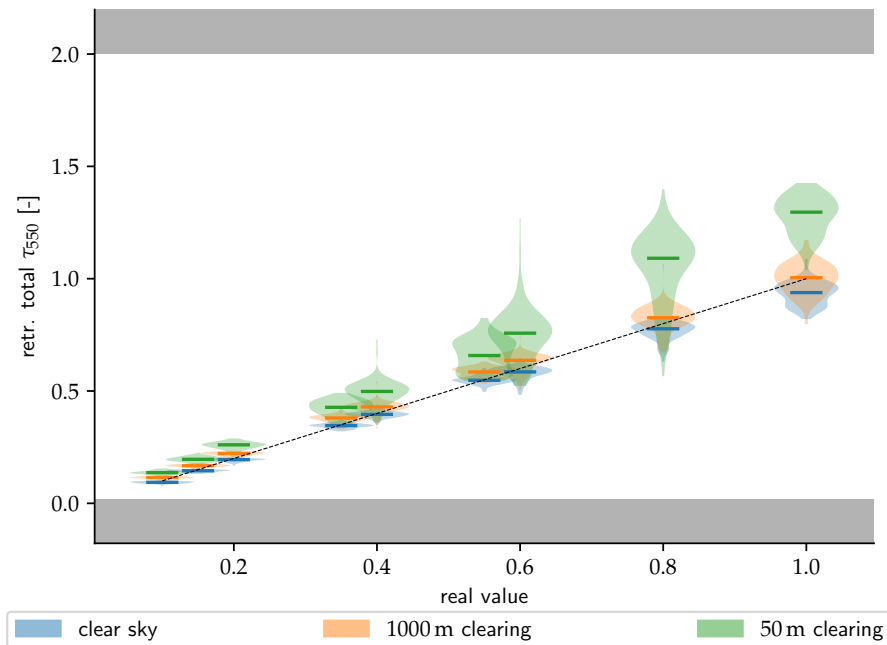
Figure 4.5.: Same as Fig. 4.6, but for the combined AOD in coarse and fine mode.

3D effects of clouds on retrieved aerosol properties

To quantify the effects of 3D cloud effects, the aerosol retrieval was run on the synthetic measurements of the cuboid clouds with 25 m and 1000 m clearing. These are taken in the principal plane in the cloud-free "street" between the clouds. Thus, no cloud-screening is necessary and all measurements can be used. The effects of clouds on the radiation field between them can be seen in the fish-eye panoramas in Fig. 4.8.

The presence of clouds increases the total radiance in large areas of the cloud free sky. At the same time, the polarized radiance is reduced. However, it can be seen that the deviation in polarized radiance is smaller than in total radiance. Figure 4.7 shows the effect for a principal plane scan between the cuboid clouds with 50 m
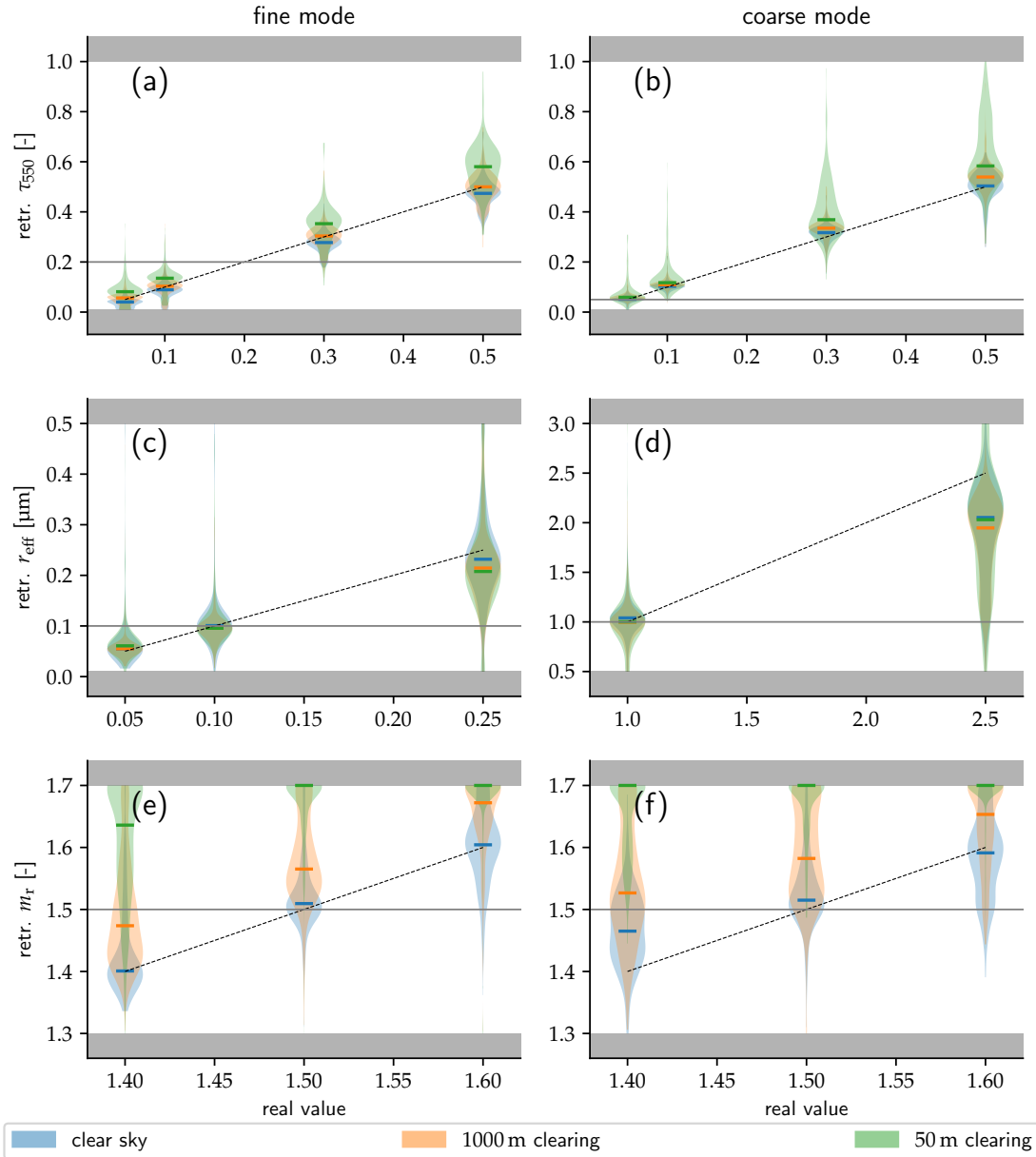
Figure 4.6.: Comparison of real (x axis) versus retrieved (y axis) aerosol properties for the fine (left column) and coarse mode (right column). The colors represent the three different cases. Blue is the clear sky test case. The other two are for cuboid clouds with 1000 m (orange) and 50 m clearing (green). The violins represent the density function of the retrieved values for the given real input. The marked values correspond to the median. The black dashed line depicts the 1:1 line. Grey shaded areas show the bounds imposed on the minimizer, the solid black horizontal line is the prior (see Table 4.1).

clearing in more detail. Again, it can be seen that for scattering angles between 30° and 100° on average the polarized radiance is less affected by the nearby clouds than the total radiance. The median of the total radiance is increased by up to 55 % at 85° scattering angle, while the median of the polarized radiance is decreased by about 25 % at the same position.
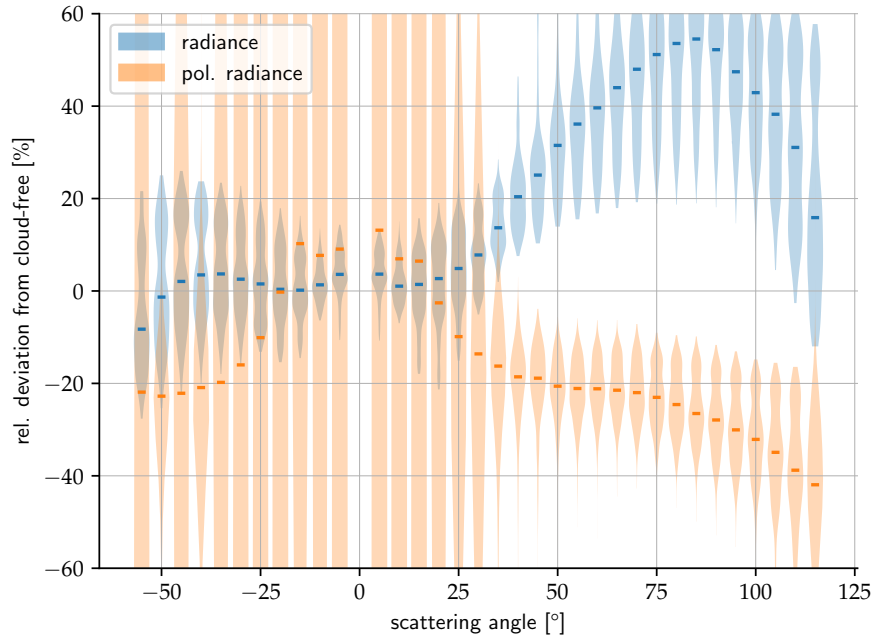
Figure 4.7.: Radiative effects of cuboid clouds with 50 m clearing on total radiance (blue) and polarized radiance (orange) of a principal plane scan at 550 nm. The horizontal markers represent the median.

This can be explained by light being "trapped" between the clouds by being reflected back and forth between the cloud sides. This light can be scattered towards the observer by aerosols or molecules above the clouds or in the cloud-free area between them, thereby adding to the total radiance in this area. On the other hand, due to the possibly many scattering events and their depolarizing effect, the resulting multiple-scattered light is less polarized, reducing the polarized radiance. Bringing the clouds closer together reinforces this effect. The deviations in radiation around the sun are small, because it is dominated by high levels single-scattered radiation as a result of the strong forward peak of the scattering phase function. Therefore, the relatively small modifications in the multiple-scattered radiation is negligible. Also, this forward scattered light is unpolarized. Due to its low absolute value, even small amounts of polarized light from multiple-scattering processes produce high relative deviations (seen in Fig. 4.8). The absolute value, however,

remains small.
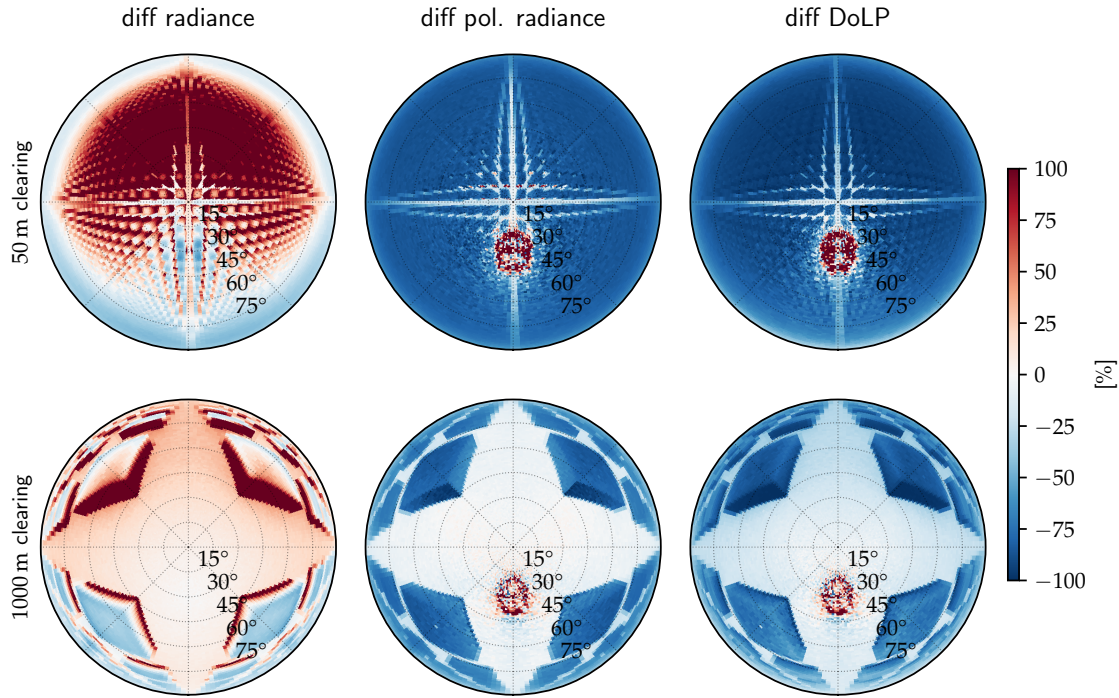
Figure 4.8.: Relative differences from clear sky for the cases and variables depicted in Fig. 4.2. Red colors indicate a higher magnitude compared to the clear sky, blue a lower magnitude.

The retrieved aerosol optical properties in these cuboid cloud scenes are shown in Figs. 4.5 and 4.6. The results for the 1000 m clearing case are presented in orange, 50 m clearing case in green. Naturally, the errors are higher than in the clear-sky case, especially for 50 m clearing.

The total AOD is overestimated by the retrieval, presumably because the forward model tries to reproduce the higher level of depolarization by a higher aerosol load (see Fig. 4.5). For 1000 m clearing, the deviations are still within the stipulated limits, even for the individual modes in most cases. Going down to 50 m, the errors increase up to 36 %. However, in 1D forward simulations, an increase of the AOD by one third, only results in an increase of total radiation of about 10 % to 30 %, not the 55 % shown above. This can be seen in Fig. 4.9. Higher radiance at scattering angles of 30° to 100° could also be reproduced by a higher refractive index. The retrieved refractive index is indeed overestimated in both modes. This

effect was also shown in Stap et al. (2016) for retrievals from satellite observations. The error increases with decreasing distance from the cloud. For 50 m clearing, the error is 0.24 for a real refractive index of 1.4. For larger inputs, the retrieved value reaches the limit of 1.7 from the microphysics parameterization, impeding further interpretation of this results in this case. For 1000 m clearing, the fine mode refractive index is overestimated by 0.7 (subplot e). The deviations for the coarse mode are of equal sign and only slightly larger (subplot f). The deviations are similar for fine and coarse mode (Fig. 4.6, subplots a and b). The retrieval of the effective radius does not seem to be sensitive to the presence of clouds or the distance to them (subplot c). Supposedly, most of the information about the size distribution is in the forward scattering intensity peak (area around the sun), which is not heavily influenced by the clouds (see Fig. 4.8, left column). The accuracy requirements are still met, regardless of cloud distance For coarse mode (subplot d), no adverse effects can be detected apart from the underestimation of large particles already visible in the clear-sky case.

Screening of cloudy measurements

To validate the retrieval results in the LES cloud fields, first the performance of the cloud screening has to be evaluated. Figure 4.10 shows the method in action for an example of all the LES cloud cases. It displays both total and polarized radiances measured in the respective case (crosses) and the corresponding clear sky case as reference (orange dashed line). Deviations between the two are therefore solely due to cloud radiative effects. The cloud screening reliably detects the strong and sudden peaks that can be attributed to measurements of cloud sides or bottoms (red crosses), for example at scattering angle $-30°$ in LES case 1 or at scattering angles $>30°$ in LES case 4. Also the clouds close to the horizon are detected in all cases, even though the deviations from the clear sky are rather small. In case 1 (first row), it can be seen that the screening is sometimes too strict. The measurements at scattering angles between $20°$ and $30°$ are falsely classified as cloudy. However, this does not hurt the retrieval, as the overall radiance distribution can still be properly reproduced. Maybe the cloud screening cloud be relaxed in the future for a better yield of measurement points.

Sometimes the measurements directly adjacent to cloudy areas are also detected as cloudy due to the large gradients. As a result, small cloud-free patches in between clouds are "filled" (classified as cloudy). This behaviour can be seen in LES case 4 at around scattering angles $75°$ and $100°$. It can be argued that these pixels are likely to have large contamination by 3D effects, so screening them might be favourable.
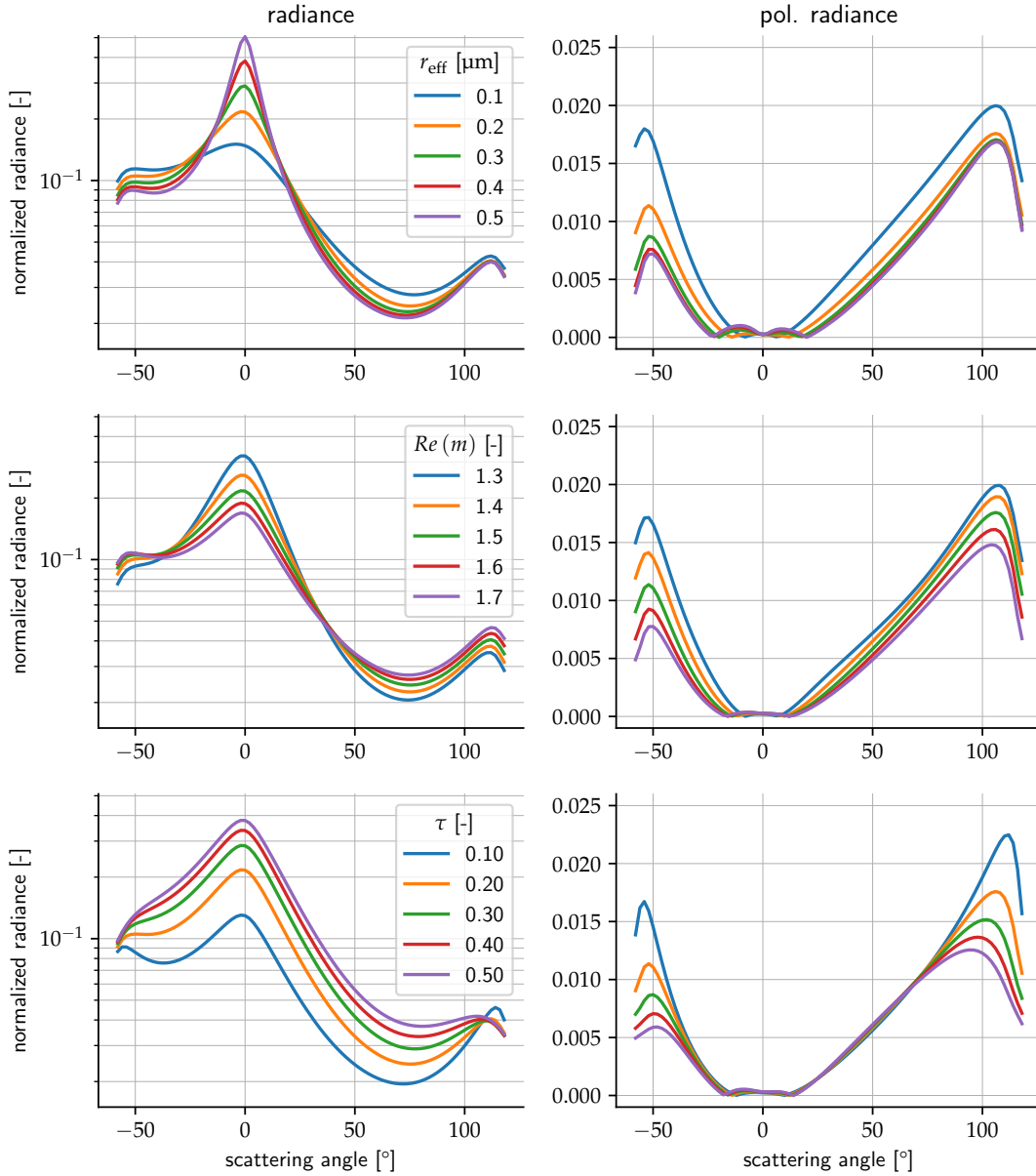
Figure 4.9.: Sensitivity of total and polarized radiance at $500\,\text{nm}$ to changes in aerosol parameters. Only one aerosol mode is used with $r_{\text{eff}} = 0.1\,\mu\text{m}$, $v_{\text{eff}} = 0.62$, $m = 1.5 + 0.01\text{i}$, and $\tau_{550} = 0.2$. Ground albedo is 0. The respective parameter is varied over the given values. The simulations are performed with *LIRA-V* in the principal plane at a SZA of 30°.
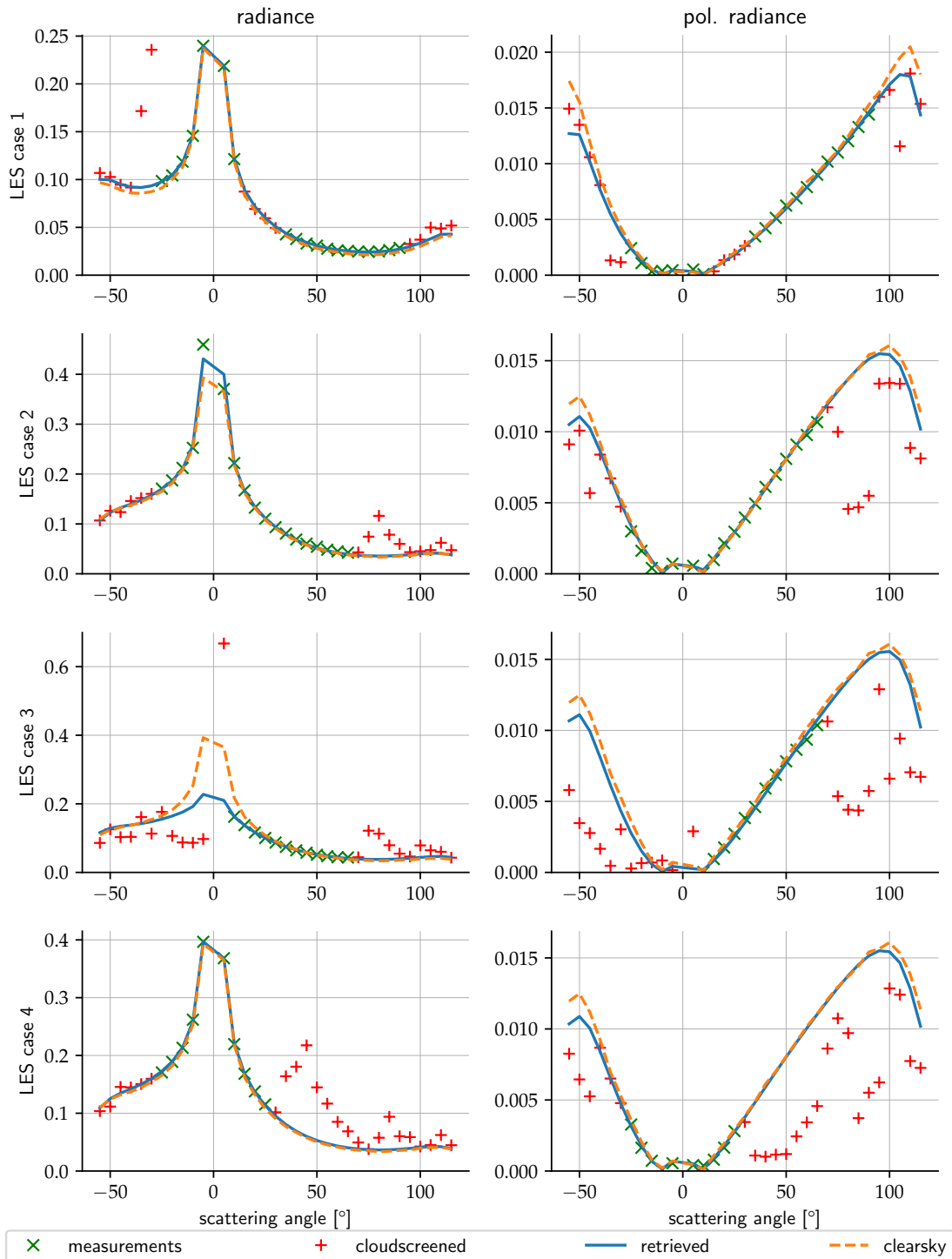
Figure 4.10.: Normalized total radiances (left column) and polarized radiances (right column) at 500 nm for the four LES cloud cases. Measurements are represented by the crosses, red crosses have been removed by the cloud-screening. The solid blue line has been retrieved from the remaining green points. The orange dashed line represents the clear sky case with the same aerosol situation.

Retrieval performance in LES cloud fields

The four LES cloud fields illustrate 3D cloud radiative effects in a more realistic situation. Figure 4.11 visualizes the deviation of total and polarized radiance, and degree of linear polarization for the LES scenes from the clear sky case. Overall, the positive offset in total radiance and negative offset in polarized radiance described in Section 4.1.2 can be seen in cloud free areas. Also, the higher level of linear polarized radiation around the sun is present. In this area, the cloud in front of the sun in LES case 3 more or less disappears in the polarized radiance. A small spec of relatively high polarized light can be seen towards the sun at an zenith angle of about 45°. This shows that clouds can also produce a positive bias in polarized radiation. The same behaviour is present in LES case 4 on the edge of the cloud in the zenith. Also, the total radiance can be increased and decreased by clouds. LES case 3 shows an increase towards the edges of the clouds and a decrease in its center.

The results of running the retrieval for the LES cloud scenes are shown in Figs. 4.12 and 4.13, as well as Tables 4.3 and 4.4. With the exception of case 3, the retrieval still performs well. For cases 1, 2 and 4 results are comparable to the 1000 m clearing cuboid cloud case, sometimes even better. The total AOD is overestimated by usually no more than 0.03, with the exception of high loads in LES case 2. Both modes contribute equally to the uncertainty (subplots a and b in Fig. 4.13). The effective radius is reconstructed to 0.02 µm for the fine mode (subplot c). In the coarse mode, the size of large particles is underestimated again (subplot d). Also, as in the cuboid cloud cases, the refractive index is overestimated by up to 0.08 in the fine mode (subplot e). The coarse mode refractive index behaves similarly, but occasionally underestimating high values (subplot f). However, the absolute error is still of the same magnitude as in the 1000 m clearing cuboid cloud case.

In LES case 3 the retrieval errors are significantly larger. The total AOD is overestimated for low aerosol loads, and underestimated for higher loads (total AOD over 0.2). In contrast to all other cases, the deviations in the coarse mode AOD are larger than in the fine mode. This might again be a result of the inaccuracies in the other coarse mode aerosol parameters that impede the retrieval of a reasonable solution. It is however noteworthy, that the effective radius is still retrieved reliably to about 0.03 in fine and 0.11 in coarse mode, again with the exception of larger particles. The real part of the refractive index is overestimated in all cases and reaches the upper bound of the inversion, possibly inducing errors in other parameters.

To understand why the performance is limited in case 3, we compare with case 4. The former has only a single larger portion of clear sky towards the zenith. The direct forward scattering region around and especially below the sun is covered
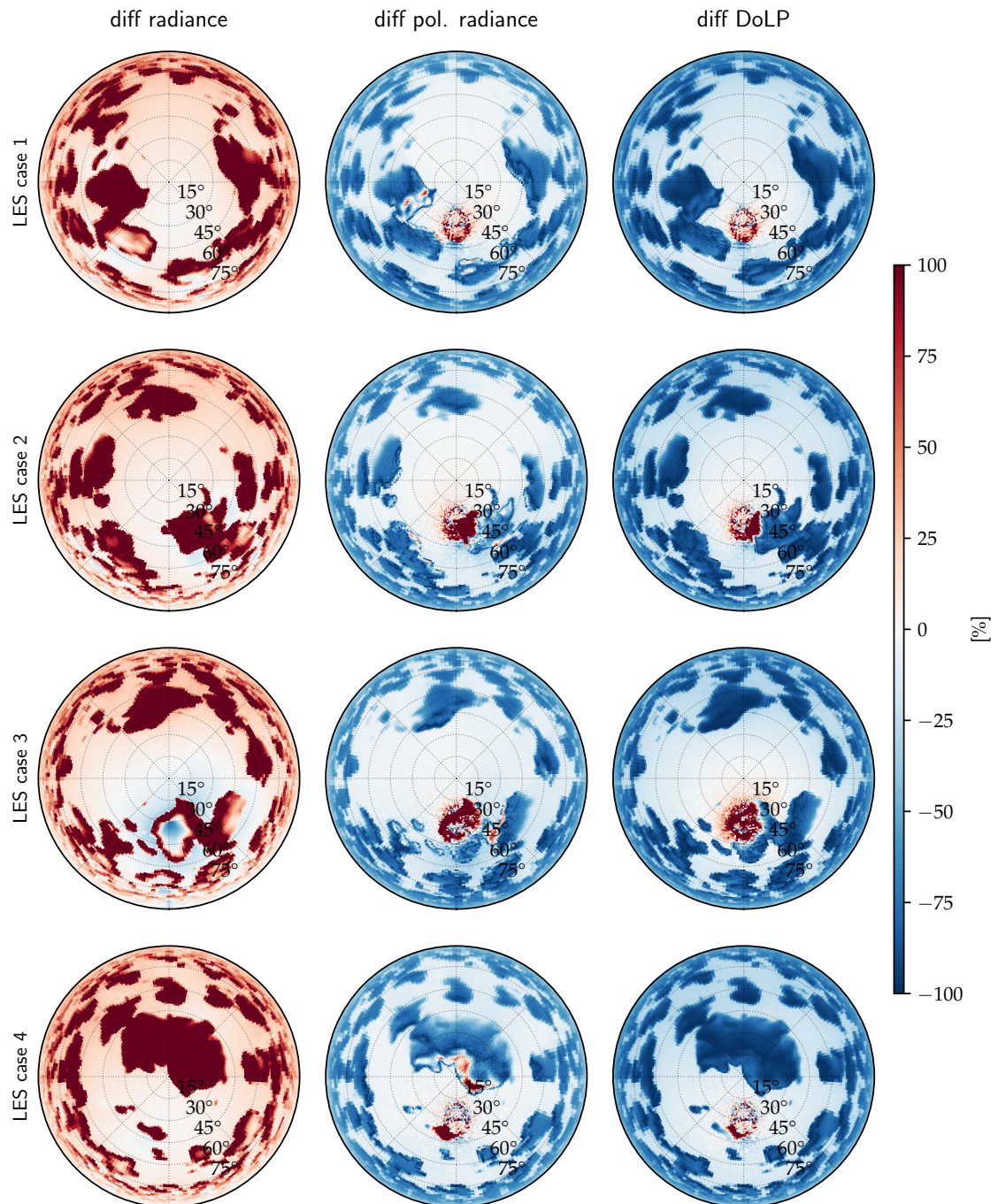
Figure 4.11.: Same as Fig. 4.8, but for the LES cases.

by a cloud. For case 4 the opposite is the case, with the aureole fully visible to about 30° above and below the sun. This can also be seen from the remaining measurements after the cloud screening in Fig. 4.10. It seems that the forward scattering peak contains more information than the measurements at scattering angles between 10° and 70°, especially for the coarse mode. This makes sense, keeping in mind that the forward scattering peak becomes more prominent for larger particles, and could also explain the underestimation of the AOD in the coarse mode described earlier. Also, the only remaining measurements close to the sun in case 3 are subject to severe 3D effects, visible by the discrepancy between the crosses and the dashed orange line in Fig. 4.10. The radiance in this area is decreased, a situation not present in any of the other LES cases, which could be the reason why the AOD is under- and not overestimated.

With the exception of case 3, the retrieved values are within the acceptable limits. The preexisting difficulties with retrieving the effective radius of large coarse mode particles, as well as the index of refraction are again visible.
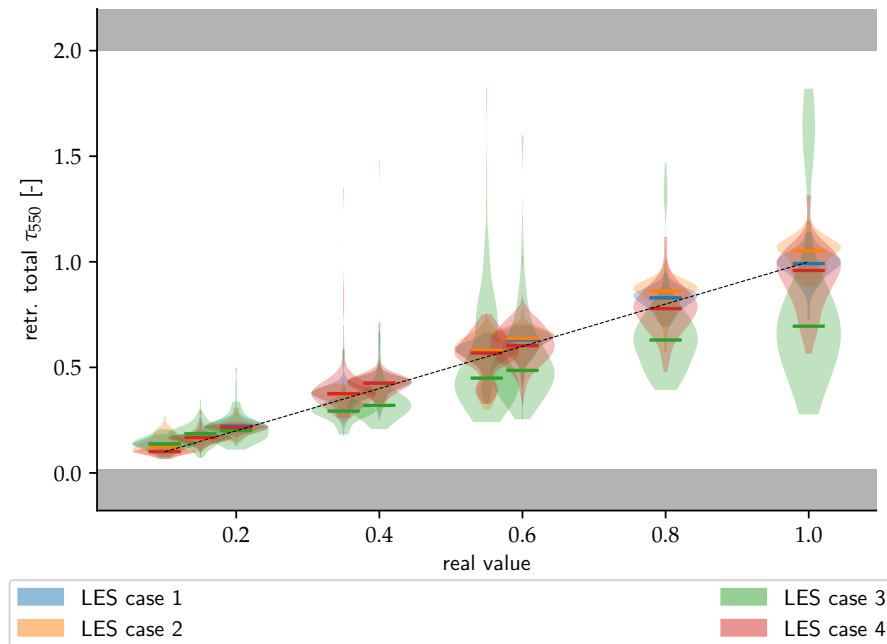
Figure 4.12.: Same as Fig. 4.13, but for the combined AOD in coarse and fine mode.
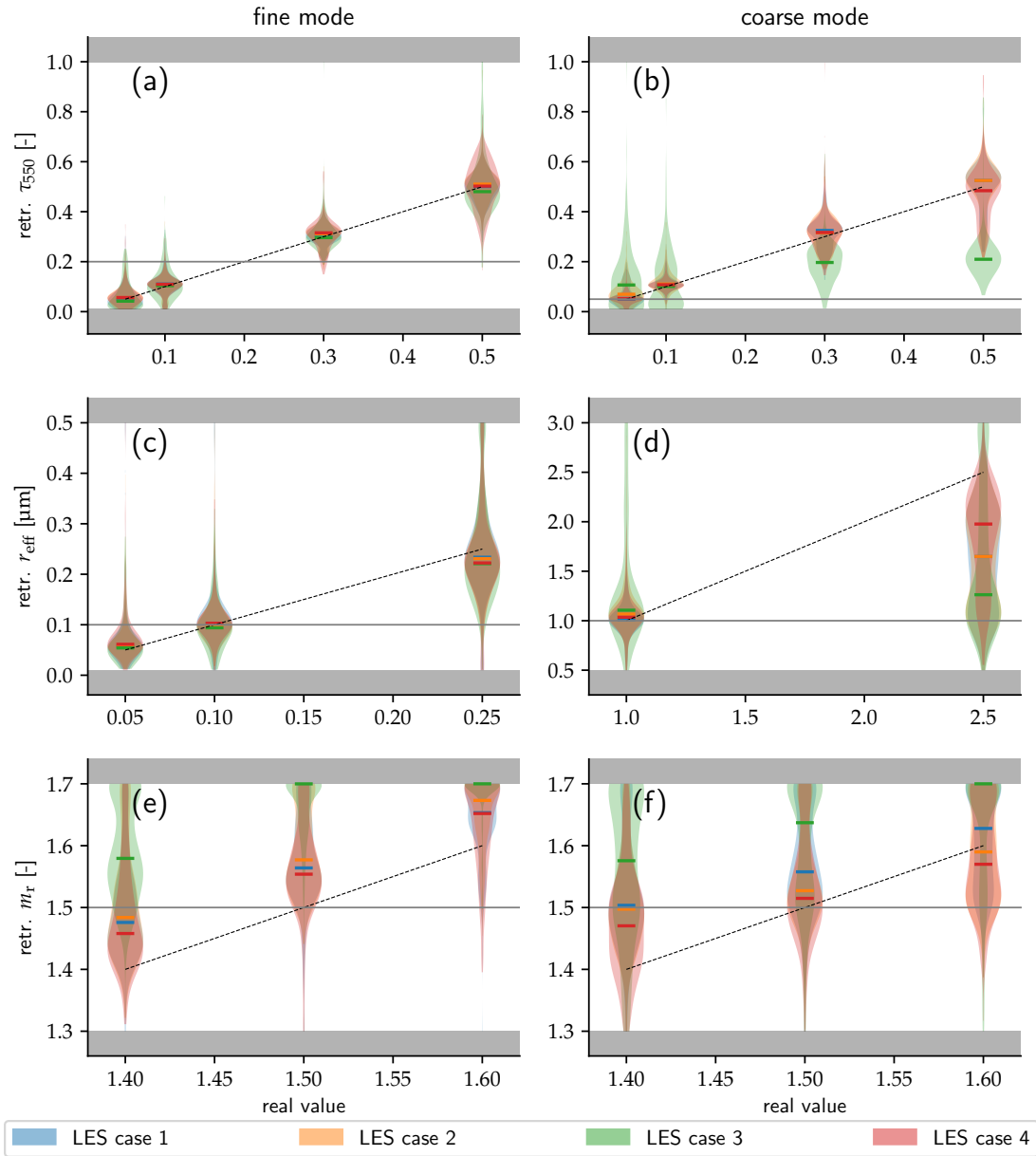
Figure 4.13.: Same as Fig. 4.6, but for the LES cases 1 (blue), 2 (orange), 3 (green) and 4 (red).

Table 4.2.: Retrieved parameters for the corresponding real value in the clear sky and cube cloud scenes (with 50 m and 1000 m clearing). Δ is the relative error of the retrieved value calculated as $\Delta = (x_{\mathrm{real}} - x_{\mathrm{retr}}) / x_{\mathrm{real}}$.

parameter	real	clear sky		1000 m		50 m	
		retr.	$\Delta\,[\%]$	retr.	$\Delta\,[\%]$	retr.	$\Delta\,[\%]$
	0.10	0.09	−6.6	0.11	14.4	0.14	36.6
	0.15	0.15	−3.2	0.17	11.6	0.20	30.6
	0.20	0.19	−2.7	0.22	10.8	0.26	30.2
	0.35	0.35	−1.1	0.38	8.6	0.43	22.1
τ_{550} (total) [-]	0.40	0.40	−1.0	0.43	7.3	0.50	24.5
	0.55	0.55	−0.4	0.58	6.3	0.66	19.6
	0.60	0.58	−2.5	0.64	6.1	0.76	26.2
	0.80	0.78	−2.9	0.83	3.3	1.09	36.4
	1.00	0.94	−6.2	1.00	0.4	1.30	29.6
	0.05	0.04	−19.6	0.06	13.0	0.08	62.6
τ_{550} (fine) [-]	0.10	0.09	−11.0	0.10	3.5	0.14	35.3
	0.30	0.28	−7.5	0.30	1.3	0.35	17.6
	0.50	0.47	−5.2	0.50	0.0	0.58	16.1
	0.05	0.05	2.3	0.06	13.0	0.06	18.1
τ_{550} (coarse) [-]	0.10	0.10	3.1	0.11	8.9	0.12	17.3
	0.30	0.32	5.6	0.34	11.7	0.37	22.9
	0.50	0.50	0.7	0.54	7.8	0.58	16.7
	0.05	0.05	9.0	0.05	9.6	0.06	21.6
r_{eff} (fine) [μm]	0.10	0.10	0.7	0.10	−4.0	0.10	−4.4
	0.25	0.23	−7.3	0.21	−14.2	0.21	−16.9
r_{eff} (coarse) [μm]	1.00	1.04	4.0	1.00	−0.2	1.00	0.1
	2.50	2.05	−17.9	1.95	−22.1	2.03	−18.8
	1.40	1.40	0.1	1.47	5.3	1.64	16.9
m_{r} (fine) [-]	1.50	1.51	0.6	1.57	4.3	1.70	13.3
	1.60	1.60	0.3	1.67	4.5	1.70	6.2
	1.40	1.47	4.6	1.53	9.0	1.70	21.4
m_{r} (coarse) [-]	1.50	1.51	1.0	1.58	5.5	1.70	13.3
	1.60	1.59	−0.5	1.65	3.3	1.70	6.2

Table 4.3.: Same as Table 4.2, but for the LES cases 1 and 2.

parameter	real	LES case 1		LES case 2	
		retr.	Δ [%]	retr.	Δ [%]
τ_{550} (total) [-]	0.10	0.14	37.0	0.12	23.3
	0.15	0.17	10.7	0.16	8.6
	0.20	0.22	10.9	0.21	6.0
	0.35	0.38	7.4	0.37	6.2
	0.40	0.43	6.6	0.42	6.2
	0.55	0.58	5.5	0.58	5.9
	0.60	0.63	5.1	0.64	6.2
	0.80	0.83	3.7	0.86	7.7
	1.00	0.99	-0.8	1.05	5.3
τ_{550} (fine) [-]	0.05	0.05	-3.3	0.06	12.1
	0.10	0.11	10.4	0.11	7.7
	0.30	0.30	1.6	0.31	3.5
	0.50	0.50	0.1	0.51	2.1
τ_{550} (coarse) [-]	0.05	0.05	1.6	0.07	39.1
	0.10	0.11	7.2	0.11	10.5
	0.30	0.32	8.3	0.32	5.2
	0.50	0.52	4.9	0.52	5.0
r_{eff} (fine) [µm]	0.05	0.06	14.3	0.06	14.9
	0.10	0.10	3.1	0.10	-0.5
	0.25	0.23	-6.5	0.23	-7.6
r_{eff} (coarse) [µm]	1.00	1.01	0.8	1.07	6.7
	2.50	1.65	-34.1	1.65	-34.0
m_{r} (fine) [-]	1.40	1.48	5.4	1.48	6.0
	1.50	1.56	4.3	1.58	5.1
	1.60	1.65	3.3	1.67	4.6
m_{r} (coarse) [-]	1.40	1.50	7.4	1.50	7.0
	1.50	1.56	3.8	1.53	1.8
	1.60	1.63	1.7	1.59	-0.6

Table 4.4.: Same as Table 4.2, but for the LES cases 3 and 4.

parameter	real	LES case 3		LES case 4	
		retr.	Δ [%]	retr.	Δ [%]
τ_{550} (total) [-]	0.10	0.14	37.1	0.10	1.0
	0.15	0.19	23.8	0.17	11.3
	0.20	0.20	0.4	0.22	8.0
	0.35	0.29	-16.3	0.38	7.2
	0.40	0.32	-20.0	0.42	6.2
	0.55	0.45	-18.3	0.57	3.2
	0.60	0.49	-19.1	0.60	0.5
	0.80	0.63	-21.3	0.78	-2.7
	1.00	0.70	-30.5	0.96	-4.1
τ_{550} (fine) [-]	0.05	0.04	-16.0	0.06	12.9
	0.10	0.10	3.9	0.11	9.5
	0.30	0.30	-1.2	0.32	5.2
	0.50	0.48	-4.0	0.50	0.5
τ_{550} (coarse) [-]	0.05	0.11	113.4	0.05	4.3
	0.10	0.10	0.9	0.11	7.7
	0.30	0.20	-34.4	0.32	5.7
	0.50	0.21	-58.1	0.48	-3.2
r_{eff} (fine) [μm]	0.05	0.05	8.2	0.06	22.7
	0.10	0.09	-6.0	0.10	2.9
	0.25	0.22	-11.6	0.22	-11.0
r_{eff} (coarse) [μm]	1.00	1.11	10.6	1.04	3.5
	2.50	1.26	-49.5	1.98	-20.9
m_{r} (fine) [-]	1.40	1.58	12.8	1.46	4.1
	1.50	1.70	13.3	1.55	3.6
	1.60	1.70	6.2	1.65	3.2
m_{r} (coarse) [-]	1.40	1.58	12.5	1.47	5.0
	1.50	1.64	9.1	1.51	1.0
	1.60	1.70	6.2	1.57	-1.9
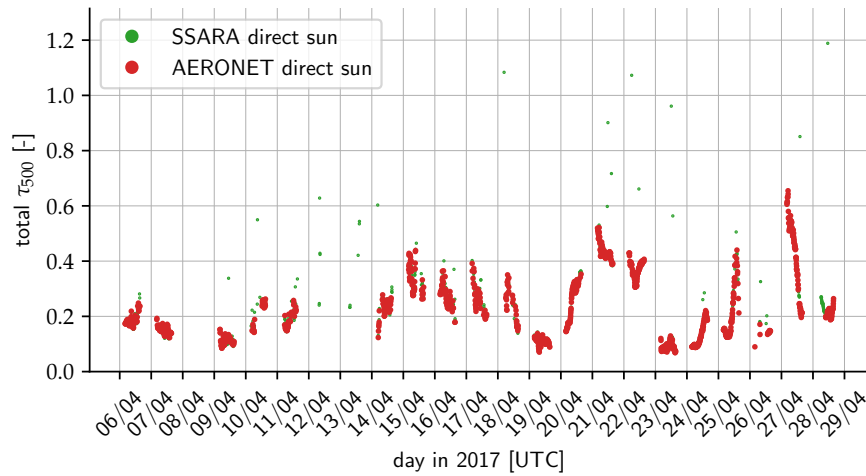
Figure 4.14.: 500 nm AOD during ALIFE campaign time from AERONET (red) and SSARA (green) direct sun measurements

4.2. Retrieval of aerosol properties from SSARA observations

The following measurements have been performed during the A-LIFE field campaign. SSARA was installed on top of a building of the University of Cyprus at Limassol (N 34.674°, E 33.040°). The AERONET station CUT-TEPAK is installed about 300 m to the east. The Leipzig Aerosol and Cloud Remote Observations System (LACROS, Bühl et al. (2013)), including a Polly^{XT} lidar system (Engelmann et al., 2016), was located 400 m to the north east.

Officially, the intensive observation period with the DLR Falcon 20E stationed in Paphos started on 3 April 2017 and ended 30 April 2017. Between 6 and 28 April, SSARA continously performed direct sun observations. These have been interleaved with sky radiance scans in the almucantar and principal plane at pre-selected solar zenith angles. Almucantar plane scans have been carried out at every 5° of solar zenith angle (SZA) between 35° and 80°, principal plane at 10° intervals between 30° and 80° of SZA. The data of channel 11 (1020 nm) were excluded from the analysis as it intermittently provided faulty values during the measurement campaign.

4.2.1. Campaign overview

In the following, a synoptic overview of the campaign time is given. The 500 nm AOD is shown in Fig. 4.14 for the time SSARA was present. Figure 4.15 is the 440–
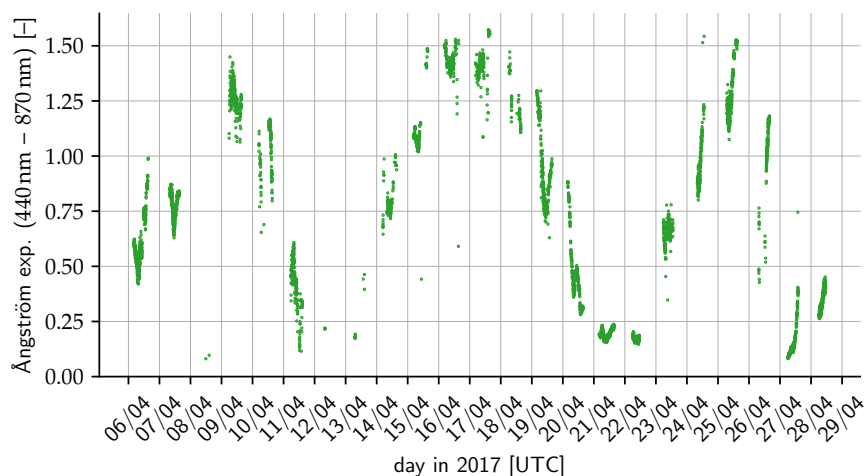
Figure 4.15.: Ångström exponent between 440 nm and 870 nm during ALIFE campaign time from SSARA direct sun measurements.

870 nm Ångström exponent for the same time. They are determined from SSARA direct sun observations as described in Section 3.4.3. The campaign featured several more or less distinct phases. This is in part a recap of a presentation given by H. Huntrieser (DLR-IPA) at the first A-LIFE workshop in March 2018, Emails describing the meteorological situation by various scientists (Bernadette Weinzierl, Albert Ansmann and others) during the time, and the campaign plan–of–the-days available on the A-LIFE website (`https://www.a-life.at/plan-of-the-day`). The cloud situation can easily be judged from the images taken by the camera installed on SSARA's sensorhead, taking pictures every 10 s. For judging the history of the airmasses, I used FLEXPART backward trajectory simulations (Stohl et al., 2005) from Nicosia, kindly provided by Christoph Knote (LMU München). The occurrence of forest fires is judged using the FINN model fire emission product (Wiedinmyer et al., 2011) obtained from `https://www.acom.ucar.edu/acresp/forecast/fire-emissions.shtml`.

On 6 April a strong dust outbreak occurred with two distinct dust layers, with the lower being Arabian dust and the upper Saharan dust aerosol. These two types are named by their source region and differ by their chemical composition, which is clearly visible in Lidar signal backscatter ratio (Mamouri et al., 2013, e. g.). Arabian dust originates from the Middle East and the Arabian peninsula, whereas Saharan dust comes from the more western parts of northern Africa. However, from a sun photometer only the column–integrated aerosol is visible and the two layers can not be observed separately. Also the different wavelength dependence of the scattering coefficient for the two aerosol types cannot be separated. The

remnants of the lower Arabian aerosol mixed more and more with pollution and maritime aerosol from Crete and Turkey over the next days. On 12 and 13 April lots of clouds were present with intermittent rain. Between the convective clouds, the remainder of the polluted Arabian dust was observed in in situ measurements. Often also cirrus clouds were present. In the following days, a mixture of local pollution with rests of the different dusts lingered over Limassol.

A new outbreak of Saharan dust occurred around 19 April. It was first sampled by the DLR Falcon over Malta on 19 April and was transported westwards, and arrived in Cyprus on 20 April, as discussed in the second case study. The airmass was traced over its path by the aircraft and ground stations in Malta, Finokalia (Crete), and Cyprus. Beginning 21 April, additional air from the eastern parts of the Sahara mixed in. The high dust load prevailed until 23 April, when cleaner air from south–east Europe arrived.

On 25 April, also from the north, biomass burning aerosol reached the measurement site. It was mostly washed out with the rain on 26 April. The prevailing winds shifted further to the east, bringing in pollution from Turkey and Syria. Starting 26 April, more dust from the Arabian peninsula stared to arrive. SSARA's involvement in the campaign ended on 28 April with the observation of pollution aerosols from Turkey, mixed with anthropogenic sources from Greece.

4.2.2. Case studies

For testing our retrieval data from 17, 20 and 25 April were selected for more in depth case studies. To evaluate of the retrieval performance the results are compared to same requirements that were used in the numerical studies. These were taken from Mishchenko et al. (2004) and allow for a maximum deviation of 0.04 or 10 % in AOD, 0.1 µm or 10 % in effective radius, and 0.02 in the refractive index. Since the true value is unknown, the results were compared with the AOD retrieved from direct sun observations and the level 1.5 data of the AERONET version 3 inversion. Level 1.5 data were used, since level 2.0 did not include refractive index values for the chosen dates. It should be noted that the AERONET inversion uses the same refractive index for both modes.

Since the plots showing the results are the same for all three days, they will be described here first. Figures 4.17, 4.21 and 4.24 show the aerosol optical depth at 500 nm for these three days. Orange and blue crosses mark values retrieved by the inversion from principal plane and almucantar scans, respectively. The residual in the minimization is shown as an indicator of the performance of the retrieval for a given measurement. The values obtained from direct sun observations are displayed as reference, with green dots representing AERONET L2 data and the red ones SSARA measurements. The latter was determined using the method described in Section 3.4.3. Figures 4.18, 4.22 and 4.28 show all retrieved aerosol

parameters for fine and coarse mode, separately. Again, blue corresponds to values obtained from principal plane, orange from almucantar scans. The AERONET points are the results of the AERONET inversion for hybrid (red) and almucantar scans (green). Since AERONET uses a common refractive index for fine and coarse mode, this value is shown for both modes (subplots (e) and (f)). It should amount to a weighted mean of the values we retrieved for the two modes, and therefore lie somewhere between those. To facilitate the comparison of the retrieval results with direct sun measurements and AERONET values, the optical depth is evaluated at 500 nm in the following case studies.

The retrieval results for the remaining campaign days are shown in Appendix B. The plots are equivalent to Figs. 4.17 and 4.18. Some days have been omitted, because there was no data available.

17 April 2017: Cloudy day

17 April has been chosen to illustrate the retrieval behaviour during cloudy phases. Around sunrise and between roughly 11:00 UTC and 14:15 UTC, convective clouds have been present at the measurement site. This can also be deduced from the gap in AERONET direct sun AOD data. Cirrus clouds already appeared around 10:30 UTC, and persisted almost until 16:00 UTC. Figure 4.16 shows four snapshots of the cloud situation during that day. The pictures have been taken with a camera installed coaxially with the SSARA sensorhead.

In the early morning (until around 04:30 UTC Fig. 4.17) an elevated AOD is retrieved. This coincides with the presence of convective clouds also visible in the top left panel of Fig. 4.16. As shown in sensitivity studies, these might lead to an overestimation of the AOD. However, it could indicate that additionally the AOD is increased, for example due to hygroscopic growth of aerosol particles in humid air. The same can be observed in Fig. 4.17 for the convective period in the afternoon between 11:00 UTC and 13:00 UTC. Here it should be noted that for the corresponding scans, the residual is sometimes slightly higher, indicating a less reliable retrieval result. This is shown by the black tickmarks in Figs. 4.17 and 4.18. Most of the time, the residual is below 0.075, but spikes up to 0.15. Interestingly, the residual reaches some of its highest values between 06:00 UTC and 07:00 UTC, even tough the retrieved values agree well with the value obtained from direct sun observations and AERONET inversion results. Starting around this time, the AOD is overestimated by up to 0.1 during clear sky periods. Small gaps in the AERONET direct measurements indicate the presence of clouds or high variability in the aerosol. Again, some deviation in the retrieval (generally overestimation) is to be expected here. Note that perfect agreement between the values retrieved from sky radiance observation and from direct sun observations cannot be expected. The reason for this might be inhomogeneity in the aerosol, either in space (maritime
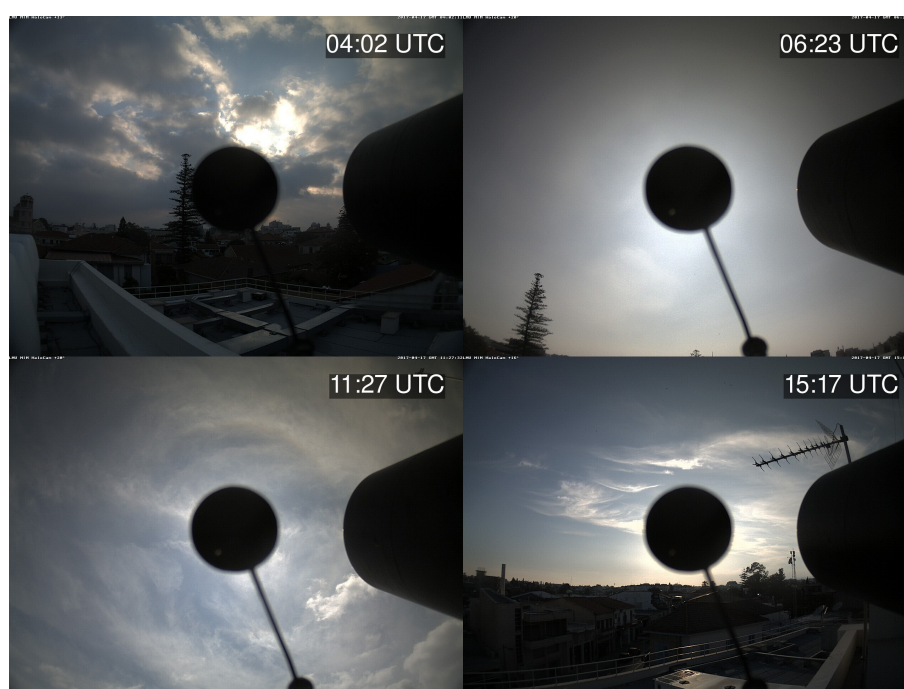
Figure 4.16.: Sky camera images for 17 April 2017. The convective clouds in the early morning and afternoon are visible. The persisting cirrus clouds towards the evening can be seen.

towards ocean, anthropogenic aerosols towards city/industry), or in time, as one scan can take up to 15 min. Also, the inversion makes the assumption of the aerosol being located in the lower 2 km of the atmosphere, which could in part explain the differences. Other explanations could be measurement errors or systematic effects of the retrieval. This can also explain the differences between the results of almucantar and principal plane scans.

In Fig. 4.18a and Fig. 4.18b, the AOD is separated into fine and coarse mode. Over the entire day, the aerosol optical depth is dominated by the fine mode. This compares well to the AERONET inversion datapoints. The contribution of the coarse mode is larger compared to AERONET. It should be noted here that – in contrast to the AERONET inversion – we do not use the total AOD from direct sun observations as a constraint for our minimization. This is not feasible for a method designed to be employed in cloudy situations, where such measurements might not be available.

The retrieved effective radius of the fine mode (Fig. 4.18c) is mostly consistent over the entire day, including the cloudy period in the afternoon. This insensitivity of the effective radius to the presence of clouds was also observed in the numerical studies. However, the increased values in the morning and evening should be noted. This seems to be a systematic pattern, the reason for which is still unknown. When compared to AERONET our fine mode effective radii are somewhat smaller, but within the 0.1 µm requirement. The same is true for the coarse mode (Fig. 4.18d). Here, the AERONET inversion suggests the presence of large particles with an effective radius of around 2 µm between 07:00 UTC and 10:00 UTC. The values we obtain are smaller. Although previous sensitivity studies have shown that our retrieval has the tendency to underestimate the size of large coarse mode particles, independent measurements would be needed to further investigate the discrepancy.

The retrieved real part of the refractive index changes rapidly for fine mode particles (Fig. 4.18e). High values can be observed in the aforementioned times with clouds present. This behaviour is again consistent with the results of the numerical studies, where clouds induce an overestimation of the index of refraction. The results for the coarse mode (Fig. 4.18f), are smoother in general. The retrieved value mostly stays close to the prior of 1.5, which might be caused by a low sensitivity to this parameter. The refractive index derived from AERONET ranges from 1.33 to 1.48. At around 07:00 UTC there is an obvious discrepancy between values obtained from hybrid and almucantar scans. The values below 1.35 between 08:30 UTC and 10:00 UTC seem unrealistic, as all expected aerosol types have a higher refractive index.
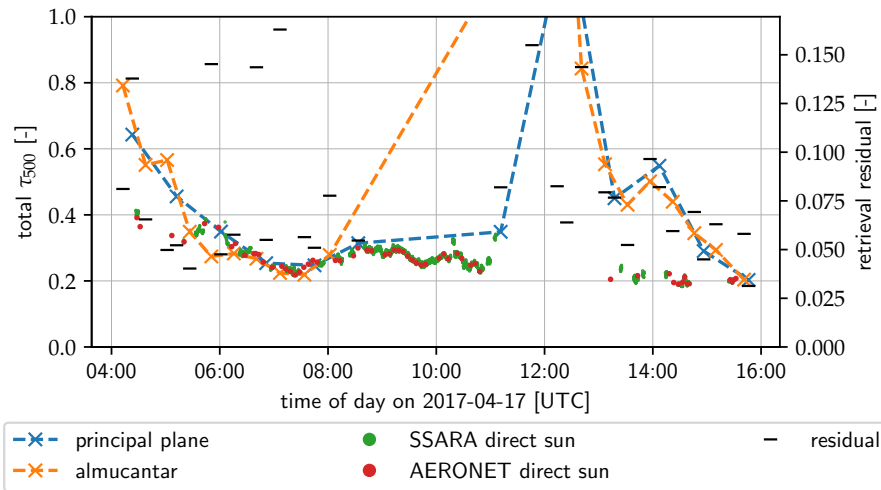
Figure 4.17.: Total AOD at 500 nm for 17 April 2017. Crosses indicate values retrieved from SSARA almucantar (orange) and principal plane (blue) scans. Green and red dots are from direct sun observations with SSARA and AERONET, respectively. The thin black markers represent the residual of the retrieved solution.

20 April 2017: Clear sky day with arriving Saharan dust layer

20 April was a clear-sky day. Starting in the late morning (07:00 UTC, 10:00 LT), the AOD increased. This can be attributed to the arrival of a Saharan dust outbreak over Cyprus from the west. Figure 4.20 shows the attenuated backscatter at 1064 nm of the Polly[XT] lidar. An aerosol layer is visible between roughly 2 km and 4 km beginning with thin filaments at around 04:00 UTC, and increasing in depth towards noon. Polly[XT] also provides measurements of the particle linear depolarization ratio (PLDR) at 532 nm that can be used to discriminate between types of aerosol (Baars et al., 2016). In this layer, PLDR values around 25 % are observed and clearly identify the aerosol as desert dust (Freudenthaler et al., 2009; Müller et al., 2003). Another indication for the arrival of desert dust is the strong decrease in the 440 nm–870 nm Ångström exponent shown in Fig. 4.19.

The AOD derived from the inversion of SSARA sky radiance measurements is overestimated by sometimes up to 0.3, in the early morning and the late afternoon and evening, when compared with the values obtained from direct sun observations from SSARA and AERONET (see Fig. 4.21). Judging from the residual, the results are all equally trustworthy, barring two exceptions between 12:00 UTC and 13:00 UTC. Again, some slightly higher residuals are visible around 07:00 UTC.

An increase in the coarse mode AOD is clearly visible in Fig. 4.22b, starting at around 07:00 UTC. The retrieved values agree well with the AERONET inversion results. This increase is consistent with the arrival of Saharan dust which contains
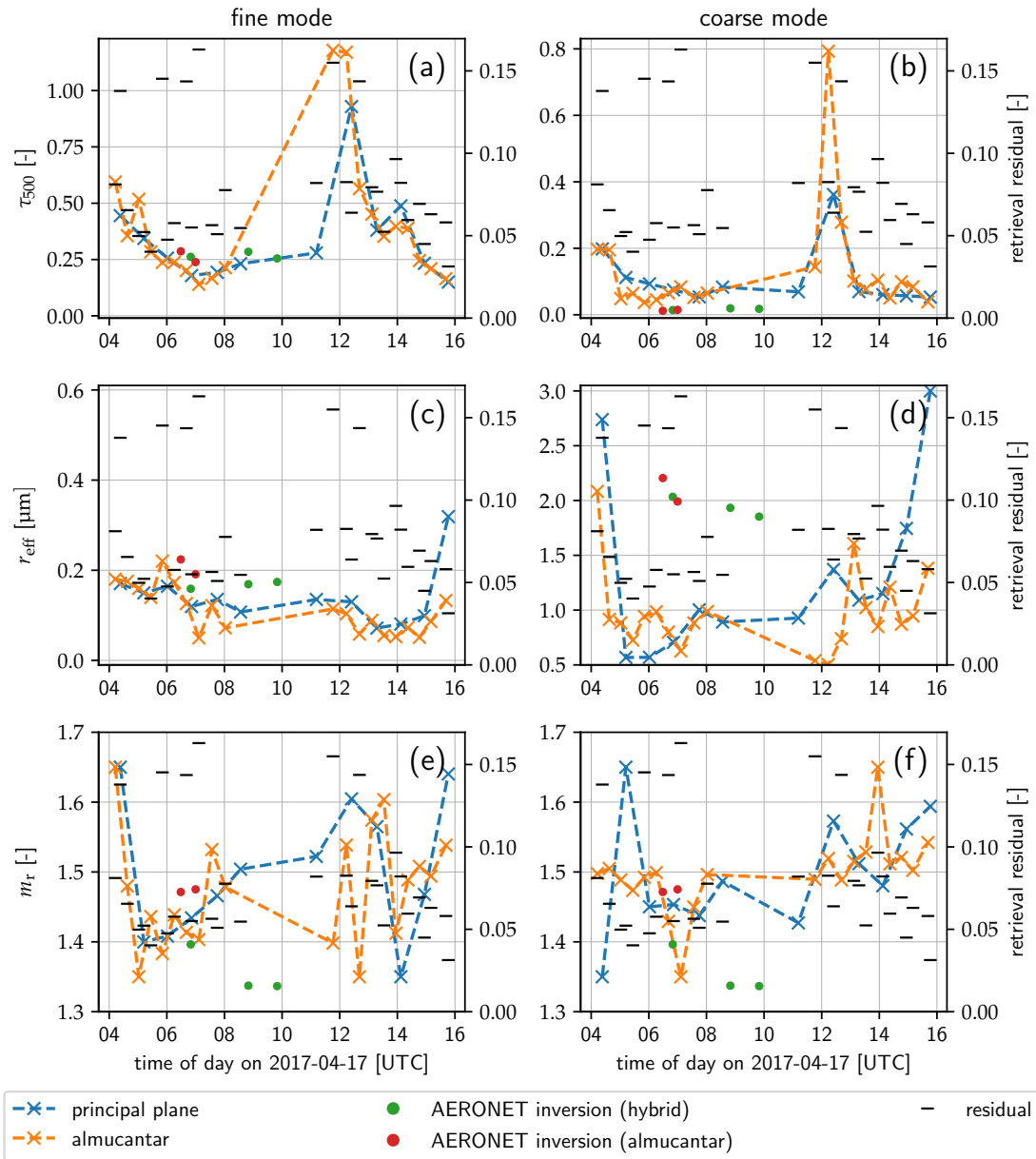
Figure 4.18.: Fine and coarse mode trends of aerosol optical depth (τ_{500}), mode effective radius (r_{eff}), and real part of refractive index (m_{r}) for 17 April 2017. Values obtained from principal plane scans are marked by blue crosses, those from almucantar scans are orange. The residual of the retrieval is shown by black markers. AERONET version 3 level 1.5 inversion results are shown as green and red dots, corresponding to retrieval of almucantar and hybrid scans, respectively. The refractive index is assumed to be equal for both modes in the AERONET retrieval.
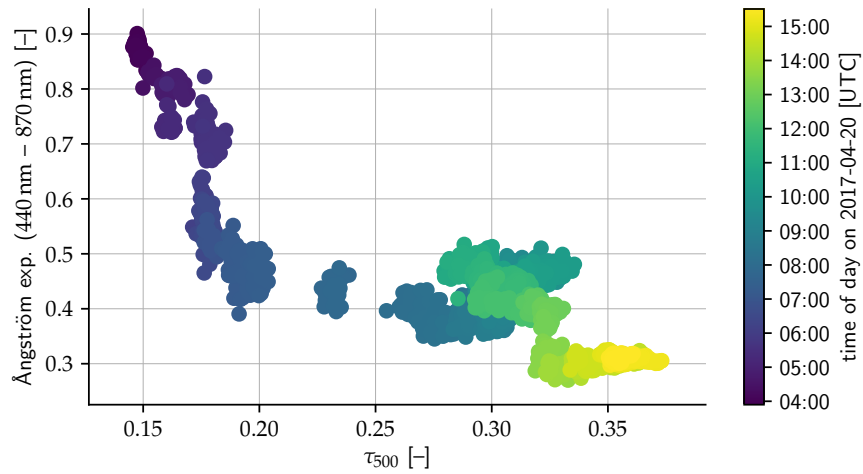
Figure 4.19.: Ångström exponent between 440 nm and 870 nm plotted versus the AOD at 500 nm on 20 April 2017, derived from SSARA direct sun observations. The decrease around 07:00 UTC marks the arrival of desert dust aerosol.
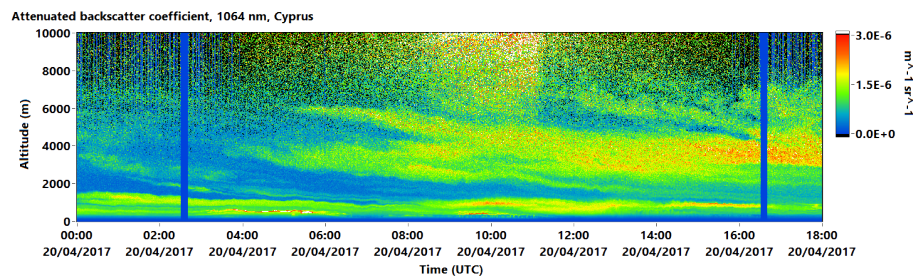
Figure 4.20.: 1064 nm attenuated backscatter (in $m^{-1} sr^{-1}$) measured by a Polly^{XT} lidar at the LACROS site on 20 April 2017.

larger particles. Consequently, the overestimation of the total AOD retrieved from SSARA sky radiance measurements has to be caused by the fine mode (see Fig. 4.22a). Also it is not consistently retrieved from principal plane and almucantar scan patterns. Again, the deviation in the retrieved total AOD from the direct sun observations is owed to the fact that this value is not used as a constraint in the inversion.

The effective radius of the fine mode (see Fig. 4.22c) is hitting its lower limit of 0.05 µm, only increasing in the evening again. This most likely causes a lot of the deviations in the other parameters of the fine mode. AERONET finds larger fine mode particles, again by up to about 0.1 µm. Apart from the single outlier at about 13:00 UTC, coarse mode effective radius is retrieved quite consistent over the entire day (Fig. 4.22d). Also, it agrees well with the AERONET inversion results. For values around 1.5 µm the retrieval proved to be reliable in the sensitivity studies.

For the real part of the refractive index of the fine mode (Fig. 4.22e), the retrieved values show different behaviour depending on the scan pattern. While the almucantar values stay around to 1.5, those from principal plane oscillate between the lower and upper limits of 1.35 and 1.65, respectively. In the coarse mode (Fig. 4.22f), the agreement between the patterns in better, again with many values around 1.5. This agrees well with the AERONET inversion, which produces only slightly lower values. However, since this is also the prior and large discrepancies between values derived from the two scan patterns are visible, this might also be the result of lacking sensitivity to this parameter.
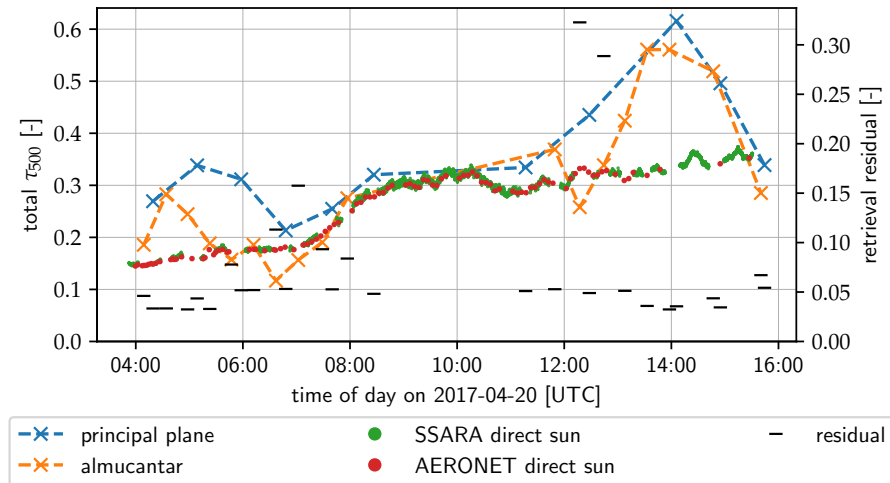
Figure 4.21.: Same as Fig. 4.17, but for 20 April 2017.
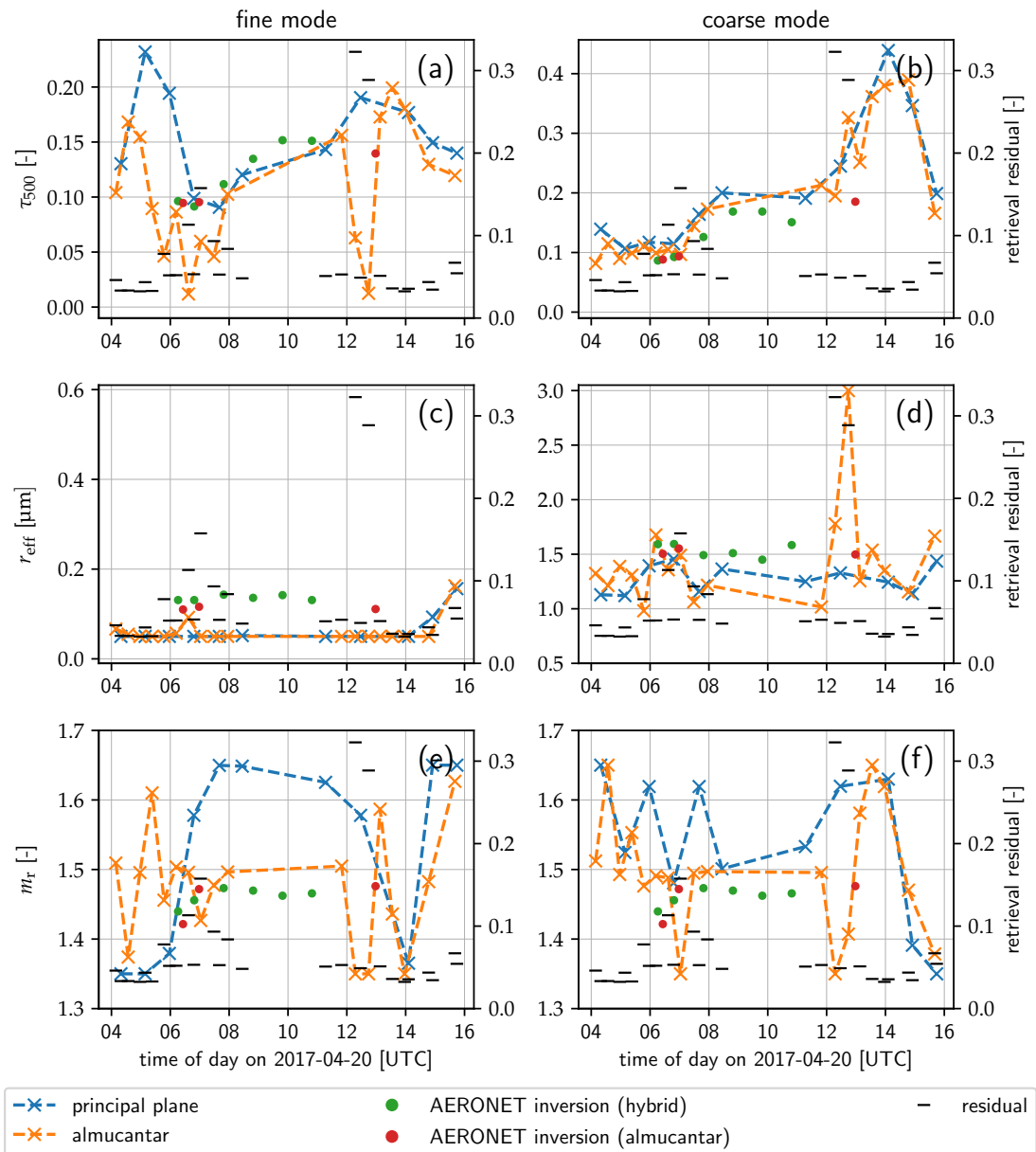
Figure 4.22.: Same as Fig. 4.18, but for 20 April 2017.

25 April 2017: Clear sky with arriving biomass burning layer
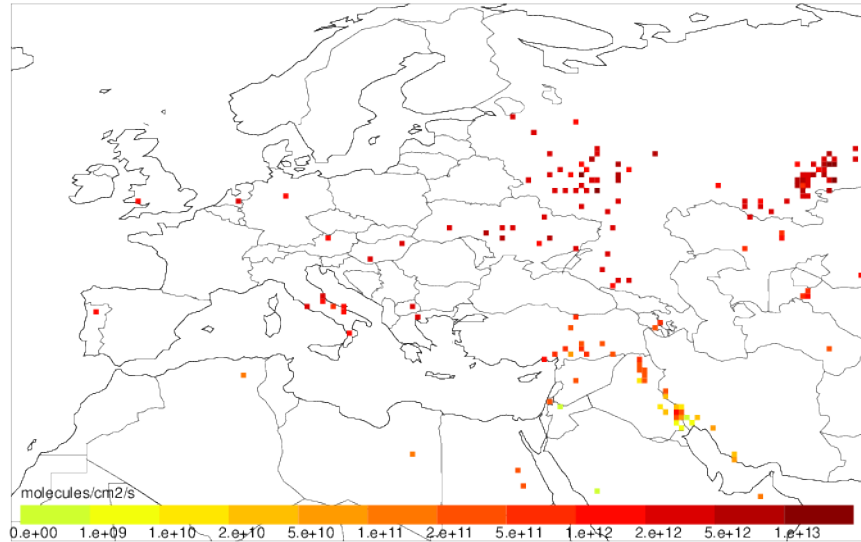
Figure 4.23.: FINN model fire emissions for 25 April 2017. Forest fires close to the Turkish–Syrian boarder emitting highly absorbing aerosol later detected in Limassol.

25 April began with a low aerosol load. Starting 09:30 UTC, the AOD increased, as can be seen in Fig. 4.24. The same is true for the Ångström exponent in Fig. 4.26, which is derived from SSARA direct sun observations. At an AOD of almost 0.45, it reached values above 1.5, some of the highest observed during the entire campaign. These values are an indication for biomass burning. Looking at the backwards trajectories in Fig. 4.27 in conjunction with fire emissions shown in Fig. 4.23, the aerosol was probably emitted by forest fires on the Turkish southern coast and the Syrian boarder area. Between roughly 12:30 UTC and 14:00 UTC clouds were developing, as can be seen in Fig. 4.25. The AOD then decreases, with the Ångström exponent remaining at around 1.5.

The retrieval residual shown in Fig. 4.24 has a few outliers around 13:00 UTC, which is to be expected as this coincides with the presence of clouds. With a few exceptions, the AOD trend is represented to within 0.1 (Fig. 4.24). The increase in AOD with the arrival of the new aerosol layer is detected, as is the decrease in the afternoon. The missing SSARA direct values in the morning are due to instrument problems. In the evening, the quadrant sensor had problems tracking the sun. This was caused by thick and "streaky" aerosols and clouds that lead to a directional smearing of the solar disc. The mode separated AOD in Fig. 4.28a
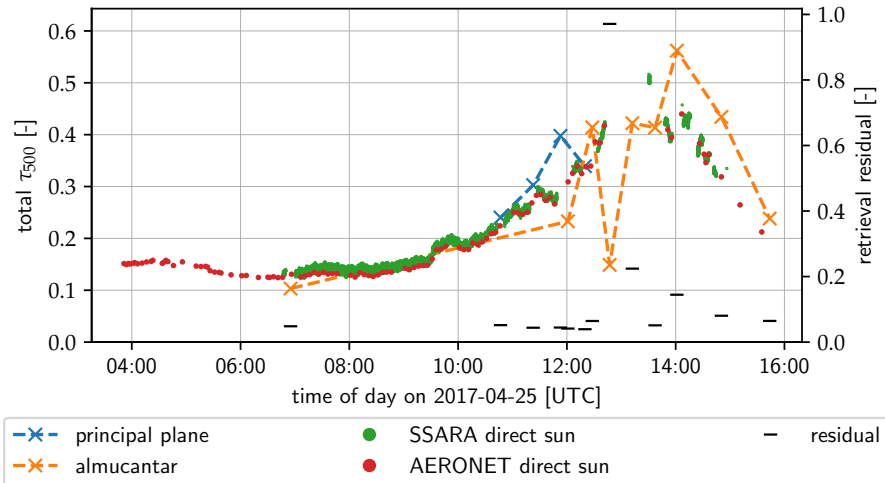
Figure 4.24.: Same as Fig. 4.24, but for 25 April 2017.

Figure 4.25.: Sky camera image for 25 April 2017. The clouds in the afternoon are visible.

and Fig. 4.28b shows that the aerosol and its increase is mainly attributed to the fine mode. This further supports the thesis of fresh biomass burning aerosols (Eck et al., 2003; Remer et al., 1998).
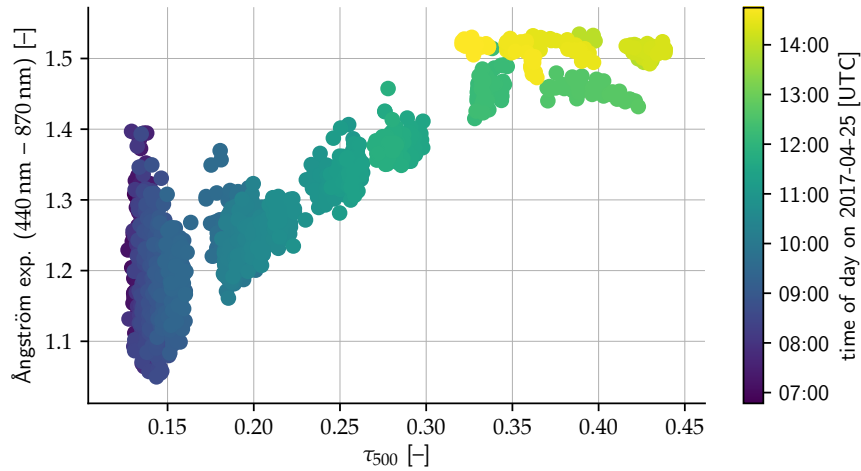
Figure 4.26.: Same as Fig. 4.19, but for 25 April 2017. The increase around 09:30 UTC marks the arrival of biomass burning aerosol.

The fine mode effective radius shown in Fig. 4.28c agrees well with AERONET from the almucantar scans. Those obtained from the few principal plane scans appear to be to low. Apart from the measurement at 07:00 UTC and the outlier around 13:00 UTC, the coarse mode particles are retrieved relatively small compared to AERONET which finds values above $2\,\mu m$ (see Fig. 4.28d). This might either be caused by their low abundance in this case or the retrievals tendency to underestimate the size of large coarse mode particles.

The refractive index is retrieved close to values of 1.5 over the entire day in both modes (Fig. 4.28e and Fig. 4.28f), again with the exception of the outlier in the afternoon. The combined–mode value from AERONET also starts at around 1.5 and decreases over noon to below 1.4.

However, it is interesting that our retrieval results are still relatively good in this case, considering we fixed the imaginary part of the refractive index to 0.01 (see Table 4.1). This value is significantly to low for biomass burning aerosols, which can reach values more than an order of magnitude larger (Bond and Bergstrom, 2006).
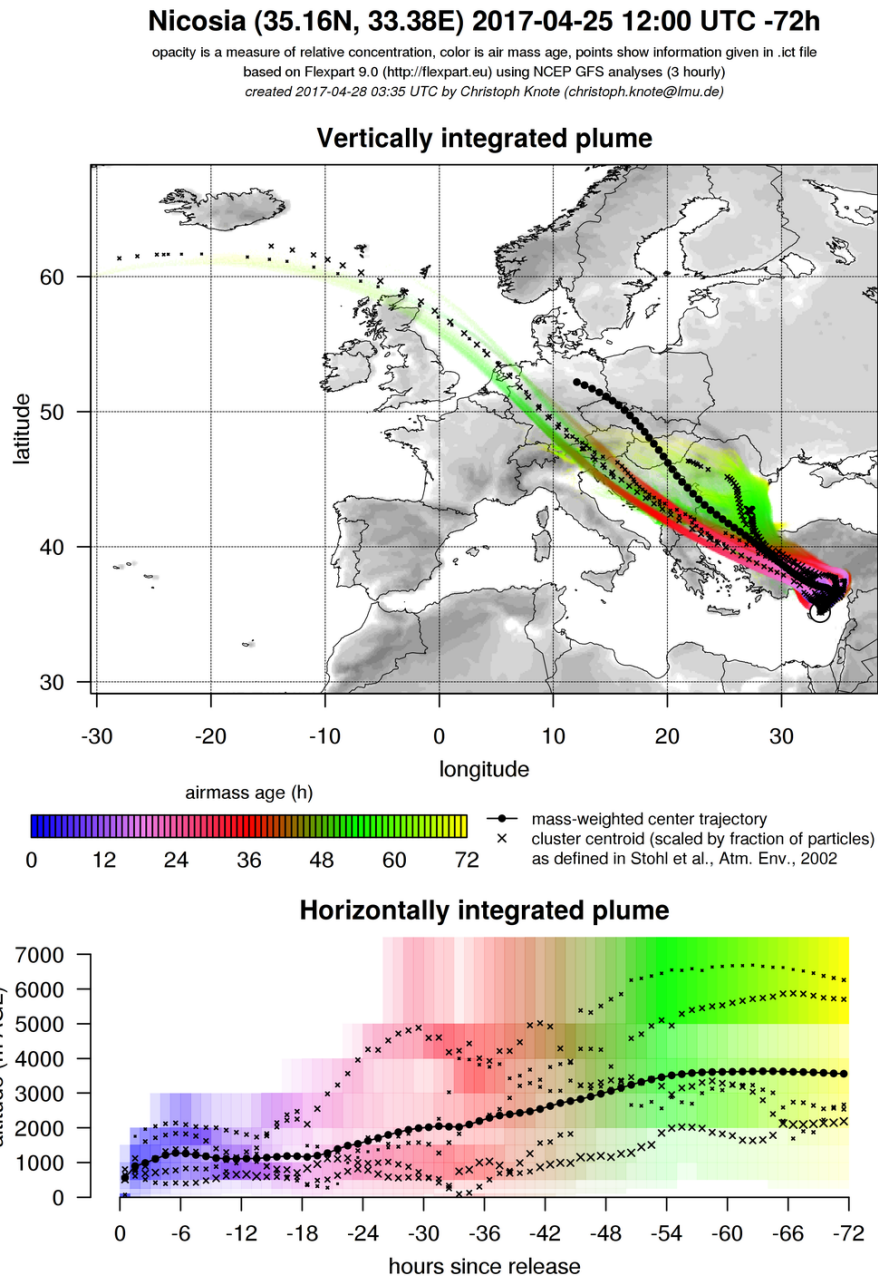
Figure 4.27.: FLEXPART output for 25 April 2017 showing backwards trajectories starting from Nicosia. The trajectories coincide with the forest fires shown in Fig. 4.23.
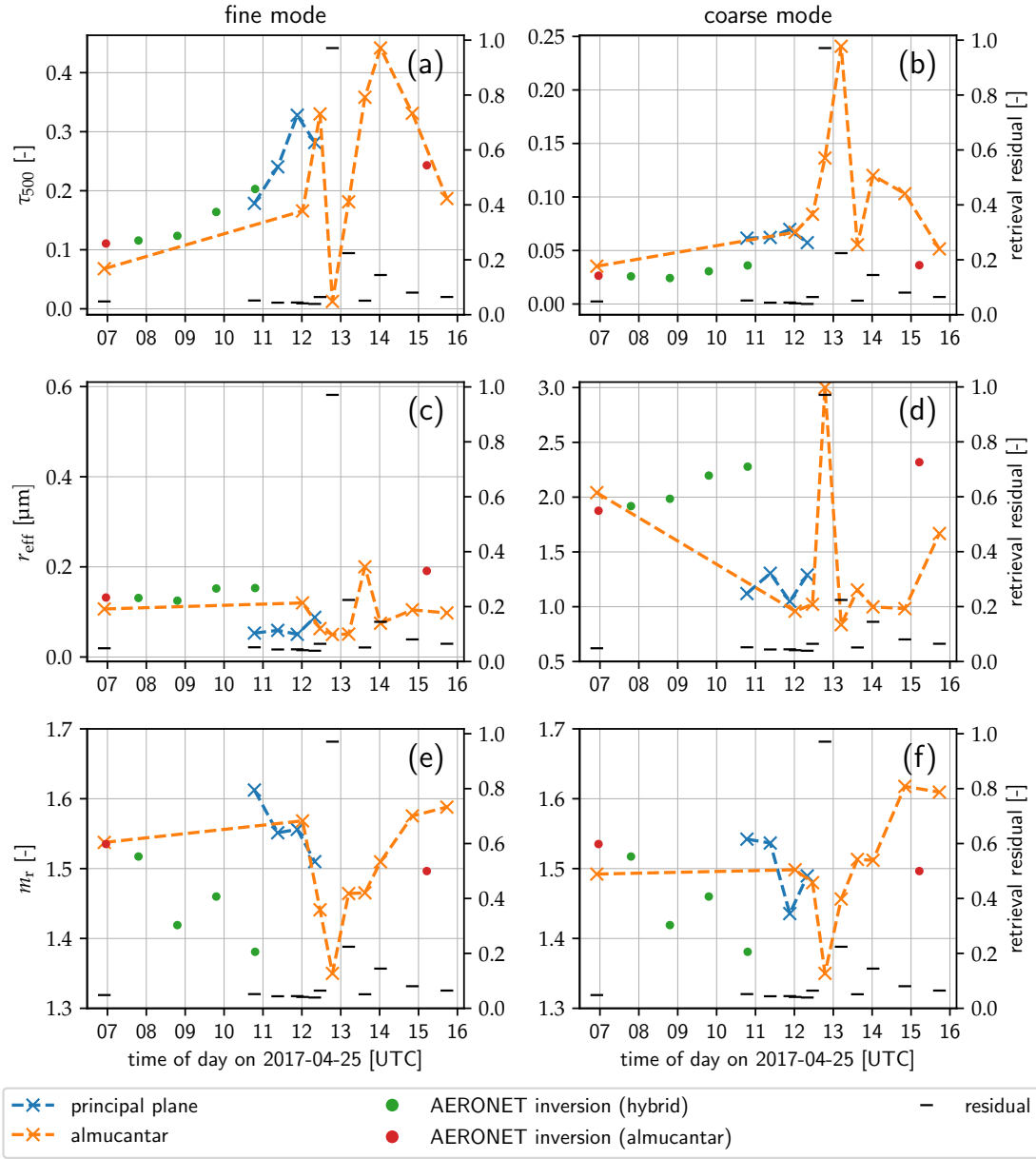
Figure 4.28.: Same as Fig. 4.28, but for 25 April 2017.

5. Discussion

Information on the microphysical and optical aerosol properties in the so–called "twilight zone" could give insight into how clouds form from aerosol and how the aerosol influence their development. The "twilight zone" is the area around clouds that exhibits microphysical and optical modifications by the cloud. However, current retrieval methods for aerosols lavishly screen out measurements near clouds to avoid the problem of 3D radiative effects. Recently, the use of polarimetric information has proven to provide additional information for retrievals (e. g. Fedarenka et al., 2016; Xu and Wang, 2015). While sun photometers like the Cimel CE318-P employed in the AERONET framework are designed for polarized radiometry, no routine retrieval algorithm using these additional measurements is in place.

In this thesis the merits of using polarized multispectral sky radiance measurements for the retrieval of aerosol properties in the vicinity of clouds is investigated. At Meteorological Institute Munich (MIM), the sun and sky scanning radiometer SSARA has been fitted with linear polarizing filters to measure linear polarization at 500 nm.

Summary

To this end, a novel aerosol inversion has been developed in the scope of this thesis, introduced in Section 3.2. It retrieves aerosol properties from polarized multispectral sky radiance measurements, such as those provided – for instance – by the SSARA instrument. The retrieval is amended by a mechanism for screening measurements of cloud sides and bottoms, making it applicable to cloudy situations. The retrieved parameters are the effective particle radius, the real part of the refractive index, and total optical depth for two aerosol modes (fine and coarse mode). The inversion and the cloud screening can use sky radiance measurements from arbitrary scan patterns.

Numerical studies with simulations of principal plane scans in synthetic cloud scans have been performed in Section 4.1. The simulations have been carried out using the 3D Monte–Carlo radiative transfer model MYSTIC and combine different cloud and aerosol situations. These cloud situations include streets of cuboid clouds with 50 m and 1000 m clearing, and four different views from a LES cloud field, as well as a clear sky case for reference. In the first part of these numerical studies, the influence of 3D cloud radiative effects on the radiance and degree of

linear polarization (DoLP) measured in the principal plane scans was investigated. Then, the retrieval is applied to these synthetic principal plane measurements to determine what effects these altered radiances have on the retrieved aerosol properties. The retrieval performance is evaluated for these synthetic cases against proposed values for the required accuracy of the retrieved quantities. Furthermore, the cloud screening was tested on the simulations of the LES cloud field.

In preparing the SSARA instrument for measurements to be used for the retrieval, a new method for the radiometric polarimetric calibration of photometers has been devised (see Section 3.4.1). It simultaneously determines the orientation and the diattenuation of a polarized channel to a high accuracy. Also, a novel quaternion-based correction of the mount skewness introduced in Section 3.4.2 reduces the pointing error of the instrument to below 32 arcmin. The correction can be applied in post-processing, reducing the demands on the accuracy of the setup of the mount. Alternatively, it can be used in real-time during the operation of the instrument, allowing for more precise pointing during cloudy days.

For evaluating the retrieval with real world measurements, it was applied to SSARA measurements from the A-LIFE field campaign that took place in Cyprus in April 2017 in Section 4.2. The SSARA instrument has been calibrated with the aforementioned methods. Three days have been selected for an in–depth analysis. The first case study investigates the retrievals behaviour during partly cloudy conditions. The second day features clear-sky conditions with an arriving Saharan dust layer. The third case captures the arrival of biomass burning aerosol dominated by fine mode. The retrieval results for all the other days are shown in Appendix B.

Conclusions

The calibration of polarization sensitive instruments was an active area of research as "there is still a lack of stable calibration methods and protocols for degree of linear polarization (DoLP) and Stokes vector parameters [. . .]" Li et al. (2018). Previous approaches make assumptions on the quality of the filter (Li et al., 2014, assumes perfect filters), or extrapolate the filter efficiencies leading to diattenuations greater than 1 (Li et al., 2018). The method proposed here closes this gap by providing an experimentally easy and mathematically well–founded solution. Additionally, since diattenuation and orientation of the filters are determined simultaneously, the experimental effort is reduced.

For the calibration of our sun photometer SSARA, the diattenuation of the linear polarizers has been determined to an accuracy of 0.002, their rotation to below 0.1°. Neglecting these filter parameters would introduce a systematic relative error of up to 1.9 % in total radiance and 3.9 % in DoLP across the hemisphere. The accuracy provided is sufficient for sun photometry and the measurement error is

most likely dominated by other instrument errors. This removes another source of error for the work with polarized sky radiance measurements. Since the calibration of SSARA has already been carried out with the equipment used for calibrating the Cimel instruments employed in AERONET, this method could easily be applied to these instruments as well. The same is true for the mount correction. It not only simplifies the tedious task of setting up an instrument on an alt–azimuthal mount, but also improves the pointing accuracy in the presence of clouds when no sun–tracking is possible, thereby making the instrument better suited for "twilight zone" observations. The achieved accuracy of 32 arcmin for SSARA is limited by the resolution of its sun–tracker and could be improved with a more sophisticated one. The high pointing accuracy is especially important for measurements close to the sun, where the radiance falls off quickly. Gasteiger et al. (2011), for instance, shows that measurements in this area carry information about the particle size.

For the retrieval of the aerosol parameters, Mishchenko et al. (2004) established requirements for the accuracy of those parameters. These are 0.04 or 10 % for the aerosol optical depth, and 0.1 μm or 10 % for the effective radius, whichever is larger, respectively. The real part of the refractive index should be known to 0.02 or better.

The results in the retrieval of the synthetic simulations of the cuboid cloud streets with 50 m cloud distance gives a good upper limit on the error in the retrieved parameters, induced by 3D cloud radiative effects. This is necessary to be able to evaluate measurements in the "twilight zone", where these cloud–induced modifications are superimposed with actual modifications of the aerosol due to microphysical processes. Also, the maximum 3D radiative effects induced by clouds can be estimated from this case. Here, the total radiance is enhanced by up to 55 % at scattering angles of about 90° when compared to the cloud–free situation. For the same case, the polarized radiance is underestimated, but only by about 25 %. These cloud–induced enhancements are stronger for larger scattering angles (further away from the sun), due to the prevalence of multiple scattered light. In the forward direction single scattering is dominating, which is not influenced that much by nearby clouds. Therefore, the relative differences are smaller here. As a result, the total AOD is overestimated by roughly 30 % by the retrieval in this cloud case. LES case 3 exhibits similar behaviour, as here the forward scattering peak is obscured by clouds. Remarkably, the effective radius is still retrieved with sufficient accuracy.

All the other investigated scenes yield significantly better results. The retrieval results of the 1000 m clearing cube cloud are comparable to those of LES cases 1, 2, and 4. The cloud screening reliably removed all measurements of cloud sides and bottoms in the LES cases. AOD and fine mode effective radius are retrieved to within the required accuracy. This holds true, even for the problematic LES case 3.

The effective radius of the coarse mode is significantly underestimated in all cases for large particles (towards effective radii of 2 μm). Modifications of the effective radius due to the presence of clouds observed by some studies (e.g. Várnai et al., 2017) are not observable here. The refractive index is overestimated and cannot be reproduced with sufficient accuracy in cloudy situations. The information in the coarse mode is always a bit less accurate, possibly due to the problem with large coarse mode aerosols.

In the case studies performed with A-LIFE data, the retrieval results differ depending on the scan pattern used on both days. The reason for this is not fully understood. The first case study investigates the retrievals behaviour under partly cloudy conditions. An increase in AOD is visible around the time of convective activity. This effect has been shown to exist due to 3D radiative effects close to clouds in previous numerical studies. The second day selected features clear-sky conditions with an arriving Saharan dust layer. This layer can be observed by an increase in coarse mode AOD retrieved from SSARA measurements, as well as in AERONET inversion data. A third case captures the arrival of fine mode dominated biomass burning aerosol. The corresponding increase in fine mode AOD is well represented in the retrieval results. With a few exceptions, the retrieval shows the tendency to overestimate the AOD when compared to values obtained from direct sun observations. The error sometimes exceeds 0.1 in total AOD. The retrieval of the effective radius works reasonably well for the fine mode. In all cases, the value is too low but agrees with AERONET to within 0.1 μm. However, oftentimes the retrieval reaches the lower limit of 0.05 μm, possibly inducing errors in other parameters. In the coarse mode, the inversion compares well to AERONET for values around 1.5 μm. For larger particles (towards effective radii of 2 μm), the retrieval produces smaller radii than AERONET. There appears to be a systematic increase in the retrieved effective radius for both modes in the morning and evening. To properly evaluate these results and resolve the remaining discrepancies, independent measurements are required. The same is true for the retrieval of index of refraction, especially due to the fact that AERONET uses a common value for both modes. In some cases, the results are well supported by AERONET. However, it often stays close to its prior, which could indicate lacking sensitivity to that parameter.

This work provides another step towards remote sensing of aerosols, especially in cloudy situations. The numerical studies show that the polarized sky radiance is less influenced by clouds than the unpolarized one. Upper limits on the enhancements by 3D cloud radiative effects have been established. These are required as they could be interpreted as modifications of the microphysical and optical properties of the aerosol. An algorithm now exists that can be employed on sky polarization and radiance measurements taken in arbitrary scan pattern and wavelength combi-

nations. Apart from that, the method was developed completely independent from AERONET considerations, giving the opportunity for meaningful intercomparison.

Outlook

The remaining differences in the retrieved parameters between the method presented here and the AERONET inversion have to be examined further. As a first step, the results from A-LIFE should be compared to measurements obtained from independent instruments, such as lidar or in situ. This should also extend to times where no AERONET results are available for comparison. With that, it should be possible to determine whether the difference are actually retrieval uncertainties or are also present is other measurements. Additionally, the uncertainty of the retrieval could be determined by a perturbation approach. If the differences are indeed errors, their source has to be determined. They could either be caused by measurement errors or by systematic effects produced by the retrieval algorithm. To this end, the inversion scheme should be applied to measurements from other sky radiometers, such as the Cimel CE318-DP used in AERONET. This is to rule out instrument effects, such as non–linearities in the amplifiers or detectors. Even though the instrument baffle reduces a large amount of straylight, there are still errors remaining, as can be seen in the non–zero DoLP in measurements close to the sun. Here it is again useful that the accuracy of the polarization calibration is high enough to discard it as a possible source of error. Furthermore, the retrieval could be evaluated using multiple polarized wavelength measurements. Vice versa, our measurements might be analyzed using different inversion algorithms. This way systematic errors in the retrieval method can be identified.

So far, only principal plane scans at a solar zenith angle of 30° have been investigated with the numerical studies in the synthetic cloud fields. Further studies with different zenith angles and scan patterns should be performed to explain the differences in the quantities retrieved from principal plane and almucantar scans.

Additionally, more studies of the retrieval could be performed. Eventually, the inaccuracies could be reduced by including sky radiance measurements in the 1020 nm channel, extending the information to the near–infrared spectral range. Also the set of retrieved aerosol properties can be changed. So far, the variance (width) of the particle size distribution, imaginary part of the refractive index and fraction of spherical particles are fixed. If this value is wrong, the retrieval tries to reproduce the measurements by modifying the other parameters, likely to false values. Furthermore, assumptions on the atmospheric composition (such as CO_2 and O_3 concentration) and the height of aerosol layers have been fixed in these studies.

One approach would be to simultaneously retrieve all these values. However, the information content of the measurements most likely does not have enough

information to reliably retrieve additional degrees of freedom. Another possibility for improvement could be to use information from direct sun measurements or other instruments to improve the choice of the fixed values. For instance, the Ångström exponent can be used to determine the presence of dust. Accordingly, the fraction of spherical particles in the coarse mode can be assumed lower, compared to other aerosol types. Similarly, for biomass burning aerosols, the imaginary part of the refractive index can be expected to be higher than average. With this, a "preselection" of the fixed retrieval values is possible. Layer height information from lidar could be used to better represent their position in the forward model and improve the retrieval results, as has been done in Gasteiger et al. (2011). While it would also be possible to add the total AOD obtained from direct sun observations as a constraint to the retrieval, this approach might limit the applicability to cloudy situations, when no such measurements are available or the value changes rapidly. For clear sky cases this constraint would certainly improve the retrieval results though.

Including other measurements as "hard" constraints that cannot be violated in the minimalization of the inversion can be done easily in the current version of the retrieval. However, these additional measurements are also subject to errors and uncertainties. To accommodate this, the retrieval is best switched to using optimal estimation methods (see Rodgers, 2000). Another upshot of this would be the possibility of estimating the uncertainty of the results.

A. Introduction to quaternions

Quaternions are an extension to complex numbers. As complex numbers can be used to describe operations – such as rotation – in 2D space (in polar notation), the same is true for quaternions in 3D space (see Horn, 1987). A quaternion is described by four real components,

$$\mathbf{q} = q_0 + iq_1 + jq_2 + kq_3 \,, \tag{A.1}$$

where i, j, and k are the imaginary units with the following identities,

$$i^2 = j^2 = k^2 = -1 \,,$$
$$ij = -ij = k \,, \quad jk = -kj = i \,, \quad ki = -ik = j \,. \tag{A.2}$$

Quaternions form a non–Ablian group under multiplication defined by the *Hamilton product*. Therefore, quaternions do not commute under the Hamilton product. It can be derived using the distributive and associative laws, and the identities in Eqs. (A.2).

$$\mathbf{qu} = (q_0 + iq_1 + jq_2 + kq_3)\,(u_0 + iu_1 + ju_2 + ku_3) \tag{A.3}$$
$$= + q_0u_0 + iq_0u_1 + ju_0q_2 + ku_0q_3$$
$$- q_1u_1 + iq_1u_0 - ju_1q_3 + ku_1q_2$$
$$- q_2u_2 + iq_2u_3 + ju_2q_0 - ku_2q_1$$
$$- q_3u_3 - iq_3u_2 + ju_3q_1 + ku_3q_0 \tag{A.4}$$

Additionally, a dot product is defined as

$$\mathbf{q} \cdot \mathbf{u} = q_0u_0 + q_1u_1 + q_2u_2 + q_3u_3 \,. \tag{A.5}$$

It can be used to induce a norm $\|\mathbf{q}\| = \sqrt{\mathbf{q} \cdot \mathbf{q}}$. A quaternion is conjugated by inverting the sign of its imaginary components,

$$\mathbf{q}^* = q_0 - iq_1 - jq_2 - kq_3 \,. \tag{A.6}$$

It can be shown that the multiplicative inverse is

$$\mathbf{q}^{-1} = \frac{1}{\mathbf{q} \cdot \mathbf{q}}\mathbf{q}^* = \frac{1}{\|\mathbf{q}\|^2}\mathbf{q}^* \tag{A.7}$$

As a result, for normed quaternions ($\|\mathbf{q}\| = 1$), its inverse is its conjugate.

Quaternions describing spatial rotations in three-dimensional space have to be normed. A rotation about an axis $\mathbf{a}$ through an angle α is represented by the quaternion

$$\mathbf{q}\left(\alpha, \vec{a}\right) = \cos\frac{\alpha}{2} + \sin\frac{\alpha}{2} \cdot \left(a_x i + a_y j + a_z k\right) . \tag{A.8}$$

It can easily be seen, that the conjugate is in fact the inverse, corresponding to a rotation by the negative angle or around the negative axis. According to Euler's rotation theorem, the conjunction of several rotations can be described by a single rotation. This also follows from the group properties of quaternions. The Hamilton product of two normed quaternions is again a normed quaternion, representing a rotation.

A regular 3D Eucledian vector $\vec{r}$ can be described by a quaternion with a real part of 0 (*pure* quaternion). The rotation by a quaternion is calculated as

$$\mathbf{r}' = \mathbf{q}\mathbf{r}\mathbf{q}^{-1} = \mathbf{q}\mathbf{r}\mathbf{q}^* \tag{A.9}$$

The resulting quaternion is again pure, and the rotated vector can be reconstructed. Also, unit quaternions can be transformed into a rotation matrix that can be applied to regular Euclidean vectors. For a unit quaternion q, the Euler angles of the corresponding rotation and the 3×3 rotation matrix $\widehat{\mathbf{M}}_\mathrm{q}$ are given by

$$\vec{r}' = \widehat{\mathbf{M}}_\mathrm{q} \cdot \vec{r} \tag{A.10}$$

$$= \begin{pmatrix} 1 - 2\left(q_2^2 + q_3^2\right) & 2\left(q_1 q_2 - q_0 q_3\right) & 2\left(q_1 q_3 + q_0 q_2\right) \\ 2\left(q_2 q_1 + q_0 q_3\right) & 1 - 2\left(q_1^2 + q_3^2\right) & 2\left(q_2 q_3 - q_0 q_1\right) \\ 2\left(q_3 q_1 - q_0 q_2\right) & 2\left(q_3 q_2 + q_0 q_1\right) & 1 - 2\left(q_1^2 + q_2^2\right) \end{pmatrix} \cdot \vec{r} \tag{A.11}$$

B. Retrieval results for the remaining A-LIFE days

In this appendix, the results of the retrieval for the all other days of the A-LIFE campaign are presented, where measurements have been performed.
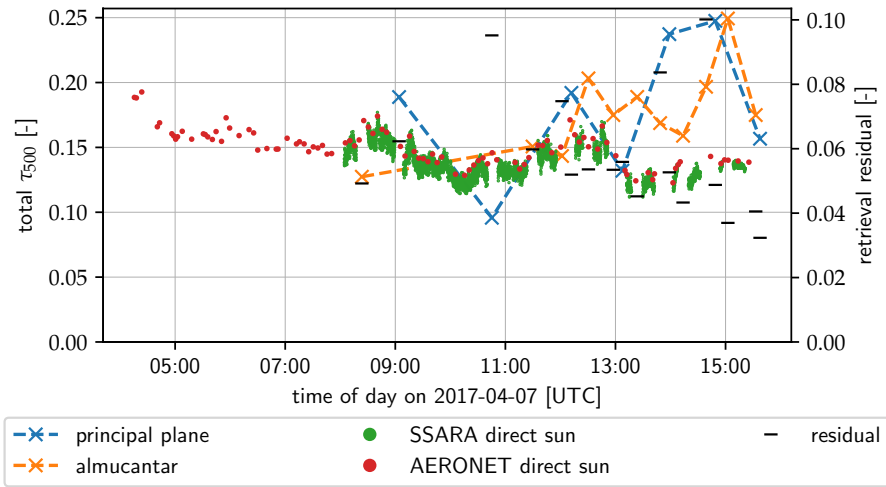
(a) Retrieved total AOD for 7 April 2017. For description see Fig. 4.17.
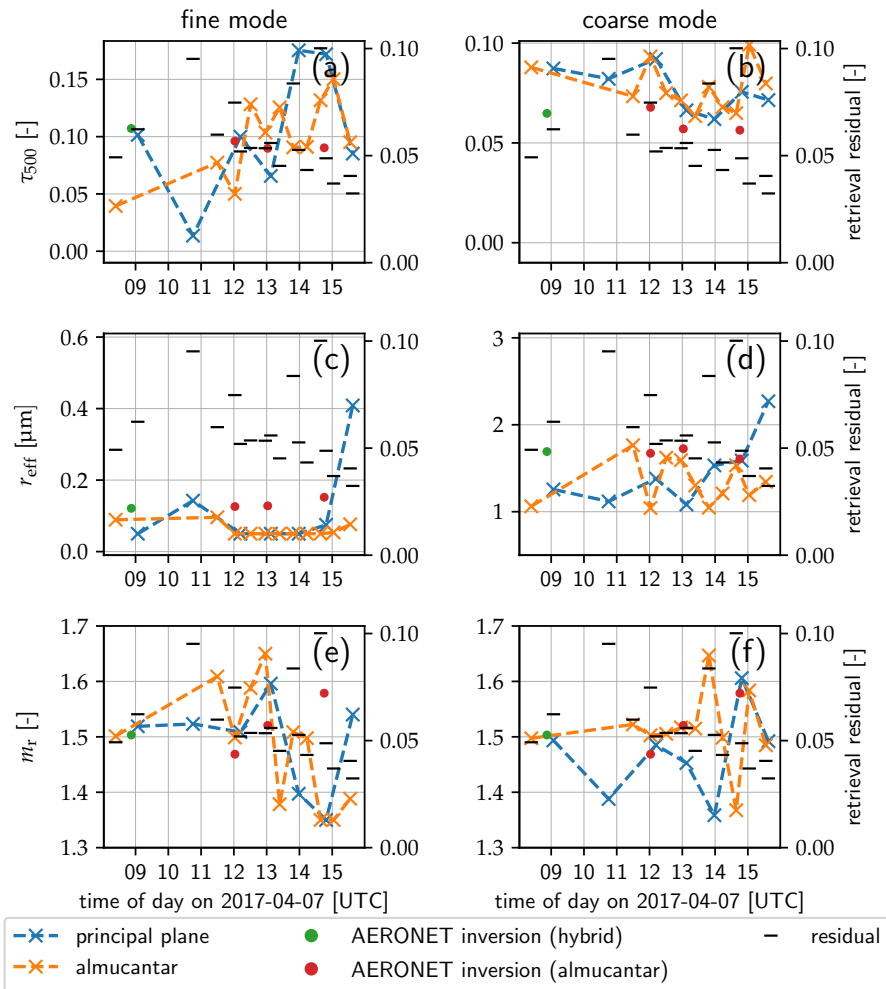
(b) Retrieved aerosol parameters for 7 April 2017. For description see Fig. 4.18.
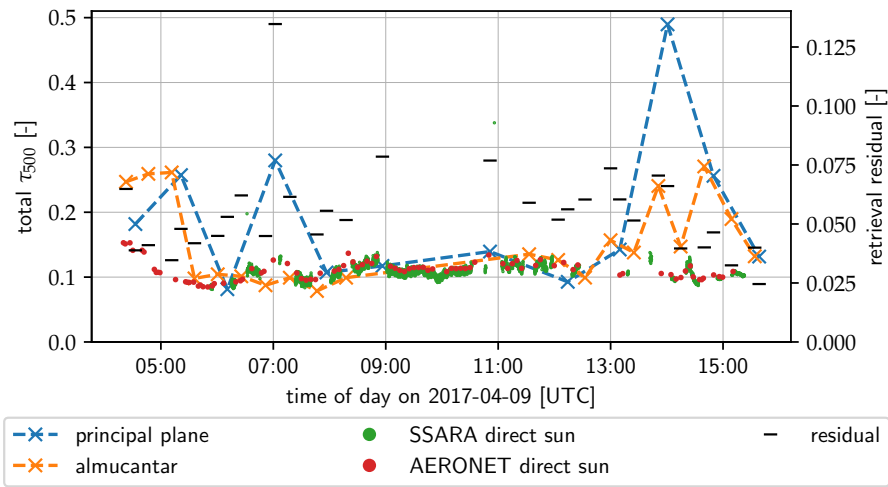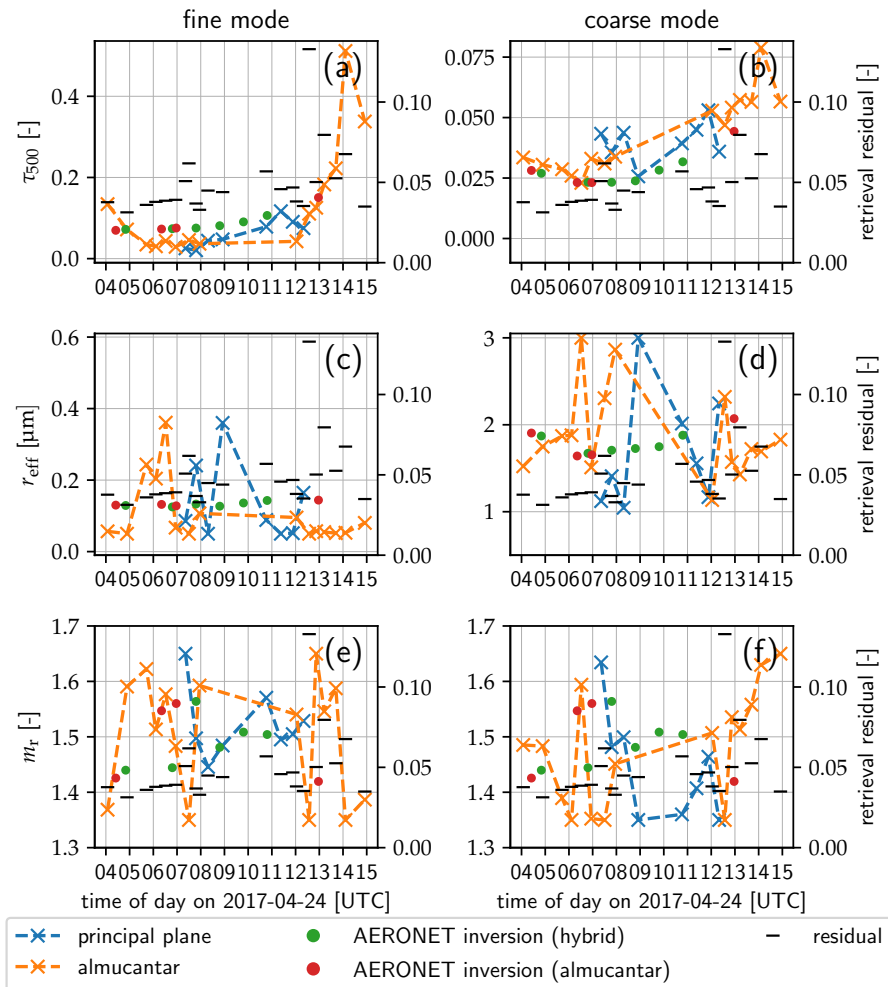
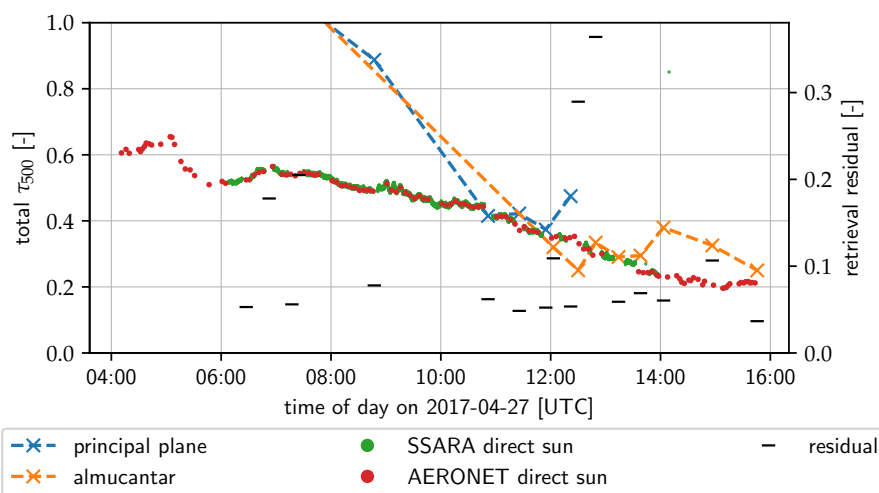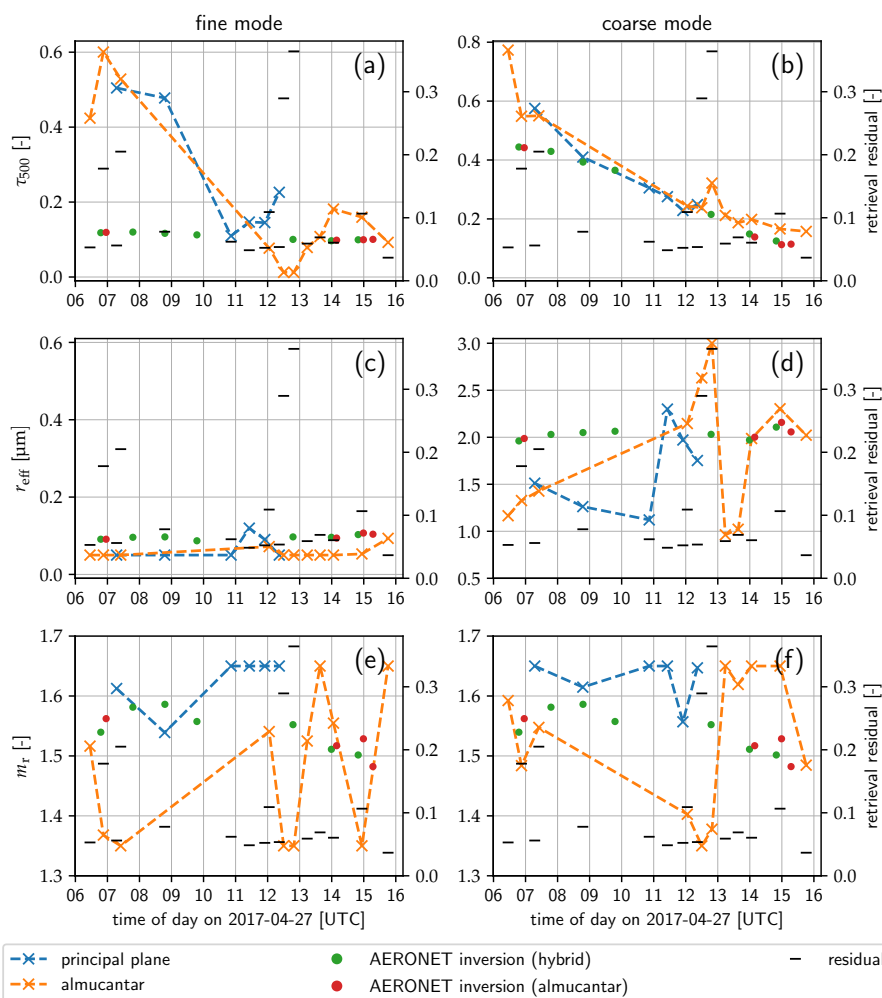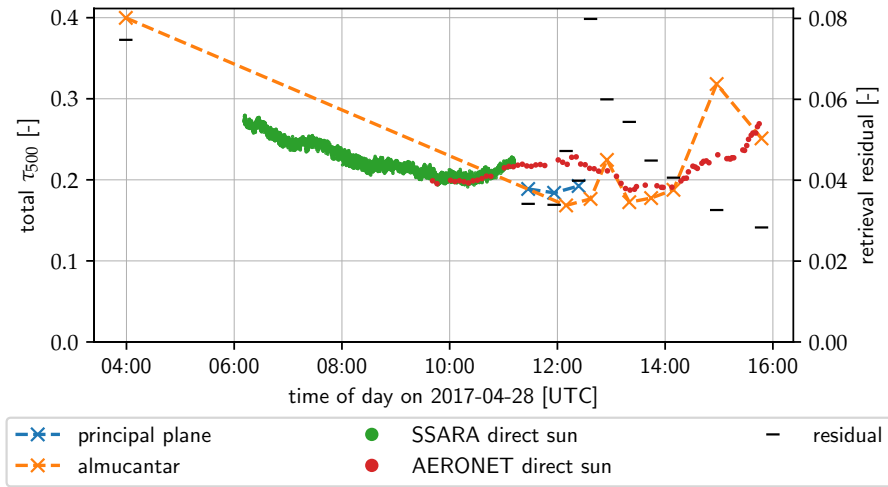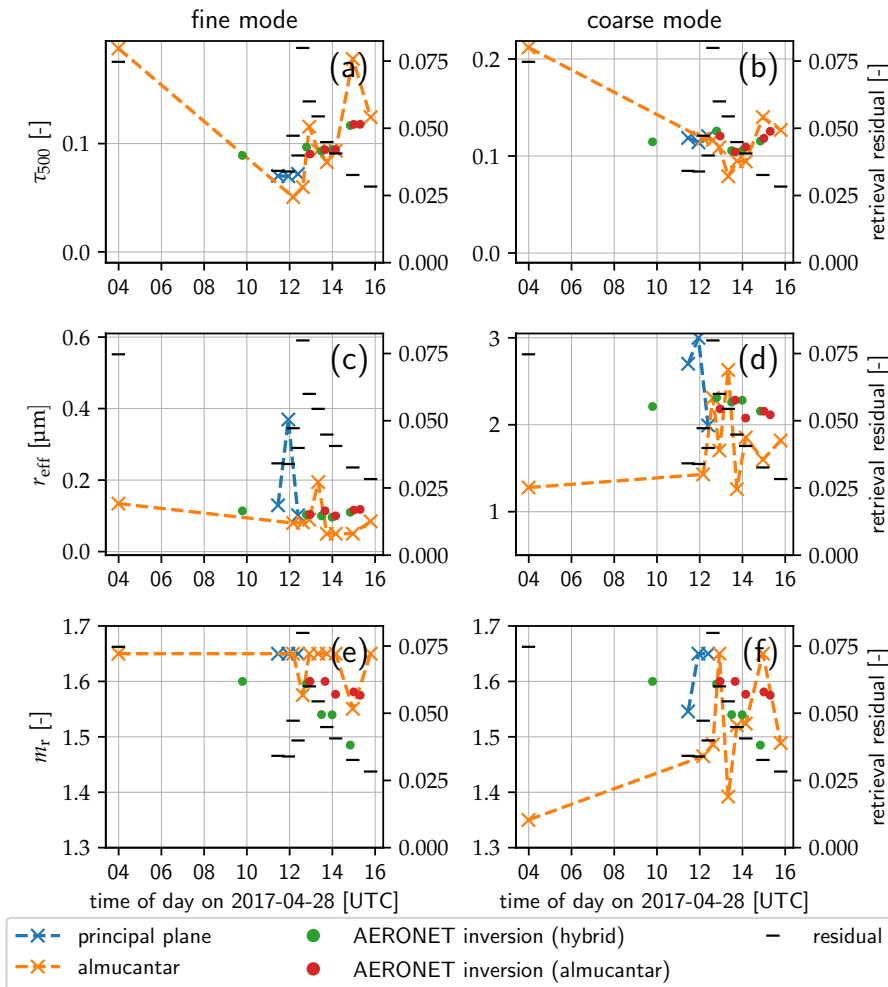(a) Retrieved total AOD for 9 April 2017. For description see Fig. 4.17.
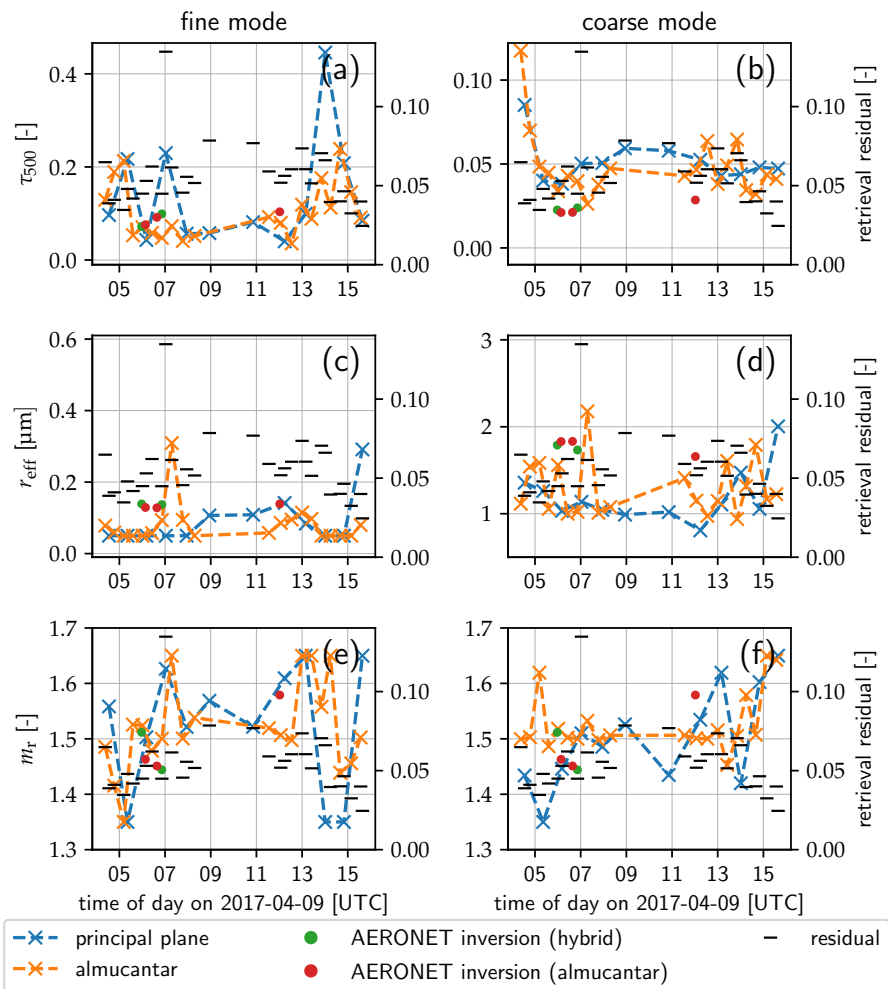
(b) Retrieved aerosol parameters for 9 April 2017. For description see Fig. 4.18.
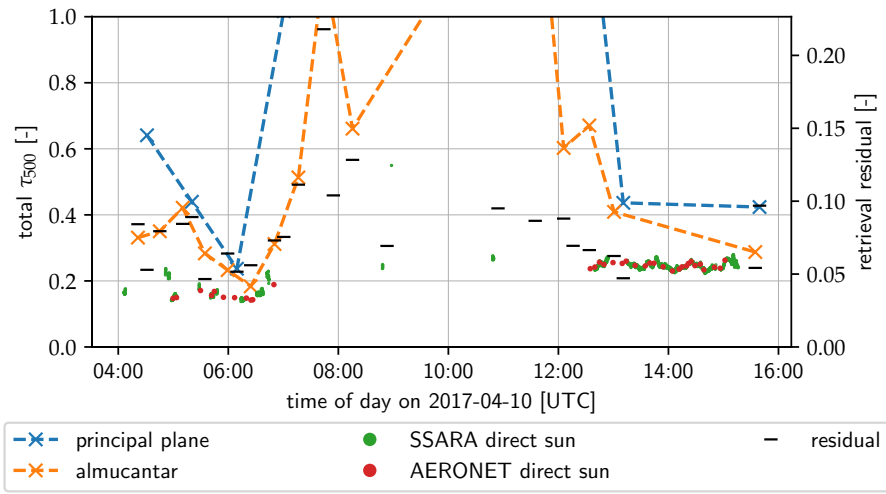
(a) Retrieved total AOD for 10 April 2017. For description see Fig. 4.17.
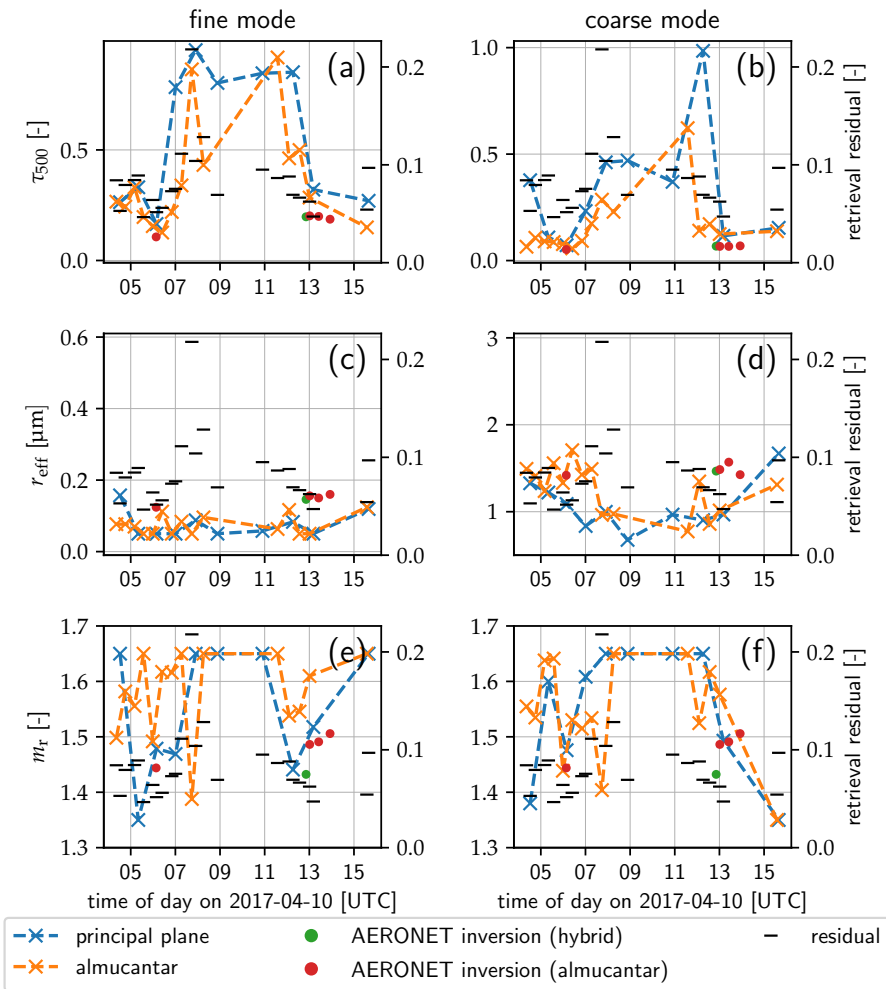
(b) Retrieved aerosol parameters for 10 April 2017. For description see Fig. 4.18.
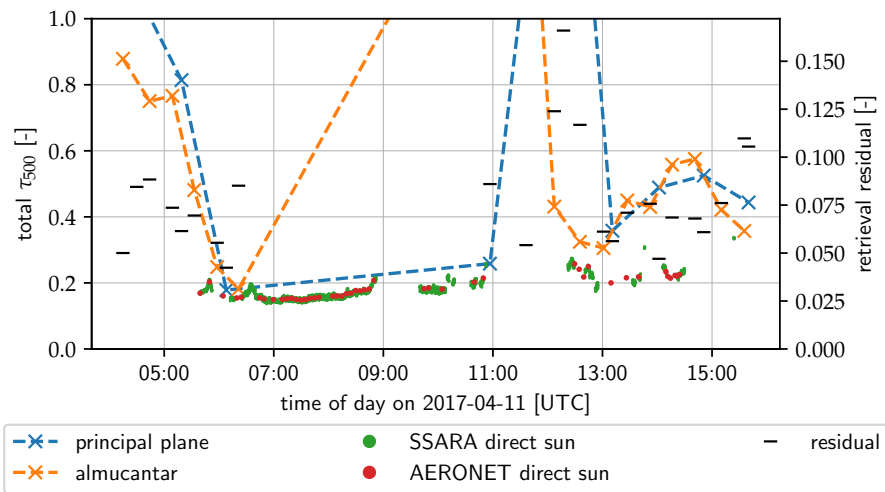
(a) Retrieved total AOD for 11 April 2017. For description see Fig. 4.17.
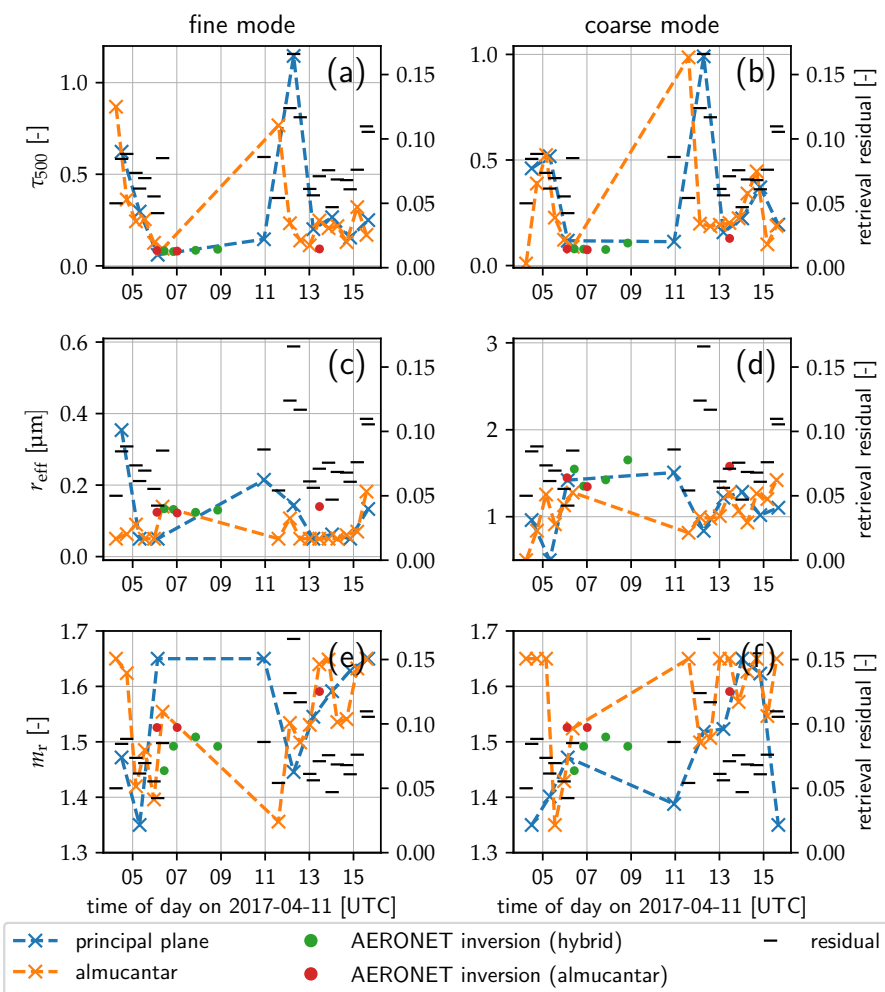
(b) Retrieved aerosol parameters for 11 April 2017. For description see Fig. 4.18.
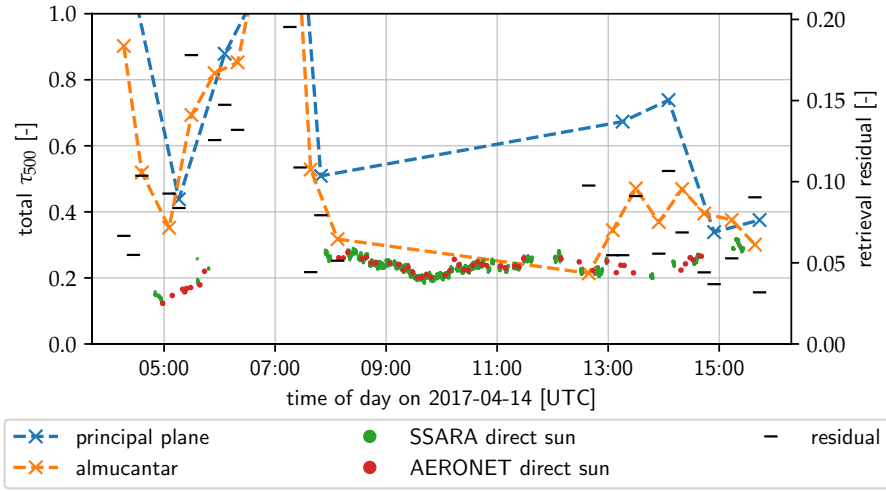
(a) Retrieved total AOD for 14 April 2017. For description see Fig. 4.17.
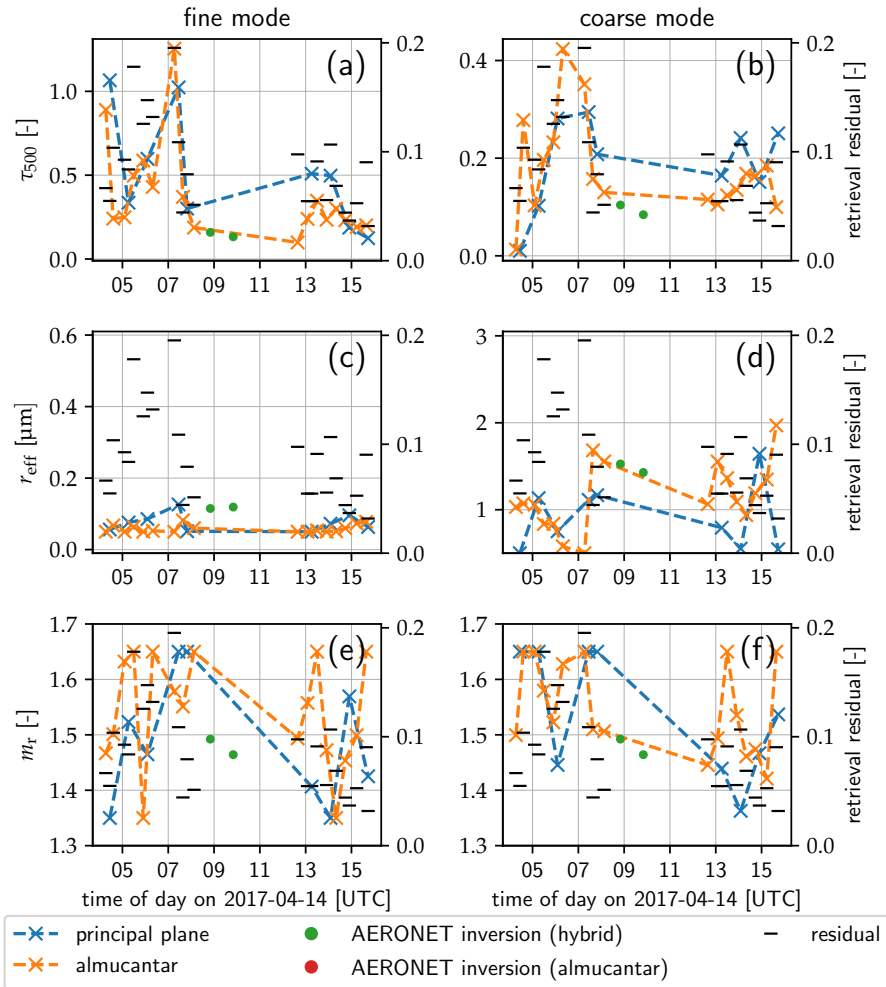
(b) Retrieved aerosol parameters for 14 April 2017. For description see Fig. 4.18.
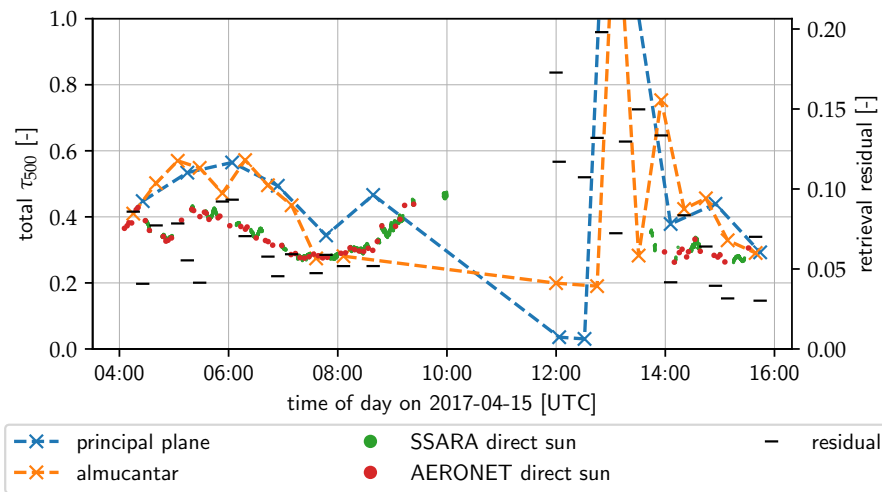
(a) Retrieved total AOD for 15 April 2017. For description see Fig. 4.17.
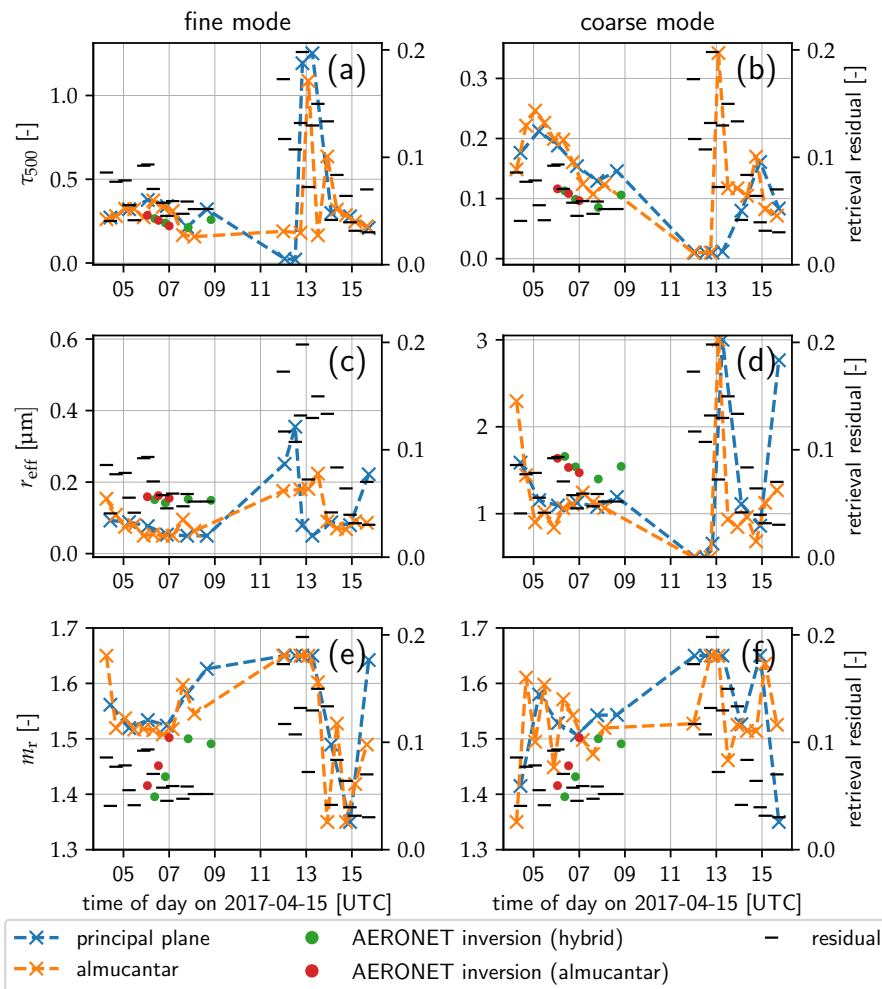
(b) Retrieved aerosol parameters for 15 April 2017. For description see Fig. 4.18.
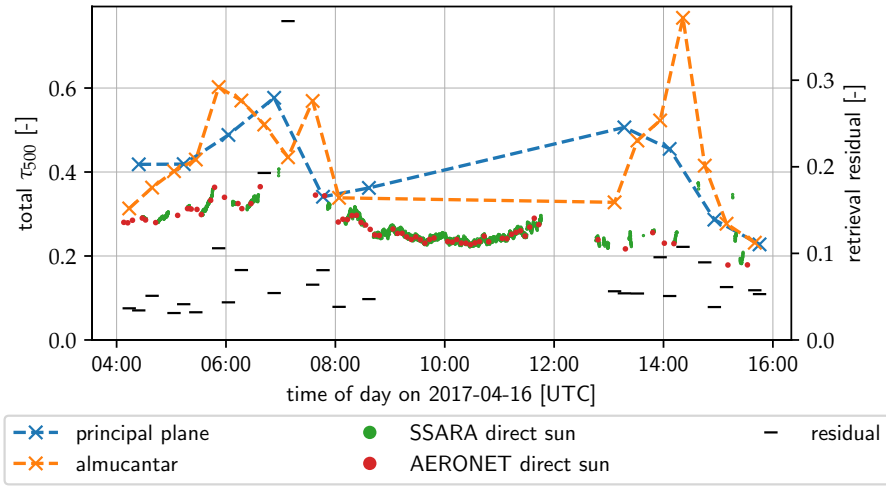
(a) Retrieved total AOD for 16 April 2017. For description see Fig. 4.17.
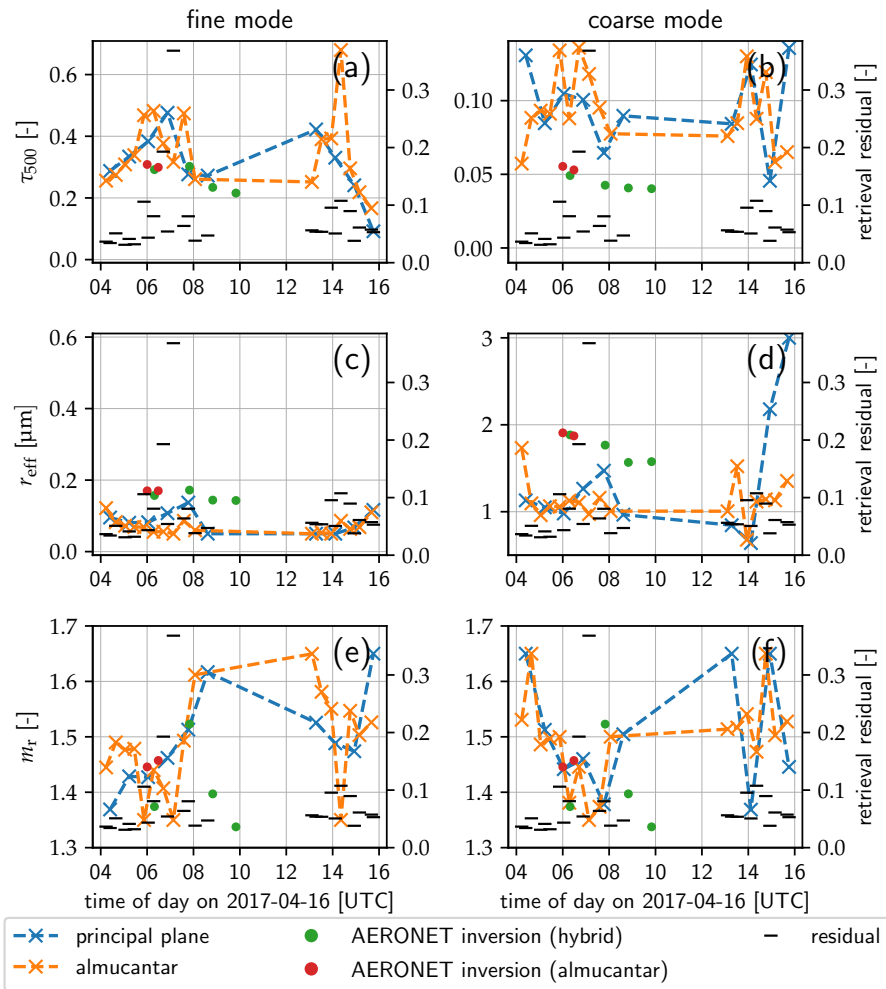
(b) Retrieved aerosol parameters for 16 April 2017. For description see Fig. 4.18.
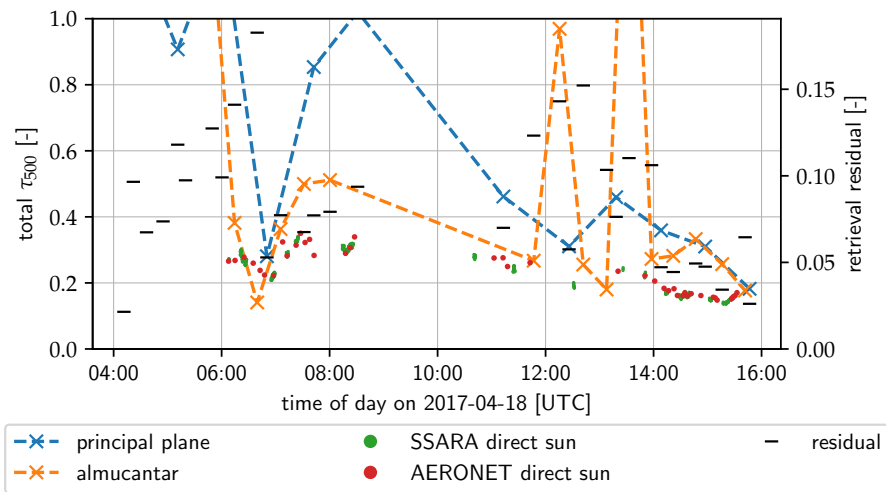
(a) Retrieved total AOD for 18 April 2017. For description see Fig. 4.17.
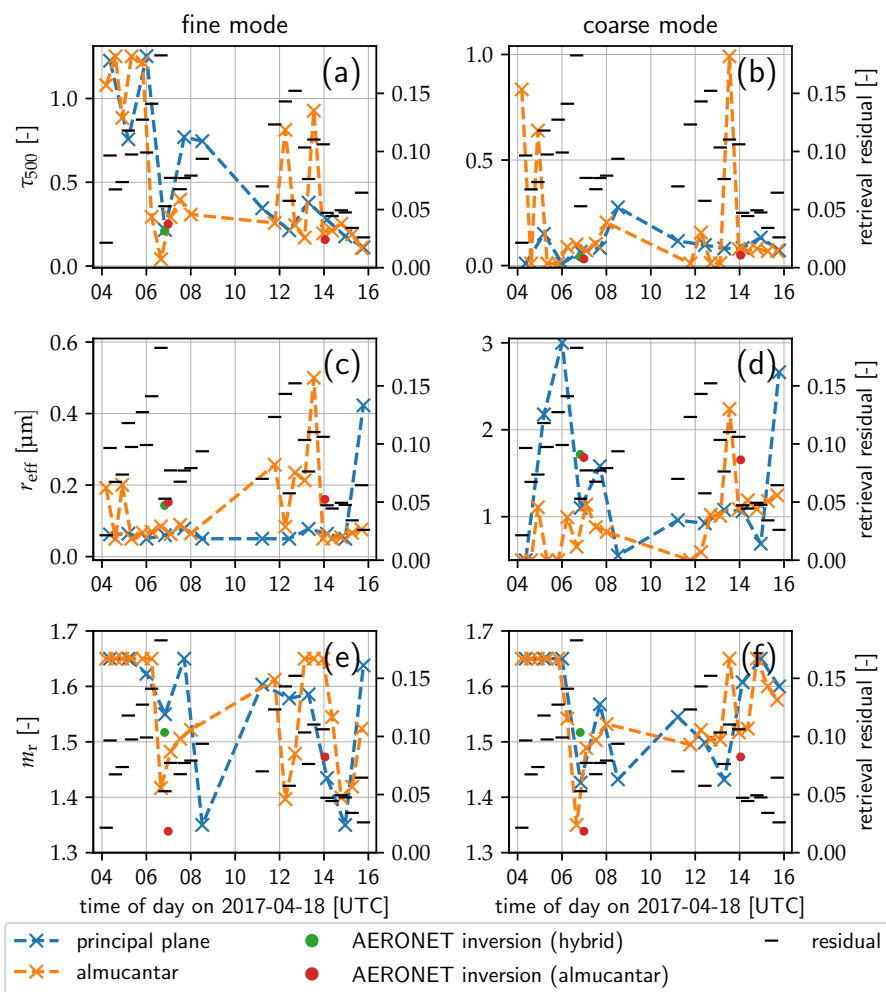
(b) Retrieved aerosol parameters for 18 April 2017. For description see Fig. 4.18.
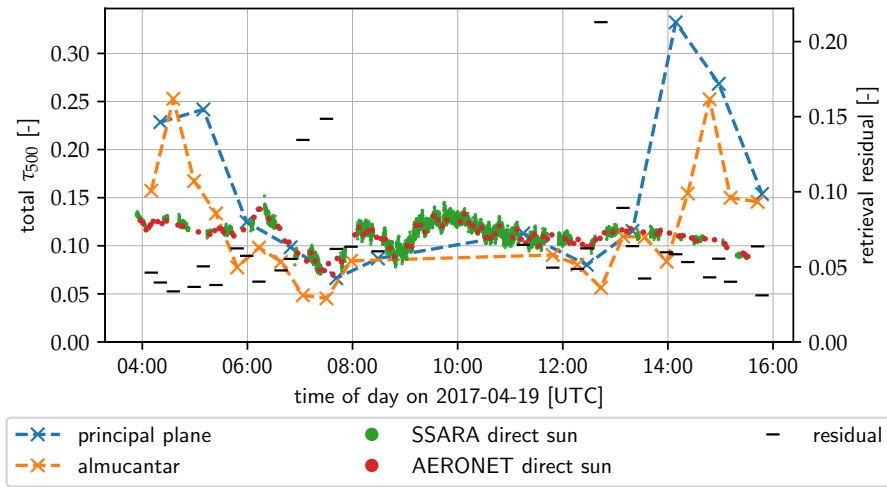
(a) Retrieved total AOD for 19 April 2017. For description see Fig. 4.17.
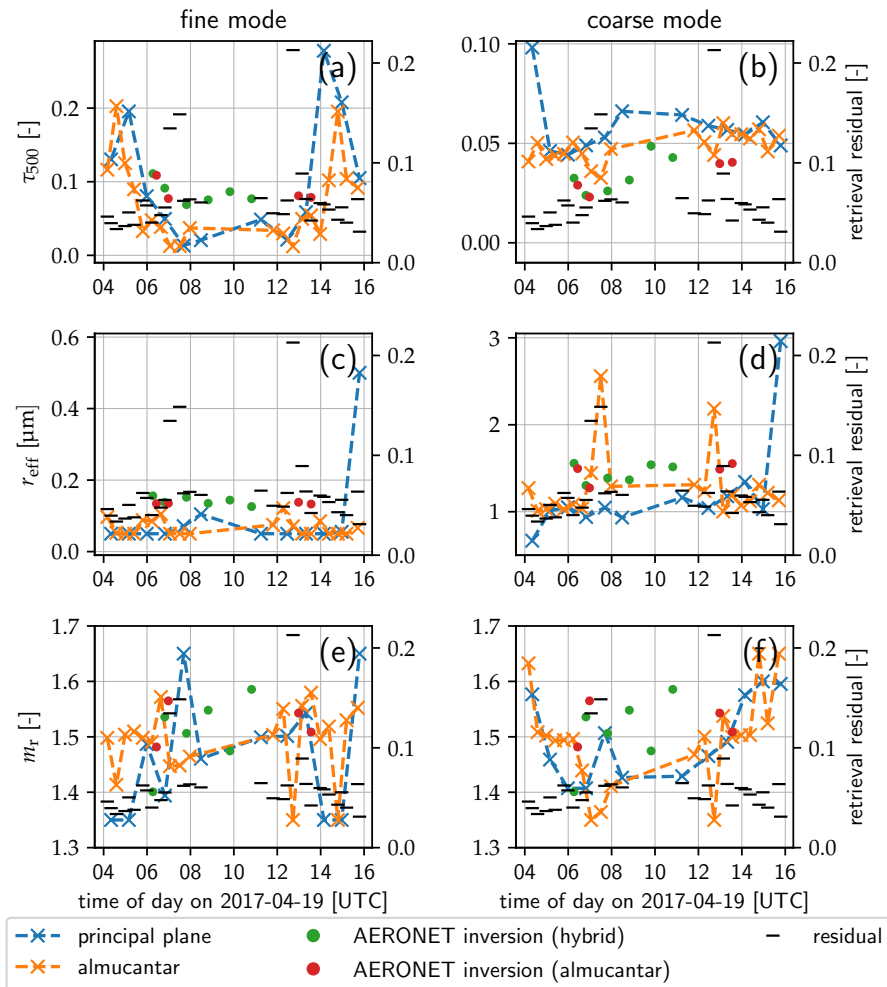
(b) Retrieved aerosol parameters for 19 April 2017. For description see Fig. 4.18.
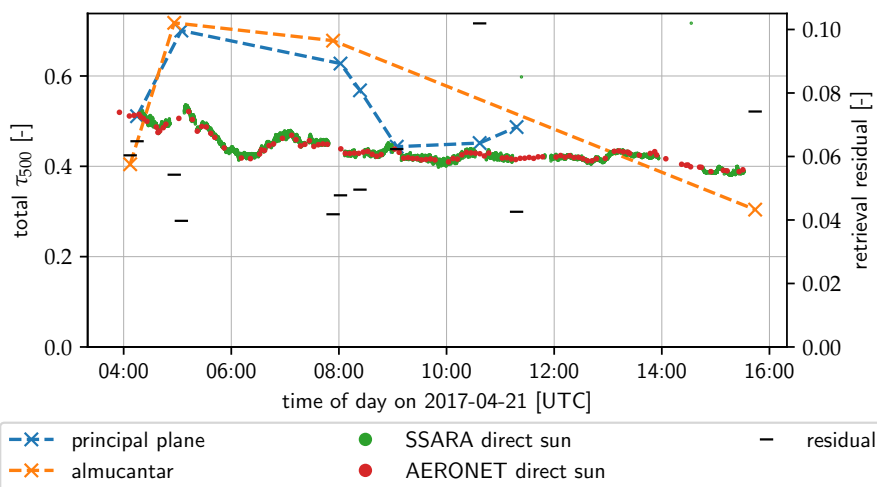
(a) Retrieved total AOD for 21 April 2017. For description see Fig. 4.17.
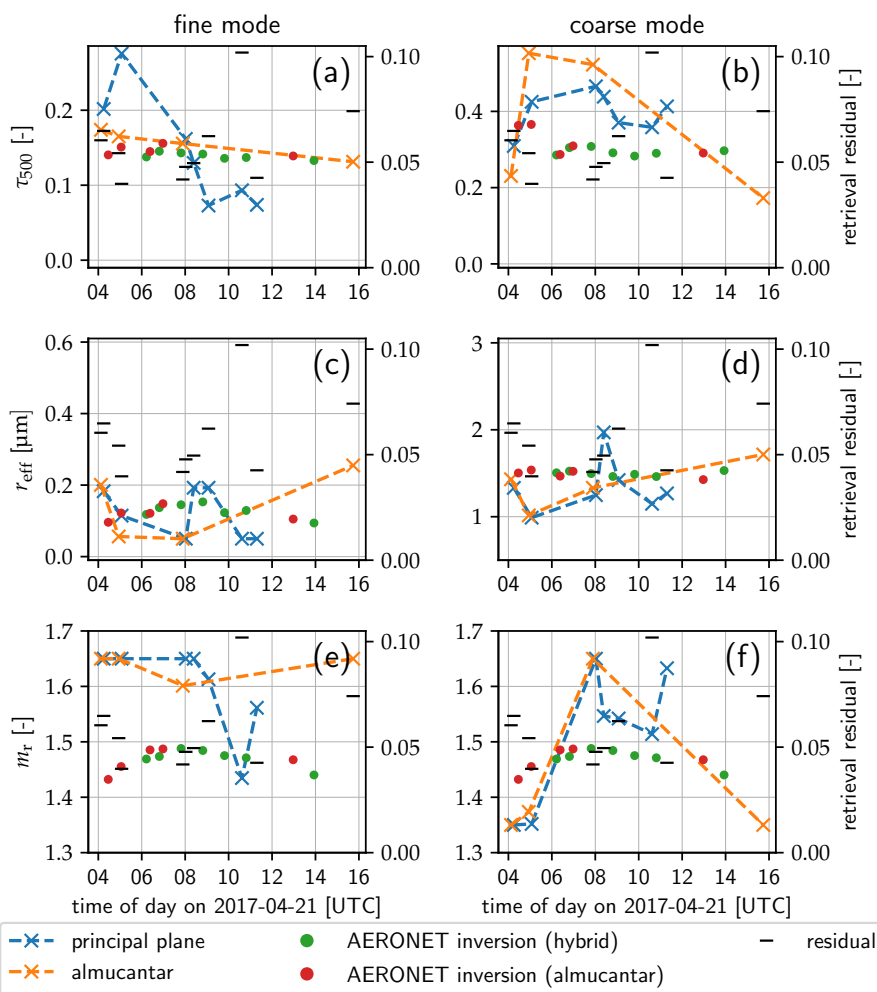
(b) Retrieved aerosol parameters for 21 April 2017. For description see Fig. 4.18.
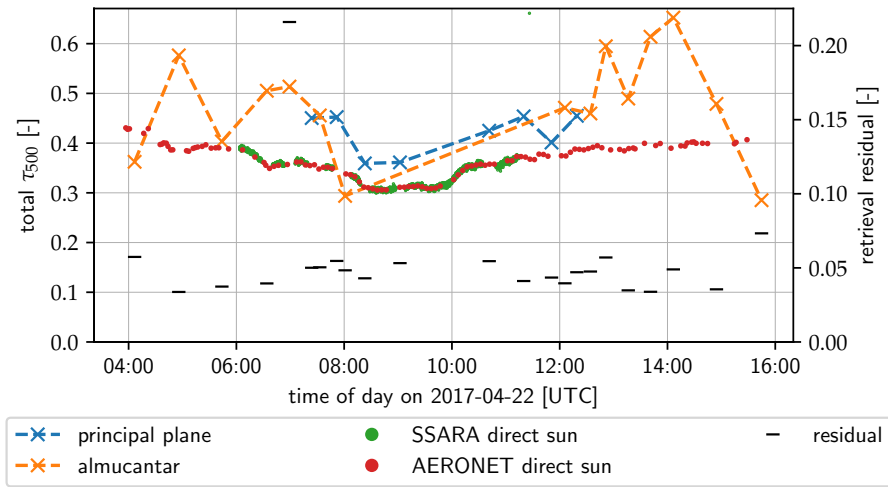
(a) Retrieved total AOD for 22 April 2017. For description see Fig. 4.17.
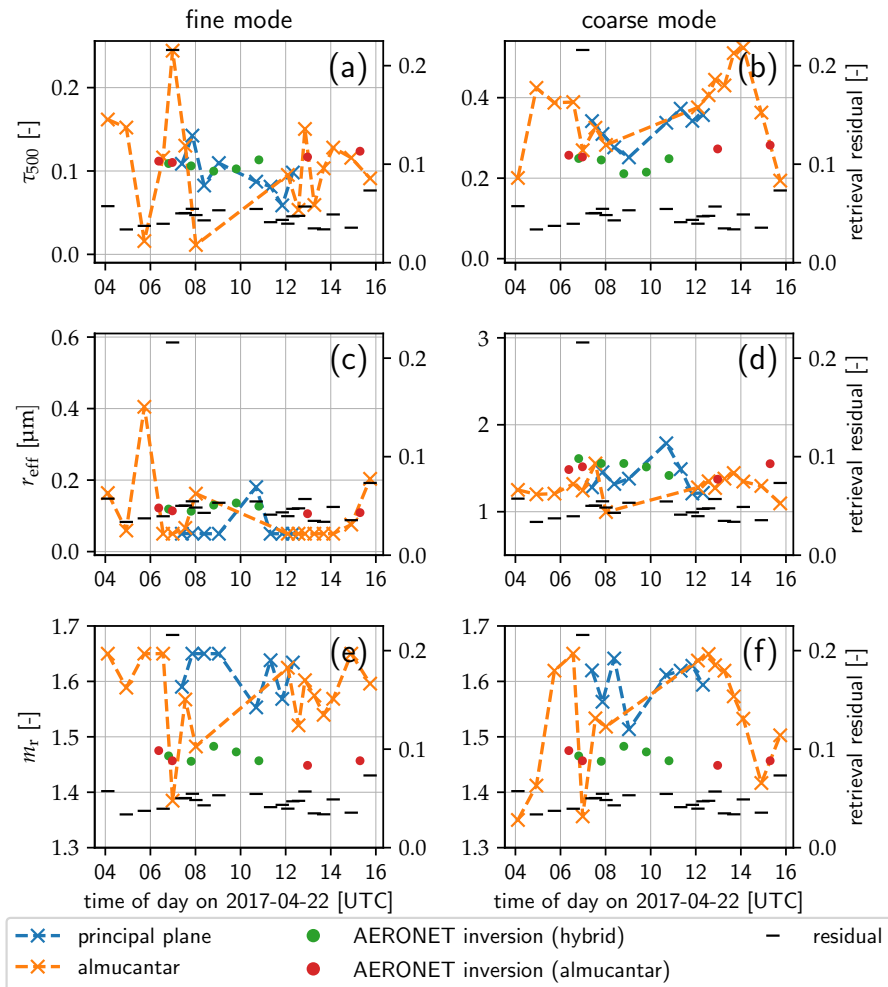
(b) Retrieved aerosol parameters for 22 April 2017. For description see Fig. 4.18.
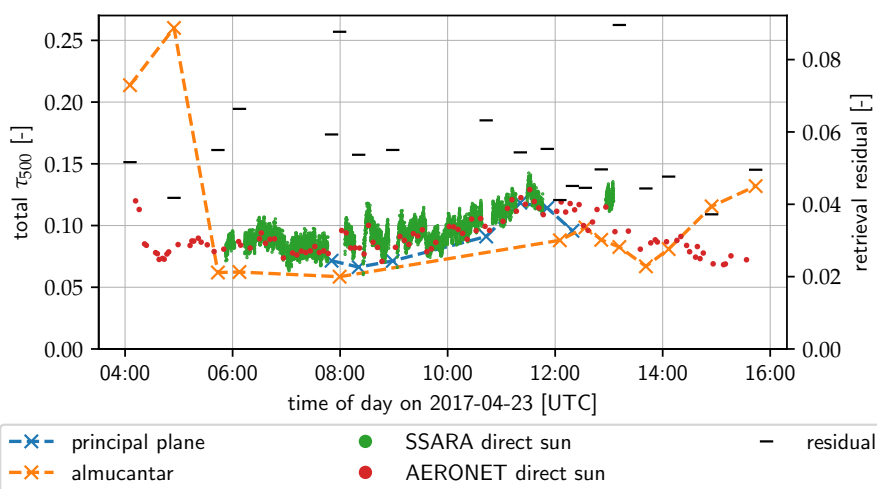
(a) Retrieved total AOD for 23 April 2017. For description see Fig. 4.17.
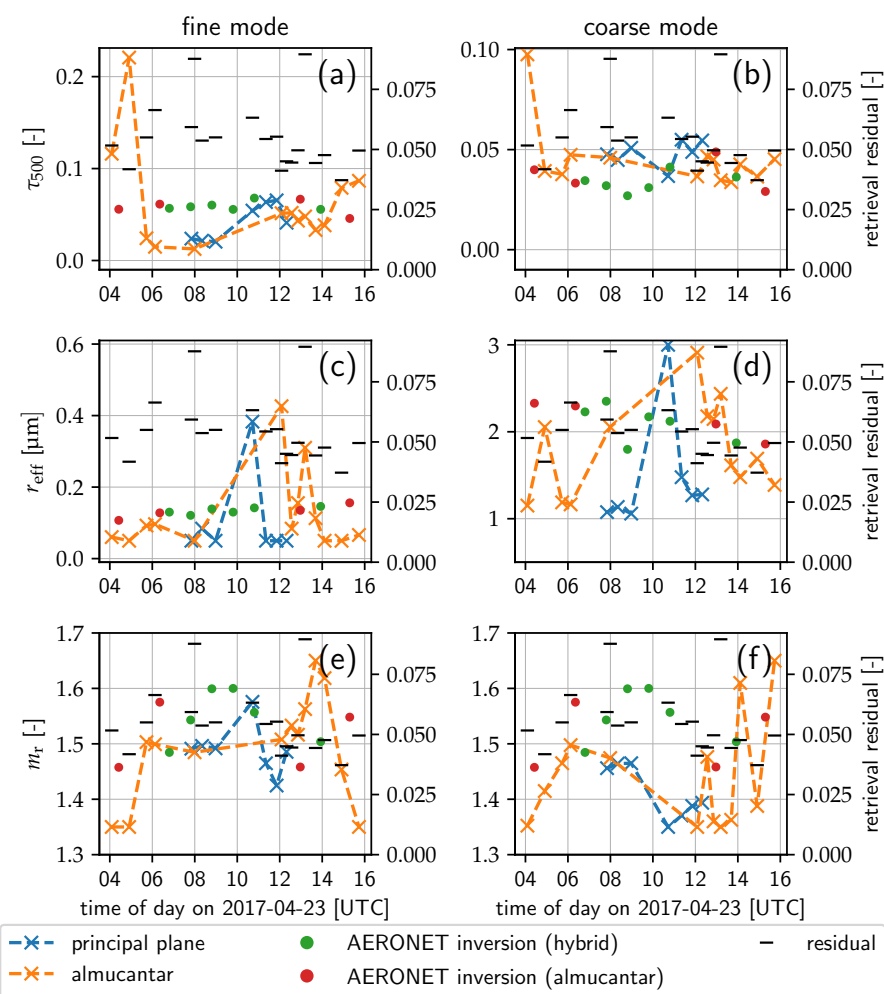
(b) Retrieved aerosol parameters for 23 April 2017. For description see Fig. 4.18.
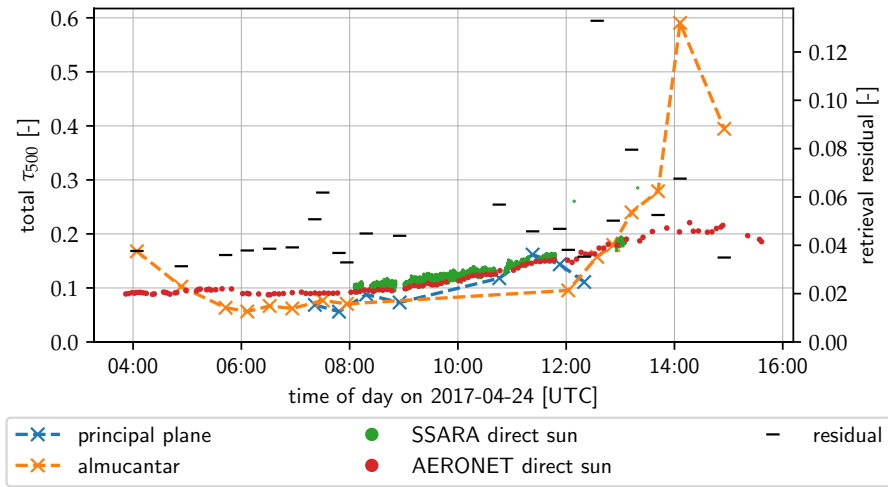
(a) Retrieved total AOD for 24 April 2017. For description see Fig. 4.17.

(b) Retrieved aerosol parameters for 24 April 2017. For description see Fig. 4.18.

(a) Retrieved total AOD for 27 April 2017. For description see Fig. 4.17.

(b) Retrieved aerosol parameters for 27 April 2017. For description see Fig. 4.18.

(a) Retrieved total AOD for 28 April 2017. For description see Fig. 4.17.

(b) Retrieved aerosol parameters for 28 April 2017. For description see Fig. 4.18.

Bibliography

Albrecht, B. A.: Aerosols, Cloud Microphysics, and Fractional Cloudiness, Science, 245, 1227–1230, https://doi.org/10.1126/science.245.4923.1227, 1989.

Anderson, G. P., Clough, S. A., Kneizys, F., Chetwynd, J. H., and Shettle, E. P.: AFGL atmospheric constituent profiles (0-120 km), Tech. rep., Air Force Geophysics Lab Hanscom AFB, MA, 1986.

Arola, A., Eck, T. F., Kokkola, H., Pitkänen, M. R. A., and Romakkaniemi, S.: Assessment of cloud-related fine-mode AOD enhancements based on AERONET SDA product, Atmospheric Chemistry and Physics, 17, 5991–6001, https://doi.org/10.5194/acp-17-5991-2017, 2017.

Baars, H., Kanitz, T., Engelmann, R., Althausen, D., Heese, B., Komppula, M., Preißler, J., Tesche, M., Ansmann, A., Wandinger, U., Lim, J.-H., Ahn, J. Y., Stachlewska, I. S., Amiridis, V., Marinou, E., Seifert, P., Hofer, J., Skupin, A., Schneider, F., Bohlmann, S., Foth, A., Bley, S., Pfüller, A., Giannakaki, E., Lihavainen, H., Viisanen, Y., Hooda, R. K., Pereira, S. N., Bortoli, D., Wagner, F., Mattis, I., Janicka, L., Markowicz, K. M., Achtert, P., Artaxo, P., Pauliquevis, T., Souza, R. A. F., Sharma, V. P., van Zyl, P. G., Beukes, J. P., Sun, J., Rohwer, E. G., Deng, R., Mamouri, R.-E., and Zamorano, F.: An overview of the first decade of Polly$^{\mathrm{NET}}$: an emerging network of automated Raman-polarization lidars for continuous aerosol profiling, Atmospheric Chemistry and Physics, 16, 5111–5137, https://doi.org/10.5194/acp-16-5111-2016, 2016.

Balois, J. Y.: Polarizing box POLBOX User's Guide, Tech. rep., Laboratoire d'Optique Atmospherique, Lille, 1998.

Bass, M., DeCusatis, C., Enoch, J., Lakshminarayanan, V., Li, G., Macdonald, C., Mahajan, V., and Van Stryland, E.: Handbook of Optics, Third Edition Volume II: Design, Fabrication and Testing, Sources and Detectors, Radiometry and Photometry, McGraw-Hill, Inc., New York, NY, USA, 3 edn., 2010.

Bodhaine, B. A., Wood, N. B., Dutton, E. G., and Slusser, J. R.: On Rayleigh Optical Depth Calculations, Journal of Atmospheric and Oceanic Technology, 16, 1854–1861, https://doi.org/10.1175/1520-0426(1999)016⟨1854:ORODC⟩2.0.CO;2, 1999.

Bogumil, K., Orphal, J., Homann, T., Voigt, S., Spietz, P., Fleischmann, O., Vogel, A., Hartmann, M., Kromminga, H., Bovensmann, H., Frerick, J., and Burrows, J.: Measurements of molecular absorption spectra with the SCIAMACHY pre-flight model: instrument characterization and reference data for atmospheric remote-sensing in the 230–2380 nm region, Journal of Photochemistry and Photobiology A: Chemistry, 157, 167–184, https://doi.org/10.1016/S1010-6030(03)00062-5, 2003.

Bond, T. C. and Bergstrom, R. W.: Light Absorption by Carbonaceous Particles: An Investigative Review, Aerosol Science and Technology, 40, 27–67, https://doi.org/10.1080/02786820500421521, 2006.

Bretagnon, P. and Francou, G.: Planetary theories in rectangular and spherical variables — VSOP 87 solutions, Astronomy and Astrophysics, 202, 309–315, 1988.

Breunig, M. M., Kriegel, H.-P., Ng, R. T., and Sander, J.: LOF: Identifying Density-based Local Outliers, SIGMOD Rec., 29, 93–104, https://doi.org/10.1145/335191.335388, 2000.

Buras, R. and Mayer, B.: Efficient unbiased variance reduction techniques for Monte Carlo simulations of radiative transfer in cloudy atmospheres: The solution, Journal of Quantitative Spectroscopy and Radiative Transfer, 112, 434–447, https://doi.org/10.1016/j.jqsrt.2010.10.005, 2011.

Bühl, J., Seifert, P., Wandinger, U., Baars, H., Kanitz, T., Schmidt, J., Myagkov, A., Engelmann, R., Skupin, A., Heese, B., Klepel, A., Althausen, D., and Ansmann, A.: LACROS: the Leipzig Aerosol and Cloud Remote Observations System, Proc. SPIE, 8890, https://doi.org/10.1117/12.2030911, 2013.

Calbó, J., Long, C. N., González, J.-A., Augustine, J., and McComiskey, A.: The thin border between cloud and aerosol: Sensitivity of several ground based observation techniques, Atmospheric Research, 196, 248–260, https://doi.org/10.1016/j.atmosres.2017.06.010, 2017.

Chandrasekhar, S.: Radiative Transfer, Dover books on physics and engineering, Dover Publications, Inc., 1950.

Chowdhary, J., Cairns, B., Mishchenko, M., and Travis, L.: Retrieval of aerosol properties over the ocean using multispectral and multiangle Photopolarimetric measurements from the Research Scanning Polarimeter, Geophysical Research Letters, 28, 243–246, https://doi.org/10.1029/2000GL011783, 2001.

Chýlek, P., Damiano, P., and Shettle, E. P.: Infrared Emittance of Water Clouds, Journal of the Atmospheric Sciences, 49, 1459–1472, https://doi.org/10.1175/1520-0469(1992)049⟨1459:IEOWC⟩2.0.CO;2, 1992.

Collett, E.: The Description of Polarization in Classical Physics, American Journal of Physics, 36, 713–725, https://doi.org/10.1119/1.1975098, 1968.

de Haan, J. F., Bosma, P., and Hovenier, J.: The adding method for multiple scattering calculations of polarized light, Astronomy and Astrophysics, 183, 371–391, 1987.

Deschamps, P., Breon, F., Leroy, M., Podaire, A., Bricaud, A., Buriez, J., and Seze, G.: The POLDER mission: instrument characteristics and scientific objectives, IEEE Transactions on Geoscience and Remote Sensing, 32, 598–615, https://doi.org/10.1109/36.297978, 1994.

Di Noia, A., Hasekamp, O. P., van Harten, G., Rietjens, J. H. H., Smit, J. M., Snik, F., Henzing, J. S., de Boer, J., Keller, C. U., and Volten, H.: Use of neural networks in ground-based aerosol retrievals from multi-angle spectropolarimetric observations, Atmospheric Measurement Techniques, 8, 281–299, https://doi.org/10.5194/amt-8-281-2015, 2015.

Diner, D. J., Xu, F., Garay, M. J., Martonchik, J. V., Rheingans, B. E., Geier, S., Davis, A., Hancock, B. R., Jovanovic, V. M., Bull, M. A., Capraro, K., Chipman, R. A., and McClain, S. C.: The Airborne Multiangle SpectroPolarimetric Imager (AirMSPI): a new tool for aerosol and cloud remote sensing, Atmospheric Measurement Techniques, 6, 2007–2025, https://doi.org/10.5194/amt-6-2007-2013, 2013.

Dubovik, O. and King, M. D.: A flexible inversion algorithm for retrieval of aerosol optical properties from Sun and sky radiance measurements, Journal of Geophysical Research: Atmospheres, 105, 20 673–20 696, https://doi.org/10.1029/2000JD900282, 2000.

Dubovik, O., Holben, B., Eck, T. F., Smirnov, A., Kaufman, Y. J., King, M. D., Tanré, D., and Slutsker, I.: Variability of Absorption and Optical Properties of Key Aerosol Types Observed in Worldwide Locations, Journal of the Atmospheric Sciences, 59, 590–608, https://doi.org/10.1175/1520-0469(2002)059⟨0590:VOAAOP⟩2.0.CO;2, 2002.

Dubovik, O., Sinyuk, A., Lapyonok, T., Holben, B. N., Mishchenko, M., Yang, P., Eck, T. F., Volten, H., Muñoz, O., Veihelmann, B., van der Zande, W. J., Leon, J.-F., Sorokin, M., and Slutsker, I.: Application of spheroid models

to account for aerosol particle nonsphericity in remote sensing of desert dust, Journal of Geophysical Research: Atmospheres, 111, https://doi.org/10.1029/2005JD006619, 2006.

Dubovik, O., Herman, M., Holdak, A., Lapyonok, T., Tanré, D., Deuzé, J. L., Ducos, F., Sinyuk, A., and Lopatin, A.: Statistically optimized inversion algorithm for enhanced retrieval of aerosol properties from spectral multi-angle polarimetric satellite observations, Atmospheric Measurement Techniques, 4, 975–1018, https://doi.org/10.5194/amt-4-975-2011, 2011.

Eck, T. F., Holben, B. N., Reid, J. S., Dubovik, O., Smirnov, A., O'Neill, N. T., Slutsker, I., and Kinne, S.: Wavelength dependence of the optical depth of biomass burning, urban, and desert dust aerosols, Journal of Geophysical Research: Atmospheres, 104, 31 333–31 349, https://doi.org/10.1029/1999JD900923, 1999.

Eck, T. F., Holben, B. N., Reid, J. S., O'Neill, N. T., Schafer, J. S., Dubovik, O., Smirnov, A., Yamasoe, M. A., and Artaxo, P.: High aerosol optical depth biomass burning events: A comparison of optical properties for different source regions, Geophysical Research Letters, 30, https://doi.org/10.1029/2003GL017861, 2003.

Eck, T. F., Holben, B. N., Reid, J. S., Arola, A., Ferrare, R. A., Hostetler, C. A., Crumeyrolle, S. N., Berkoff, T. A., Welton, E. J., Lolli, S., Lyapustin, A., Wang, Y., Schafer, J. S., Giles, D. M., Anderson, B. E., Thornhill, K. L., Minnis, P., Pickering, K. E., Loughner, C. P., Smirnov, A., and Sinyuk, A.: Observations of rapid aerosol optical depth enhancements in the vicinity of polluted cumulus clouds, Atmospheric Chemistry and Physics, 14, 11 633–11 656, https://doi.org/10.5194/acp-14-11633-2014, 2014.

Emde, C. and Mayer, B.: Errors induced by the neglect of polarization in radiance calculations for three-dimensional cloudy atmospheres, Journal of Quantitative Spectroscopy and Radiative Transfer, 218, 151–160, https://doi.org/10.1016/j.jqsrt.2018.07.001, 2018.

Emde, C., Buras, R., Mayer, B., and Blumthaler, M.: The impact of aerosols on polarized sky radiance: model development, validation, and applications, Atmospheric Chemistry and Physics, 10, 383–396, https://doi.org/10.5194/acp-10-383-2010, 2010.

Emde, C., Barlakas, V., Cornet, C., Evans, F., Korkin, S., Ota, Y., Labonnote, L. C., Lyapustin, A., Macke, A., Mayer, B., and Wendisch, M.: IPRT polarized radiative transfer model intercomparison project – Phase A, Journal of Quantitative Spectroscopy and Radiative Transfer, 164, 8–36, https://doi.org/10.1016/j.jqsrt.2015.05.007, 2015.

Emde, C., Buras-Schnell, R., Kylling, A., Mayer, B., Gasteiger, J., Hamann, U., Kylling, J., Richter, B., Pause, C., Dowling, T., and Bugliaro, L.: The libRadtran software package for radiative transfer calculations (version 2.0.1), Geoscientific Model Development, 9, 1647–1672, https://doi.org/10.5194/gmd-9-1647-2016, 2016.

Emde, C., Barlakas, V., Cornet, C., Evans, F., Wang, Z., Labonotte, L. C., Macke, A., Mayer, B., and Wendisch, M.: IPRT polarized radiative transfer model intercomparison project – Three-dimensional test cases (phase B), Journal of Quantitative Spectroscopy and Radiative Transfer, 209, 19–44, https://doi.org/10.1016/j.jqsrt.2018.01.024, 2018.

Engelmann, R., Kanitz, T., Baars, H., Heese, B., Althausen, D., Skupin, A., Wandinger, U., Komppula, M., Stachlewska, I. S., Amiridis, V., Marinou, E., Mattis, I., Linné, H., and Ansmann, A.: The automated multiwavelength Raman polarization and water-vapor lidar Polly[XT]: the neXT generation, Atmospheric Measurement Techniques, 9, 1767–1784, https://doi.org/10.5194/amt-9-1767-2016, 2016.

Fedarenka, A., Dubovik, O., Goloub, P., Li, Z., Lapyonok, T., Litvinov, P., Barel, L., Gonzalez, L., Podvin, T., and Crozel, D.: Utilization of AERONET polarimetric measurements for improving retrieval of aerosol microphysics: GSFC, Beijing and Dakar data analysis, Journal of Quantitative Spectroscopy and Radiative Transfer, 179, 72–97, https://doi.org/10.1016/j.jqsrt.2016.03.021, 2016.

Forgan, B. W.: General method for calibrating sun photometers, Appl. Opt., 33, 4841–4850, https://doi.org/10.1364/AO.33.004841, 1994.

Freudenthaler, V., Esselborn, M., Wiegner, M., Heese, B., Tesche, M., Ansmann, A., Müller, D., Althausen, D., Wirth, M., Fix, A., Ehret, G., Knippertz, P., Toledano, C., Gasteiger, J., Garhammer, M., and Seefeldner, M.: Depolarization ratio profiling at several wavelengths in pure Saharan dust during SAMUM 2006, Tellus B: Chemical and Physical Meteorology, 61, 165–179, https://doi.org/10.1111/j.1600-0889.2008.00396.x, 2009.

Fröhlich, C. and Shaw, G. E.: New determination of Rayleigh scattering in the terrestrial atmosphere, Appl. Opt., 19, 1773–1775, https://doi.org/10.1364/AO.19.001773, 1980.

Gasteiger, J., Groß, S., Freudenthaler, V., and Wiegner, M.: Volcanic ash from Iceland over Munich: mass concentration retrieved from ground-based remote sensing measurements, Atmospheric Chemistry and Physics, 11, 2209–2223, https://doi.org/10.5194/acp-11-2209-2011, 2011.

GCOS: Systematic Observation Requirements for Satellite-based Products for Climate Supplemental details to the satellite-based component of the Implementation Plan for the Global Observing System for Climate in Support of the UNFCCC: 2011 update, GCOS-No. 154, WMO, 2011.

Giles, D. M., Sinyuk, A., Sorokin, M. G., Schafer, J. S., Smirnov, A., Slutsker, I., Eck, T. F., Holben, B. N., Lewis, J. R., Campbell, J. R., Welton, E. J., Korkin, S. V., and Lyapustin, A. I.: Advancements in the Aerosol Robotic Network (AERONET) Version 3 database – automated near-real-time quality control algorithm with improved cloud screening for Sun photometer aerosol optical depth (AOD) measurements, Atmospheric Measurement Techniques, 12, 169–209, https://doi.org/10.5194/amt-12-169-2019, 2019.

Gobbi, G. P., Kaufman, Y. J., Koren, I., and Eck, T. F.: Classification of aerosol properties derived from AERONET direct sun data, Atmospheric Chemistry and Physics, 7, 453–458, https://doi.org/10.5194/acp-7-453-2007, 2007.

Grob, H., Emde, C., and Mayer, B.: Retrieval of aerosol properties from ground-based polarimetric sky-radiance measurements under cloudy conditions, Journal of Quantitative Spectroscopy and Radiative Transfer, 228, 57–72, https://doi.org/10.1016/j.jqsrt.2019.02.025, 2019a.

Grob, H., Emde, C., Wiegner, M., Seefeldner, M., and Mayer, B.: The polarized sun and sky radiometer SSARA: design, calibration, and application for ground based aerosol remote sensing, Atmospheric Measurement Techniques Discussions, https://doi.org/10.5194/amt-2019-226, in review, 2019b.

Hansen, J. E.: Radiative transfer by doubling very thin layers, Astrophys. J., 155, 565–573, https://doi.org/10.1086/149892, 1969.

Hansen, J. E.: Multiple Scattering of Polarized Light in Planetary Atmospheres. Part I. The Doubling Method, Journal of the Atmospheric Sciences, 28, 120–125, https://doi.org/10.1175/1520-0469(1971)028⟨0120:MSOPLI⟩2.0.CO;2, 1971.

Hansen, J. E. and Travis, L. D.: Light scattering in planetary atmospheres, Space Science Reviews, 16, 527–610, https://doi.org/10.1007/BF00168069, 1974.

Hasekamp, O. and Landgraf, J.: A linearized vector radiative transfer model for atmospheric trace gas retrieval, Journal of Quantitative Spectroscopy and Radiative Transfer, 75, 221 – 238, https://doi.org/10.1016/S0022-4073(01)00247-3, 2002.

Hasekamp, O. P. and Landgraf, J.: Retrieval of aerosol properties over land surfaces: capabilities of multiple-viewing-angle intensity and polarization measurements, Appl. Opt., 46, 3332–3344, https://doi.org/10.1364/AO.46.003332, 2007.

Hasekamp, O. P., Litvinov, P., and Butz, A.: Aerosol properties over the ocean from PARASOL multiangle photopolarimetric measurements, Journal of Geophysical Research: Atmospheres, 116, https://doi.org/10.1029/2010JD015469, 2011.

Hess, M., Köpke, P., and Schult, I.: Optical Properties of Aerosols and Clouds: The Software Package OPAC, Bulletin of the American Meteorological Society, 79, 831–844, https://doi.org/10.1175/1520-0477(1998)079⟨0831:OPOAAC⟩2.0.CO;2, 1998.

Holben, B., Eck, T., Slutsker, I., Tanré, D., Buis, J., Setzer, A., Vermote, E., Reagan, J., Kaufman, Y., Nakajima, T., Lavenu, F., Jankowiak, I., and Smirnov, A.: AERONET — A Federated Instrument Network and Data Archive for Aerosol Characterization, Remote Sensing of Environment, 66, 1–16, https://doi.org/10.1016/S0034-4257(98)00031-5, 1998.

Holben, B. N., Eck, T. F., Slutsker, I., Smirnov, A., Sinyuk, A., Schafer, J., Giles, D., and Dubovik, O.: Aeronet's Version 2.0 quality assurance criteria, Proc.SPIE, 6408, https://doi.org/10.1117/12.706524, 2006.

Horn, B. K. P.: Closed–form solution of absolute orientation using unit quaternions, J. Opt. Soc. Am. A, 4, 629–642, https://doi.org/10.1364/JOSAA.4.000629, 1987.

Hovenier, J. W.: Symmetry Relationships for Scattering of Polarized Light in a Slab of Randomly Oriented Particles, Journal of the Atmospheric Sciences, 26, 488–499, https://doi.org/10.1175/1520-0469(1969)026⟨0488:SRFSOP⟩2.0.CO;2, 1969.

Hovenier, J. W.: Multiple Scattering of Polarized Light in Planetary Atmospheres, Astronomy & Astrophysics, 13, 7, 1971.

Howell, H. B. and Jacobowitz, H.: Matrix Method Applied to the Multiple Scattering of Polarized Light, Journal of the Atmospheric Sciences, 27, 1195–1206, https://doi.org/10.1175/1520-0469(1970)027⟨1195:MMATTM⟩2.0.CO;2, 1970.

IPCC: Climate Change 2013: The Physical Science Basis. Contribution of Working Group I to the Fifth Assessment Report of the Intergovernmental Panel on Climate Change, Cambridge University Press, Cambridge, United Kingdom and New York, NY, USA, https://doi.org/10.1017/CBO9781107415324, 2013.

Kasten, F. and Young, A. T.: Revised optical air mass tables and approximation formula, Appl. Opt., 28, 4735–4738, https://doi.org/10.1364/AO.28.004735, 1989.

Koren, I., Remer, L. A., Kaufman, Y. J., Rudich, Y., and Martins, J. V.: On the twilight zone between clouds and aerosols, Geophysical Research Letters, 34, https://doi.org/10.1029/2007GL029253, 2007.

Koren, I., Feingold, G., Jiang, H., and Altaratz, O.: Aerosol effects on the inter-cloud region of a small cumulus cloud field, Geophysical Research Letters, 36, https://doi.org/10.1029/2009GL037424, 2009.

Kraft, D.: A Software Package for Sequential Quadratic Programming, DFVLR-FB 88-28, DFVLR Insitut für Dynamik der Flugsysteme, 1988.

Kreuter, A., Emde, C., and Blumthaler, M.: Measuring the influence of aerosols and albedo on sky polarization, Atmospheric Research, 98, 363–367, https://doi.org/10.1016/j.atmosres.2010.07.010, 2010.

Köpke, P., Hess, M., Schult, I., and Shettle, E. P.: Global aerosol data set, Report No. 243, MPI Meteorologie Hamburg, 1997.

Landgraf, J., Hasekamp, O. P., Box, M. A., and Trautmann, T.: A linearized radiative transfer model for ozone profile retrieval using the analytical forward-adjoint perturbation theory approach, Journal of Geophysical Research: Atmospheres, 106, 27 291–27 305, https://doi.org/10.1029/2001JD000636, 2001.

Li, J., Min, Q., Peng, Y., Sun, Z., and Zhao, J.-Q.: Accounting for dust aerosol size distribution in radiative transfer, Journal of Geophysical Research: Atmospheres, 120, 6537–6550, https://doi.org/10.1002/2015JD023078, 2015.

Li, L., Li, Z., Li, K., Blarel, L., and Wendisch, M.: A method to calculate Stokes parameters and angle of polarization of skylight from polarized CIMEL sun/sky radiometers, Journal of Quantitative Spectroscopy and Radiative Transfer, 149, 334–346, https://doi.org/doi.org/10.1016/j.jqsrt.2014.09.003, 2014.

Li, Z., Goloub, P., Dubovik, O., Blarel, L., Zhang, W., Podvin, T., Sinyuk, A., Sorokin, M., Chen, H., Holben, B., Tanré, D., Canini, M., and Buis, J.-P.: Improvements for ground-based remote sensing of atmospheric aerosol properties by additional polarimetric measurements, Journal of Quantitative Spectroscopy and Radiative Transfer, 110, 1954–1961, https://doi.org/10.1016/j.jqsrt.2009.04.009, 2009.

Li, Z., Blarel, L., Podvin, T., Goloub, P., and Chen, L.: Calibration of the degree of linear polarization measurement of polarized radiometer using solar light, Appl. Opt., 49, 1249–1256, https://doi.org/10.1364/AO.49.001249, 2010.

Li, Z., Li, K., Li, L., Xu, H., Xie, Y., Ma, Y., Li, D., Goloub, P., Yuan, Y., and Zheng, X.: Calibration of the degree of linear polarization measurements of the polarized Sun-sky radiometer based on the POLBOX system, Appl. Opt., 57, 1011–1018, https://doi.org/10.1364/AO.57.001011, 2018.

Mamouri, R. E., Ansmann, A., Nisantzi, A., Kokkalis, P., Schwarz, A., and Hadjimitsis, D.: Low Arabian dust extinction-to-backscatter ratio, Geophysical Research Letters, 40, 4762–4766, https://doi.org/10.1002/grl.50898, 2013.

Marshak, A., Wen, G., Coakley, J. A., Remer, L. A., Loeb, N. G., and Cahalan, R. F.: A simple model for the cloud adjacency effect and the apparent bluing of aerosols near clouds, Journal of Geophysical Research: Atmospheres, 113, https://doi.org/10.1029/2007JD009196, 2008.

Mayer, B.: Radiative transfer in the cloudy atmosphere, European Physical Journal Conferences, 1, 75–99, https://doi.org/10.1140/epjconf/e2009-00912-1, 2009.

Mayer, B. and Kylling, A.: Technical note: The libRadtran software package for radiative transfer calculations - description and examples of use, Atmospheric Chemistry and Physics, 5, 1855–1877, https://doi.org/10.5194/acp-5-1855-2005, 2005.

Mie, G.: Beiträge zur Optik trüber Medien, speziell kolloidaler Metallösungen, Annalen der Physik, 330, 377–445, https://doi.org/10.1002/andp.19083300302, 1908.

Mishchenko, M., Lacis, A., and Travis, L.: Errors induced by the neglect of polarization in radiance calculations for rayleigh-scattering atmospheres, Journal of Quantitative Spectroscopy and Radiative Transfer, 51, 491–510, https://doi.org/10.1016/0022-4073(94)90149-X, 1994.

Mishchenko, M. I., Cairns, B., Hansen, J. E., Travis, L. D., Burg, R., Kaufman, Y. J., Martins, J. V., and Shettle, E. P.: Monitoring of aerosol forcing of climate from space: analysis of measurement requirements, Journal of Quantitative Spectroscopy and Radiative Transfer, 88, 149–161, https://doi.org/10.1016/j.jqsrt.2004.03.030, 2004.

Müller, D., Mattis, I., Wandinger, U., Ansmann, A., Althausen, D., Dubovik, O., Eckhardt, S., and Stohl, A.: Saharan dust over a central European EARLINET-AERONET site: Combined observations with Raman lidar and Sun photometer, Journal of Geophysical Research: Atmospheres, 108, https://doi.org/10.1029/2002JD002918, 2003.

Nash, S.: Newton-Type Minimization via the Lanczos Method, SIAM Journal on Numerical Analysis, 21, 770–788, https://doi.org/10.1137/0721052, 1984.

Nicolet, M.: On the molecular scattering in the terrestrial atmosphere : An empirical formula for its calculation in the homosphere, Planetary and Space Science, 32, 1467–1468, https://doi.org/10.1016/0032-0633(84)90089-8, 1984.

O'Neill, N. T., Eck, T. F., Smirnov, A., Holben, B. N., and Thulasiraman, S.: Spectral discrimination of coarse and fine mode optical depth, Journal of Geophysical Research: Atmospheres, 108, https://doi.org/10.1029/2002JD002975, 2003.

Remer, L. A., Kaufman, Y. J., Holben, B. N., Thompson, A. M., and McNamara, D.: Biomass burning aerosol size distribution and modeled optical properties, Journal of Geophysical Research: Atmospheres, 103, 31 879–31 891, https://doi.org/10.1029/98JD00271, 1998.

Riesing, K. M., Yoon, H., and Cahoy, K. L.: Rapid telescope pointing calibration: a quaternion-based solution using low-cost hardware, Journal of Astronomical Telescopes, Instruments, and Systems, 4, https://doi.org/10.1117/1.JATIS.4.3.034002, 2018.

Rodgers, C. D.: Inverse Methods for Atmospheric Sounding: Theory and Practice, Series on Atmospheric, Oceanic and Planetary Physics, World Scientific, 2000.

Seefeldner, M., Oppenrieder, A., Rabus, D., Reuder, J., Schreier, M., Hoeppe, P., and Köpke, P.: A Two-Axis Tracking System with Datalogger, Journal of Atmospheric and Oceanic Technology, 21, 975–979, https://doi.org/10.1175/1520-0426(2004)021⟨0975:ATTSWD⟩2.0.CO;2, 2004.

Smirnov, A., Zhuravleva, T., Segal-Rosenheimer, M., and Holben, B.: Limitations of AERONET SDA product in presence of cirrus clouds, Journal of Quantitative Spectroscopy and Radiative Transfer, 206, 338–341, https://doi.org/10.1016/j.jqsrt.2017.12.007, 2018.

Spencer, J. W.: Fourier Series Representation of the Position of the Sun, Search, 2, 172, 1971.

Stap, F., Hasekamp, O., Emde, C., and Röckmann, T.: Influence of 3D effects on 1D aerosol retrievals in synthetic, partially clouded scenes, Journal of Quantitative Spectroscopy and Radiative Transfer, 170, 54–68, https://doi.org/10.1016/j.jqsrt.2015.10.008, 2016.

Stap, F. A., Hasekamp, O. P., and Röckmann, T.: Sensitivity of PARASOL multi-angle photopolarimetric aerosol retrievals to cloud contamination, Atmospheric

Measurement Techniques, 8, 1287–1301, https://doi.org/10.5194/amt-8-1287-2015, 2015.

Stevens, B., Moeng, C.-H., Ackerman, A. S., Bretherton, C. S., Chlond, A., de Roode, S., Edwards, J., Golaz, J.-C., Jiang, H., Khairoutdinov, M., Kirkpatrick, M. P., Lewellen, D. C., Lock, A., Müller, F., Stevens, D. E., Whelan, E., and Zhu, P.: Evaluation of Large-Eddy Simulations via Observations of Nocturnal Marine Stratocumulus, Monthly Weather Review, 133, 1443–1462, https://doi.org/10.1175/MWR2930.1, 2005.

Stohl, A., Forster, C., Frank, A., Seibert, P., and Wotawa, G.: Technical note: The Lagrangian particle dispersion model FLEXPART version 6.2, Atmospheric Chemistry and Physics, 5, 2461–2474, https://doi.org/10.5194/acp-5-2461-2005, 2005.

Toledano, C., Wiegner, M., Garhammer, M., Seefeldner, M., Gasteiger, J., Müller, D., and Köpke, P.: Spectral aerosol optical depth characterization of desert dust during SAMUM 2006, Tellus B: Chemical and Physical Meteorology, 61, 216–228, https://doi.org/10.1111/j.1600-0889.2008.00382.x, 2009.

Toledano, C., Wiegner, M., Groß, S., Freudenthaler, V., Gasteiger, J., Müller, D., Müller, D., Schladitz, A., Weinzierl, B., Torres, B., and O'Neill, N. T.: Optical properties of aerosol mixtures derived from sun-sky radiometry during SAMUM-2, Tellus B: Chemical and Physical Meteorology, 63, 635–648, https://doi.org/10.1111/j.1600-0889.2011.00573.x, 2011.

Twomey, S.: The Influence of Pollution on the Shortwave Albedo of Clouds, Journal of the Atmospheric Sciences, 34, 1149–1152, https://doi.org/10.1175/1520-0469(1977)034⟨1149:TIOPOT⟩2.0.CO;2, 1977.

Twomey, S., Jacobowitz, H., and Howell, H. B.: Matrix Methods for Multiple-Scattering Problems, Journal of the Atmospheric Sciences, 23, 289–298, https://doi.org/10.1175/1520-0469(1966)023⟨0289:MMFMSP⟩2.0.CO;2, 1966.

van Amerongen, A., Rietjens, J., Smit, M., van Loon, D., van Brug, H., van der Meulen, W., Esposito, M., and Hasekamp, O.: Spex the Dutch roadmap towards aerosol measurement from space, Proc.SPIE, 10562, https://doi.org/10.1117/12.2296227, 2017.

van de Hulst, H.: Light Scattering by Small Particles, Dover Books on Physics, Dover Publications, 1981.

van Harten, G., Snik, F., Rietjens, J. H. H., Smit, J. M., de Boer, J., Diamantopoulou, R., Hasekamp, O. P., Stam, D. M., Keller, C. U., Laan, E. C., Verlaan,

A. L., Vliegenthart, W. A., ter Horst, R., Navarro, R., Wielinga, K., Hannemann, S., Moon, S. G., and Voors, R.: Prototyping for the Spectropolarimeter for Planetary EXploration (SPEX): calibration and sky measurements, Proc.SPIE, 8160, https://doi.org/10.1117/12.893741, 2011.

van Harten, G., de Boer, J., Rietjens, J. H. H., Di Noia, A., Snik, F., Volten, H., Smit, J. M., Hasekamp, O. P., Henzing, J. S., and Keller, C. U.: Atmospheric aerosol characterization with a ground-based SPEX spectropolarimetric instrument, Atmospheric Measurement Techniques, 7, 4341–4351, https://doi.org/10.5194/amt-7-4341-2014, 2014.

Várnai, T. and Marshak, A.: Analysis of co-located MODIS and CALIPSO observations near clouds, Atmospheric Measurement Techniques, 5, 389–396, https://doi.org/10.5194/amt-5-389-2012, 2012.

Várnai, T., Marshak, A., and Eck, T. F.: Observation-Based Study on Aerosol Optical Depth and Particle Size in Partly Cloudy Regions, Journal of Geophysical Research: Atmospheres, 122, 10,013–10,024, https://doi.org/10.1002/2017JD027028, 2017.

Wallace, J. M. and Hobbs, P. V.: Atmospheric Science: An Introductory Survey, Academic Press, 2 edn., https://doi.org/10.1016/C2009-0-00034-8, 2006.

Wen, G., Marshak, A., Cahalan, R. F., Remer, L. A., and Kleidman, R. G.: 3-D aerosol-cloud radiative interaction observed in collocated MODIS and ASTER images of cumulus cloud fields, Journal of Geophysical Research: Atmospheres, 112, https://doi.org/10.1029/2006JD008267, 2007.

Wiedinmyer, C., Akagi, S. K., Yokelson, R. J., Emmons, L. K., Al-Saadi, J. A., Orlando, J. J., and Soja, A. J.: The Fire INventory from NCAR (FINN): a high resolution global model to estimate the emissions from open burning, Geoscientific Model Development, 4, 625–641, https://doi.org/10.5194/gmd-4-625-2011, 2011.

Wiscombe, W. J.: Improved Mie scattering algorithms, Appl. Opt., 19, 1505–1509, https://doi.org/10.1364/AO.19.001505, 1980.

Xu, X. and Wang, J.: Retrieval of aerosol microphysical properties from AERONET photopolarimetric measurements: 1. Information content analysis, Journal of Geophysical Research: Atmospheres, 120, 7059–7078, https://doi.org/10.1002/2015JD023108, 2015.

Xu, X., Wang, J., Zeng, J., Spurr, R., Liu, X., Dubovik, O., Li, L., Li, Z., Mishchenko, M. I., Siniuk, A., and Holben, B. N.: Retrieval of aerosol microphysical properties from AERONET photopolarimetric measurements: 2. A new

research algorithm and case demonstration, Journal of Geophysical Research: Atmospheres, 120, 7079–7098, https://doi.org/10.1002/2015JD023113, 2015.

Yang, W., Marshak, A., Várnai, T., and Wood, R.: CALIPSO observations of near-cloud aerosol properties as a function of cloud fraction, Geophysical Research Letters, 41, 9150–9157, https://doi.org/10.1002/2014GL061896, 2014.

Ångström, A.: On the Atmospheric Transmission of Sun Radiation and on Dust in the Air, Geografiska Annaler, 11, 156–166, https://doi.org/10.1080/20014422. 1929.11880498, 1929.

Acknowledgements